12-2013

Zinc Oxide Nanorod Based Ultraviolet Detectors with Wheatstone Bridge Design

Arun Vasudevan
University of Arkansas, Fayetteville

Zinc Oxide Nanorod Based Ultraviolet Detectors with Wheatstone Bridge Design

Zinc Oxide Nanorod Based Ultraviolet Detectors with Wheatstone Bridge Design

A dissertation submitted in partial fulfillment
of the requirements for the degree of
Doctor of Philosophy in Microelectronics-Photonics

By

Arun Vasudevan
University of Kerala
Bachelor of Science in Physics, 2002
Cochin University of Science and Technology
Master of Science in Physics, 2005

December 2013
University of Arkansas

This dissertation is approved for recommendation to the Graduate Council.

_____   _____
Dr. Taeksoo Ji   Dr. Simon Ang
Dissertation Director   Dissertation Co-Director

_____   _____
Dr. Z. Ryan Tian   Dr. Shui-Qing (Fisher) Yu
Committee Member   Committee Member

_____
Prof. Kenneth Vickers
Committee Member

The following signatories attest that all software used in this dissertation was legally licensed for use by Arun Vasudevan for research purposes and publication.

_____   _____

Mr. Arun Vasudevan, Student   Dr. Simon Ang, Dissertation Co-Director

This dissertation was submitted to http://www.turnitin.com for plagiarism review by the TurnItIn company's software. The signatories have examined the report on this dissertation that was returned by TurnItIn and attest that, in their opinion, the items highlighted by the software are incidental to common usage and are not plagiarized material.

_____   _____

Prof. Ken Vickers, Program Director   Dr. Simon Ang, Dissertation Co-Director

ABSTRACT

This research work, for the first time, investigated metal-semiconductor-metal (MSM) zine oxide (ZnO) nanorod based ultra-violet (UV) detectors having a Wheatstone bridge design with a high responsivity at room temperature and above, as well as a responsivity that was largely independent of the change in ambient conditions. The ZnO nanorods which acted as the sensing element of the detector were grown by a chemical growth technique. Studies were conducted to determine the effects on ZnO nanorod properties by varying the concentration of the chemicals used for the rod growth. These studies showed how the rod diameter and the deposition of ZnO nanorods from the solution was controlled by varying the concentration of the chemicals used for the rod growth. Conventional MSM UV detectors were fabricated with ZnO nanorods grown under optimized conditions to determine the dependence of UV response on electrode dimension and rod dimension. These studies gave insights into the dependence of UV response on the width of the electrode, spacing between the electrodes, density of the rod growth, and length and diameter of the rods. The UV responsivity was affected by varying the number of times the seed layer was spin coated, by varying the spin speed of seed layer coating and by varying the annealing temperature of the seed and rod. Based on these studies, optimum conditions for the fabrication of Wheatstone bridge UV ZnO nanorod detectors were determined. The Wheatstone bridge ZnO nanorod UV detectors were fabricated in three different configurations, namely, symmetric, asymmetric, and quasi-symmetric. The transient responses of the symmetric, asymmetric and quasi-symmetric configurations at room temperature and above showed how the response stability differed. At high temperature the responsivity of quasi-symmetric Wheatstone bridge detector configuration did not drop after saturation and the responsivity drifted by 17% to 25% from the room temperature response. The responsivity of the symmetric, asymmetric (rods in one quadrant), asymmetric (rods in three quadrant), and quasi-symmetric Wheatstone bridge

was approximately 3.25 A/W, 0.95 A/W, 15.00 A/W, and 1.20 A/W and the corresponding response time was 299 sec, 71 sec, 217 sec, and 159 sec, respectively. The responsivity of quasi-symmetric Wheatstone bridge configuration with good temperature stability was 1.16 A/W, while those of conventional MSM UV detectors were approximately 60 A/W. However, the quasi-symmetric Wheatstone bridge with responsivity 1.16 A/W was higher than the commercially available detector having responsivity of only about 0.1 A/W. Though the response of quasi-symmetric Wheatstone bridge detector was higher than the detectors available commercially, the response time was very high. The response time of quasi-symmetric Wheatstone bridge was approximately 159 seconds at room temperature, while that of commercially available detectors is of the order of microseconds. If the quasi-symmetric Wheatstone bridge has to compete with current commercially available detectors, then the response time should be brought down from seconds to microseconds. Based on these studies, an improved design of the quasi-symmetric Wheatstone bridge UV detector with the ZnO rods oriented parallel to the substrate instead of oriented vertical to the substrate was proposed.

Tripuraneni, Mrs. Sindhu Mirosh, Mr. Sundeep Chalamalasetty, Mr. Suraj Sujathan, Mr. Vinayaraj O. K., Ms. Vinayasree S., Mrs. Vineetha V. S., and Dr. Vivek A. K., for all the help and wonderful moments they gifted me.

Last but not least I would like to thank my grandparents Mr. Narayanan Pillai and late Mrs. Sumathi S., my parents Mr. Vasudevan Pillai and Mrs. Usha S., my uncle Mr. Rajendra Pillai, my aunt Mrs. Girija S., and my younger brother Mr. Aneesh V. for actively supporting, encouraging and standing behind me with my decisions and goals.

DEDICATION

I would like to dedicate this dissertation to all the teachers who taught me to dream and gave me

the wings to reach those dreams.

TABLE OF CONTENTS

LIST OF FIGURES

LIST OF TABLES

ABBREVIATIONS

A- Ampere

A/W- Ampere/Watt

Å- Angstrom

ad- Adsorbed

Ag- Silver

Al- Aluminium

AlGaN- Aluminium Gallium Nitride

Au- Gold

CCD- Charge Coupled Device

CdS- Cadmium Sulphide

Cr- Chromium

DNA- Deoxyribonucleic Acid

EDAX- Energy Dispersive X-ray Analysis

eV- Electron Volt

g- Gas

GaN- Galium Nitride

HMT- Hexamethylenetetramine

ICDD- International Center for Diffraction Data

P_{inc}- Incident Power

I_{ph}- Photocurrent

I-V- Current-Voltage

M- Molarity

meV- Milli Electron Volt

MSM- Metal Semiconductor Metal

mW/cm^2- Milli Watt/Centimeter^2

Ni- Nickle

nm- Nanometer

NRs- Nanorods

O_2- Oxygen

Pd- Palladium

PMT- Photomultiplier Tube

Pt- Platinum

rpm- Rotations Per Minute

Ru- Rubudium

s- Solid

Sec- Seconds

SEM- Scanning Electron Microscope

Si- Silicon

Si/SiO$_2$- Silicon/Silicon Oxide

SiC- Silicon Carbide

UV- Ultraviolet

V- Volt

XRD- X-Ray Diffraction

ZnO- Zinc Oxide

ZnS- Zinc Sulphide

ZnSe- Zinc Selenide

Ω- Ohm

μm- Micrometer

^{0}C- Degree Celsius

1.   INTRODUCTION

Electromagnetic radiation having wavelengths from 400 nm-10 nm is called Ultraviolet. A device that can detect and quantify the intensity of ultraviolet (UV) light is called an ultraviolet detector. An UV detector that quantifies the intensity of incident radiation by measuring the change in electrical signal on absorption of the incident photons is called UV photodetector. Some commonly used UV photodetectors are silicon detector, photomultiplier tube (PMT), and charge coupled device (CCD). A UV detector that quantifies the intensity of the incident light by measuring the change in temperature dependent properties is called a thermal detector. The commonly used thermal detectors are bolometer and pyroelectric detectors. In bolometer detectors a change in resistance is measured and in pyroelectric detectors a change in electric polarization is measured.

1.1   APPLICATIONS OF UV DETECTOR

UV detectors have great demand in fields like civilian for medical applications and water sterilization, military for small arms fire detection and missile plumes, environmental and biological research, astronomical studies, high temperature plasma research, optical communication, space studies and for monitoring the thickness of the ozone layer which blocks harmful UV radiation from sun reaching earth (1-4). UV detection is also helpful in keeping track of the human exposure to UV radiation since studies have shown that UV radiation can increase rate of aging, cause cancer, affect DNA structure and affect the immune system (5).

1.2   CURRENTLY USED UV DETECTORS AND ITS DRAWBACKS

A detector with ideal performance characteristics should have high signal-to-noise ratio, high selectivity, high response speed, and less energy consumption of the electrical power source. Comparing these to the performance characteristics of the current widely used UV detectors, they are bulky, low selectivity (200-1100 nm), and require high voltage biasing. Currently used UV detectors are photo-detectors such as Si based detectors, photomultiplier tubes, and charge coupled devices and thermal detectors such as pyrometers and bolometers **(6-8)**. In case of a Si detectors, since its band gap energy is less than that of visible light, it is sensitive to visible light. Hence, visible light blocking filters are required. Also, for high sensitivity (10 nW/ cm^2 to 1 mW/cm^2) applications cooling is required to reduce the dark current **(7)**. The sensitivity of a Si detector is very low at room temperature and its sensitivity increases with decrease in temperature. But cooled detectors will serve as cold traps for the contaminants thereby affecting the sensitivity of the detector. For photomultiplier tubes though the gain is high (~10^5 to 10^7 dB), noise is low (~1.3 x 10^{-18} W) and fairly insensitive (75 mA/W at 400 nm) to visible light. The drawback is that they are bulky, fragile and require high biasing. In case of CCD the response is fast (~few nanosec) but it is independent of the wavelength of light. Similarly the response of thermal detectors is about millisec and responsivity of about1000- 2000 V/W, but its wavelength independent. The other major disadvantage of all the above mentioned detectors are device aging on exposure to radiation higher than the band gap of the material, intolerant to high temperature (> 333 K) and environment with radiations greater than 124 eV (Enhanced UV) **(9)**. Many applications require an alternative UV detector which is of micro-sized, portable, high sensitivity (10 nW/ cm^2 to 1 mW/cm^2), and robust to high energy radiation (>124 eV) and temperature

(> 333 K). So, the current focus of researchers is to develop UV detectors that meet this demand.

1.3 ALTERNATIVE UV SENSING ELEMENTS

The drawbacks of silicon based detectors, photomultiplier tubes, CCD, pyrometers and bolometer can be overcome with wide band gap semiconductors like galium nitride (GaN), silicon carbide (SiC), aluminium galium nitride (AlGaN), zinc selenide (ZnSe), diamond and zinc oxide (ZnO) etc. **(2, 10, 11-14)**. UV detectors based on wide band gap materials do not need an optical filter since the band gap energy of these materials is higher than visible light. Hence, they are insensitive to visible light. The band gap of these wide band gap semiconductors is shown in Table 1-1. Also, the melting point of the wide bandgap semiconductors shown in Table 1-1 suggest that wide band gap materials are thermally and chemically more stable than low

Table 1-1 Comparison of properties of wide band gap semiconductors (8).

Wide band gap semiconductor	Crystal structure	Lattice Parameter (A^o)		$E_g(eV)$ at RT	Melting temp. (K)	Excitation binding energy (meV)
		a	c			
ZnO	Wurtzite	3.25	5.206	3.37	2248	60
GaN	Wurtzite	3.189	5.185	3.4	1973	21
ZnSe	Zinc-blende	5.667	-	2.7	1790	20
ZnS	Wurtzite	3.824	6.261	3.7	2103	36
4H-SiC	Wurtzite	3.073	10.053	3.26	2070	35

band gap semiconductors. Due to high thermal conductivity and strong chemical bonds, UV detectors based on these materials can be used in harsh environments where temperature greater

than 333 K and radiation of energy greater than 124 eV **(15)**. In addition to the above mentioned benefits, since the wide bandgap semiconductors are chemically stable, a passivation layer is not required thereby improving the responsivity and stability at short wavelength. The other advantages of solid state wideband gap based UV detectors are lighter, more efficient than low band gap based detectors and incorporation into micro and nanosystems or portable devices like cell phones is easier.

1.4 BEST UV SENSING ELEMENT IN WIDE BANDGAP SEMICONDUCTORS

Responsivity of a detector is defined as the ratio of the photocurrent (I_{ph}) expressed in amperes to the incident power (P_{inc}) expressed in watts. The responsivity of a detector is a measure of the ability of the detector to convert the radiation incident on the detector into photocurrent. Since the radiation absorbed by a material changes with wavelength, the responsivity of the detector also changes with wavelength,

$$R = \frac{I_{ph}}{P_{inc}} = \frac{\eta q}{h\nu} \qquad (1-1)$$

where, η is the external quantum efficiency of the photodetector.

The responsivity can be expressed in terms of wavelength 'λ' as:

$$R = \frac{\eta \lambda q}{hc} = \frac{\eta \lambda (\mu m)}{1.24} (A/W) \qquad (1-2)$$

The responsivities of commercially available wide bandgap based detectors such as diamond, SiC, and GaN are shown in Table 1-2 **(8)**. The responsivities of low band gap semiconductors

like Si and GaP also are shown in Table 1-2 for sake of comparison. The responsivity of the wide band gap based detectors shown in Table 1-2 is of the order of 10^{-1} A/W. Comparing the responsivity of wide band gap based detectors with the responsivity of low band gap semiconductors shown in Table 1-2, the responsivity of diamond and silicon carbide is higher and that of gallium nitride and aluminium gallium nitride lower than that of low band gap silicon and gallium phosphide based detectors. Now comparing these responsivities with a ZnO based UV detector (though a detector based on ZnO material is not available commercially), research studies showed that the responsivity was approximately of the order of $0.03\text{-}10^{2}$ A/W (**40, 42**). Thus the responsivity of the ZnO based UV detector is higher than other wide band gap detectors. One of the reasons for the high responsivity of ZnO is due to high exciton binding energy (60 meV). The exciton binding energy of other wide bandgap materials is less than 60 meV. Thus, the sensitivity of ZnO based detectors is high even at room temperature. ZnO material also is resistant to radiation exposure. The effects of radiation damage on ZnO

Table 1-2   Performance of commercial wideband gap detectors (8)

	UDT sensors UV001 to UV 100	IFW JEP5	Centronic PD1.4	CREE CD-260-0.3-D	APA Optics	APA Optics
Material	Si	GaP	Diamond	SiC	GaN	AlGaN
Spectral range (nm)	1100-200	200-520	130-225	219-380	365-200	280-200
Responsivity (A/W)	0.14 at 254 nm	0.15 at 440 nm	0.15 at 200 nm	0.19-0.13 at 275 nm	0.1 at 325 nm	0.03 at 275 nm
Raise time Fall time	0.2-5.9 µs	5 µs	-	-	-	-
Dark current	0.1 mA max	10pA at -5 V	<1 nA	0.2-2 fA at -1 V	1-100 nA At -0.5V	1-100 nA At -0.5 V

material was studied by Look et al **(16)**. These studies show that the electrical properties of ZnO are largely unaffected (acceptor concentration changes from 1.5 x 10^{15} cm^{-3} to 2 x 10^{15} cm^{-3}) up to a radiation dose of 1.6 MeV. Compared to other semiconductor materials like GaN, CdS, GaN and Si, ZnO suffers less radiation damage (33% change in carrier concentration) **(16)**. The thermal conductivity of ZnO is about 1.35 W/m/K which is higher than other wide band gap semiconductors. Hence, ZnO based detectors can be operated even in high temperature (>60^{0}C) and high radiation (>124 eV) environments **(1)**. From a fabrication aspect, ZnO detector fabrication is cheaper since ZnO can be grown by solution using the same process method on both organic and inorganic substrates. Inorganic substrates reported in literature for growth of ZnO are insulators like quartz, sapphire, glass, mica, fluorite, diamond, alumimium oxide, sodium chloride and on semiconductors such as silicon, galium arsenide, galium nitride and indium phosphide **(17-26)**. Organic substrates which can be used for ZnO growth are polyethylene terephthalate, polyethylene naphthalate, polyarylate, polyestersulfone, polycarbonate, polyimide, and polytetrafluoroethylene **(27-30)**. Organic substrates are flexible, lighter, sturdy, and durable. Hence, ZnO based sensors grown on these organic substrates can be easily integrated into micro/nanosystems and portable devices like smart cards, digital cameras, cell phones, camcorders, and personal digital assistants **(31, 32)**. Also, ZnO nanostructures can be grown in varied nonstructural configurations. However, other wide band gap semiconductors require high processing temperature (~ 1000^{0}C), sophisticated vacuum system, and are limited to grow in different nonstructural configuration. The other advantage of ZnO from a fabrication point of view is that the processing techniques are compatible with existing silicon technology. Thus, the characteristics of ZnO that makes it a unique material for UV detector can be summarized as high optical gain (4500 cm^{-1}), high thermal conductivity (1.35 W/m/K), high

exciton binding energy (60 meV), high temperature stability (2248 K), and ease of fabrication **(33-37)**.

1.5   DIFFERENT CONFIGURATION OF ZINC OXIDE THIN FILM UV DETECTOR

In semiconductor based photodetectors, the incident photons excite electrons from the valence band to conduction band thus forming an electron-hole pair. The electron hole pair can be separated by electric field formed by a p-n junction, Schottky barrier or external bias generating external photocurrent which is proportional to the incident photons. Hence, ZnO based detectors can be fabricated in different device configurations. Each configuration has its advantages as well as disadvantages. The device structure chosen will depend on the application of the detector. The different device structures are (1) photoconductors (2) metal-semiconductor-metal photodiodes (3) Schottky photodiodes and (4) p-n junction photodiodes.

1.5.1   Photoconductors

The photoconductor consists of semiconductor thin film with ohmic contact on it both ends. The schematic diagram is shown in Figure 1-1. On shining UV light of energy greater than the bandgap of the semiconductor, electron-hole pairs are produced and the applied bias drifts the electrons and holes in opposite directions before they combine. Thus, the current through the device increases with incident UV light. Here the resistance of the device is larger than the load resistance. The responsivity of semiconductor detector can reach about 1616 A/W (shown in Table 1-3). The drawback is that its UV/visible contrast is poor and the photoresponsivity has a sublinear relation with the incident power. Several authors have reported on photoconductor

based UV detector using semiconductor thin films prepared by different fabrication techniques. The performance of the photoconductor based UV detector prepared using different techniques is listed in the Table 1-3 **(38-42).** The responsivity, response and the dark current depend on the

.
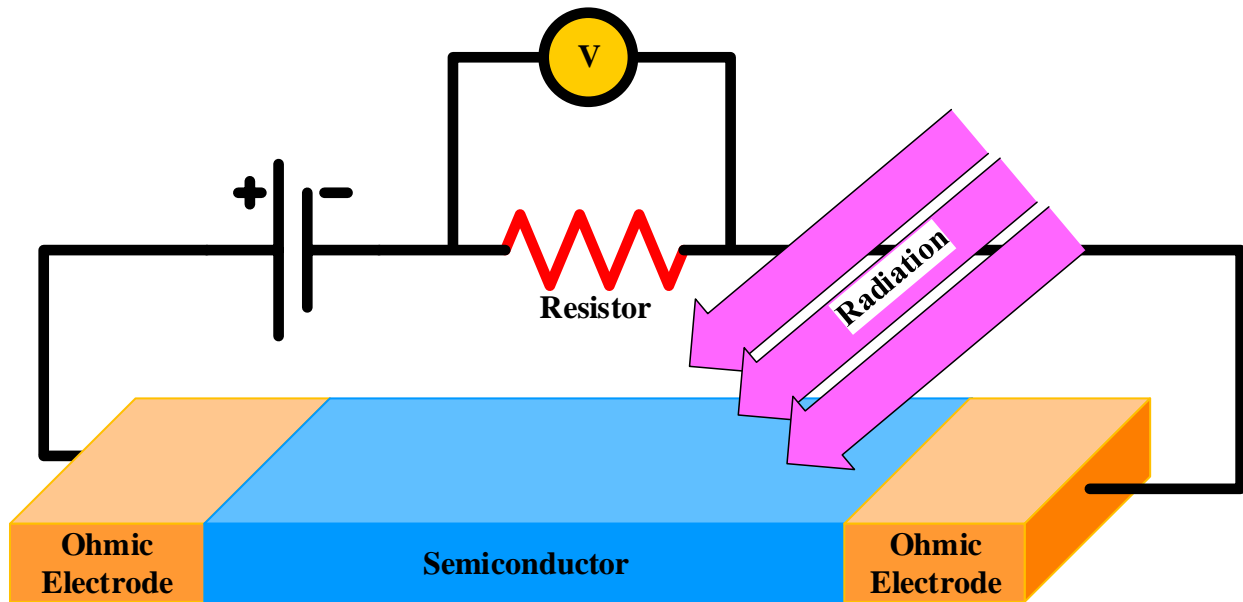
Figure 1-1   Schematic structure of photoconductor detector

Table 1-3   Performance characteristics of photoconductor detector

Fabrication Method	Electrodes	Dark Current μA	Responsivity (A/W)	Response time (µS)	Refe--rences
PLD	Al	200 (5 V bias)	-	50×10^6 (raise time) 120×10^6 (fall time)	**38**
MOCVD	Al	0.4 (5 V bias)	400 (5 V bias)	1 (raise time) 1.5 (fall time)	**39**
RF sputtering	Al, ITO	640 (5 V bias)	1616 (5 V bias)	0.071 (raise time) 377(fall time)	**40**
P-MBE	Al/Ti	10000 (5 V bias)	1.68 (20 V bias)	95×10^6 (raise time) 2068×10^6 (fall time)	**41**
Sol-gel	Au	800 (1.5 V bias)	0.03 (5 V bias)	160×10^6 (drop to 50% of its maximum value)	**42**

8

the fabrication technique used.

1.5.2 Schottky Photodiode

The structure of Schottky photodiode is shown in Figure 1-2. The Schottky photodiode has two metal–semiconductor contacts. One of the contacts acts as Schottky contact and the other contact acts as ohmic contact. The contact can be made Schottky or ohmic by choosing appropriate metals. For an n-type semiconductor, Schottky contact can be formed when the work function of the metal is greater than the work function of the semiconductor, while for p-type the work function of the metal should be less than the semiconductor. For forming an ohmic contact with n-type semiconductor, the work function of the metal should be less than the work function of
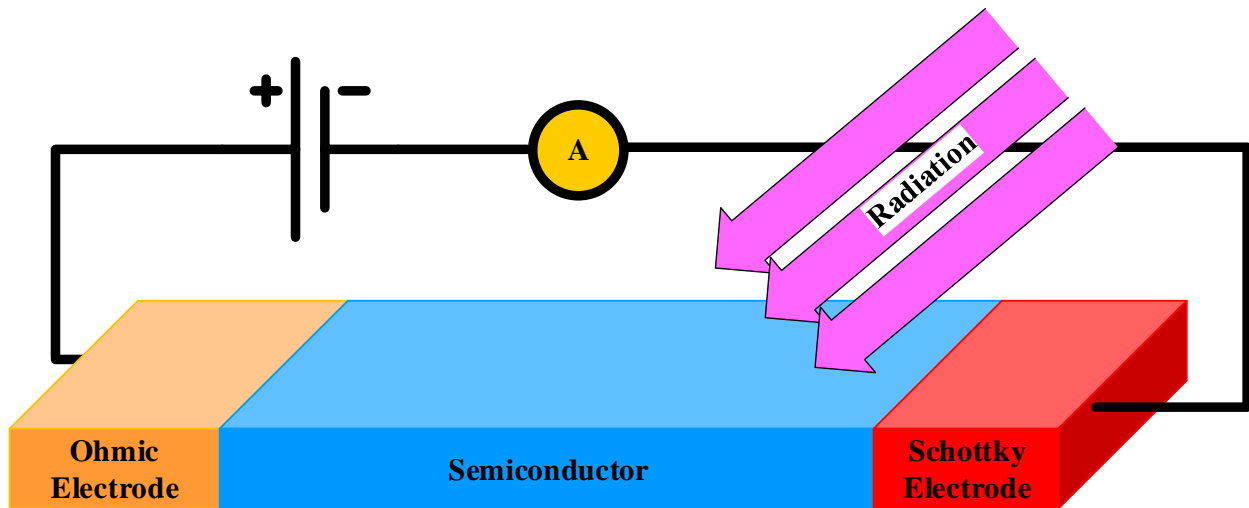
Figure 1-2 Schematic structure of Schottky photodiode detector

 the semiconductor. While, for p-type semiconductor the work function of the metal should be greater than the semiconductor. The advantage of a Schottky photodiode is that its dark current

is low (micro amps to nano amps) so less energy consumption, UV to visible ratio is high (10^3),

response is fast (micro sec to milli sec) but the drawback is that its responsivity is lower than

photoconductor based detector. The performance characteristics for Schottky photodiodes for

various metal contacts and semiconductor growth technique are shown in Table 1.4 **(43-46)**.

Table 1-4 Performance characteristics of Schottky detector (43-46)

Fabrication Method	Electrodes	Dark Current µA	Responsivity (A/W)	Response time (µS)	References
Sputtering	Au(Schottky) Mn(Ohmic)	1×10^{-3} (0.5 V)	1.7×10^3	20(raise) 30(fall)	**43**
Plasma assisted MBE	Au(Schottky) In(Ohmic)	10^{-2}	10^3 A (no res)	$1\sim2 \times 10^3$ (raise and fall)	**44**
Hydrothermal	Pt(Schottky) Al(Ohmic)	10^{-8} A/cm^2	0.185	-	**45**
Hydrothermal	PEDOT:PSS (Schottky) Ti(Ohmic)	10 A/cm^2 (2V)	0.48 (-0.6 V)	-	**46**

1.5.3 P-N Junction Photodiodes

A p-n junction photodiode is a p-n junction diode with a window on its encapsulation to allow

light to reach the junction of the diode. The p-n junction can be formed by sandwiching the same

semiconductor material doped to p-type and n-type. This diode is called p-n homojunction

photodiodes. If the junction is formed by using p-type and n-type of different semiconductor

material, it is known as the p-n heterojunction photodiode. The schematic structure of p-n

junction diode photodetector is shown in Figure 1-3. The metal contacts for p-n junction diode

are ohmic. The p-n homojunction junction diode performance of ZnO based detectors grown

under various growth conditions is shown in Table 1-5 **(47-49)**. In case of p-n junction diodes
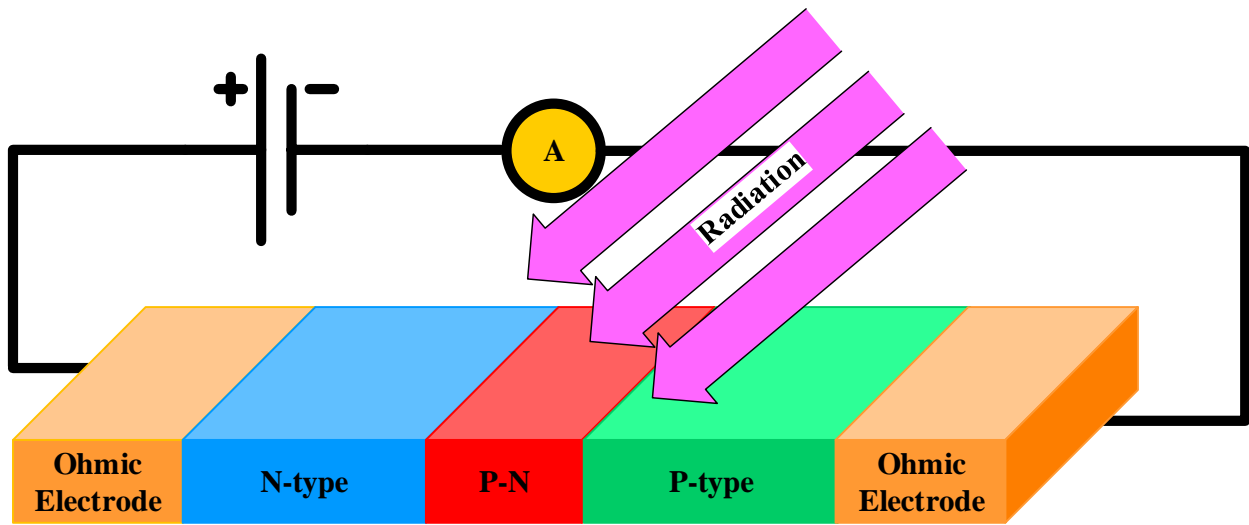
Figure 1-3   Schematic structure of P-N junction photodiode

Table 1-5   Performance characteristics of p-n homojunction detector (47-49)

Fabrication Method	Electrodes	Dark Current μA	Responsivity (A/W)	Response time (μS)	References
RF magnetron sputtering	In	-	2 mA(-2.7V)	-	**47**
Hybrid beam deposition	Ni/Ti	10^{-6} A/cm^2	0.3×10^{-10} A	-	**48**
MBE	Al/Ti	2×10^{-4} mA(-7 V)	26.4 mA (5 C)	-	**49**

the dark current is low (nano amps to micro amps) so less energy consumption, response is fast (nano sec to micro sec) but the drawback is that it's responsivity is lower than the photoconductor based detectors (< 90%). The other drawback of a p-n junction diode is that it's fabrication involves two times more processing steps compared to photoconductor and Schottky photodiodes.

11

1.5.4 MSM Photodiodes

MSM photodiodes consist of two Schottky diodes connected back-to-back. The MSM photodiode is formed using an interdigitated electrode fabricated on top of the active region of the detector. The schematic structure is shown in Figure 1-4. The fabrication of the MSM photodiode involves two times less steps than p-n junction photodiode, has simple structures and, due to low capacitance per unit area the response is faster (nano sec to milli sec). The drawback of the MSM photodiode is that the responsivity of the detector is reduced by 95% compared to photoconductor detector due to masking of the active region by the interdigitated electrodes
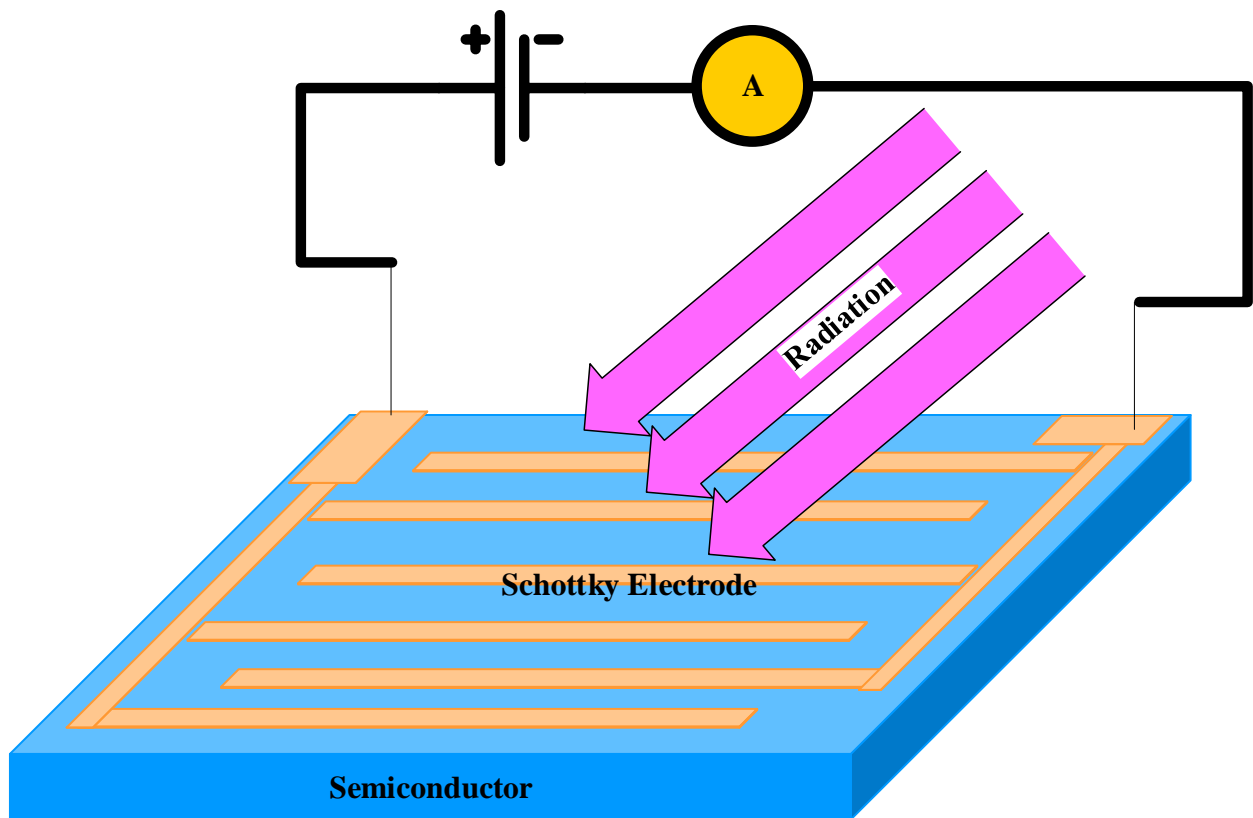
Figure 1-4   Schematic structure of MSM photodiode detector

Various authors have studied the response of MSM detector for metals like Ru, Cr, Al, Ni, Pt, Pd, Au, Ag **(14, 50-56)**. These studies showed that the response of the detector depended on the barrier height of the metal-semiconductor-interface. The barrier height depends on the work function of the metal. Metals with high work function give high Schottky barrier height. When barrier height is high, the leakage current is reduced, breakdown voltage increases, response time decreases and the photocurrent to dark current contrast improves. The drawback is that the responsivity and quantum efficiency decreases. The performance characteristics of MSM photodetector for various semiconductor growth conditions are shown in Table 1-6 **(14, 51, 52, 54).**

Table 1-6   Performance characteristics of MSM detector (14, 51, 52, 54)

Fabrication Method	Electrodes	Dark Current µA	Responsivity (A/W)	Response time (µS)	References
MOCVD	Ag	1×10^{-3} (5 V)	1.5 (5 V)	1.2×10^{-2} (raise time) 5×10^{-2} (fall time)	**14**
LAMBD	Au	8.85×10^{-2} (5 V)	11.3×10^{-6} (5 V)	-	**54**
ALD	Au	1×10^{5} (2 V)	0.7 (5 V)	-	**52**
RF sputtering	Ag/ZnO	-	3×10^{2} (5 V)	-	**51**

1.6   BEST CONFIGURATION FOR ZINC OXIDE UV DETECTOR

Comparing different photodetector structure configuration for the same active area, MSM detector structure is simple and fabrication involves two times less steps compared to p-n

junction and Schottky diode detector. Studies on MSM ZnO thin film based UV detector by Ji et. al. showed that the responsivity of the detector was enhanced by incorporation of ZnO nanorods **(57)**. By incorporation of ZnO nanorods, the responsivity of the detector enhanced from 0.13 A/W at 370 nm to 41.22 A/W at 370 nm **(57)**. The better response on incorporation of ZnO nanorods is due the following reasons (1) The life time of the carrier is enhanced due to large surface-to-volume ratio and presence of deep level traps on the surface of the rods, (2) the transit time of the carrier is reduced due to nano dimension of the rods (3) the absorption of light is reduced due to enhancement in optical path length from multiple reflection and scattering of light at the rough textured surface of the nanorods, and (4) carrier life time is increased due to oxygen adsoption and desorption at the surface of the ZnO nanorods **(58-63)**.

1.7 DETECTION MECHANISM OF ZINC OXIDE NANROD UV DETECTOR

When the ZnO rods are not exposed to UV light, oxygen from the atmosphere is adsorbed on the surface of the rods due to free surface states **(64-65)**. Figure 1-5(a) shows a schematic representation of the rod surface before it is exposed to UV light. The adsorbed oxygen on the surface traps free electrons of the n-type ZnO nanorod. This creates a depletion region near the rod surface as shown in Figure 1-5(a). The chemical reaction for the binding of the oxygen on the rod surface is shown in Eq (3) and Eq (4)

$$O_2 \, (g) + e- \rightarrow O^- \, (ad) \hspace{4cm} \text{Eq (1-3)}$$

$$O_2 \, (g) + 2e- \rightarrow O_2^{2-} \, (ad) \hspace{3.5cm} \text{Eq (1-4)}$$

When the rods are exposed to UV light, electron-hole pairs are formed due to band gap

14

excitation (Figure 1-5(b)). The electric field due to the depletion region at the surface of the rod attracts the holes formed by photo excitation to the surface. The holes on reaching the surface, combine with electrons bound to the oxygen atoms, thereby, releasing the adsorbed oxygen from the surface of the rod. The schematic representation of the electron-hole recombination at the rod surface is shown in Figure 1-5(c), and the reaction mechanism is shown in Eq (5) and Eq (6),

$$O^- \text{ (ad)} + h^+ \rightarrow O_2 \text{ (g)} \qquad\qquad\qquad \text{Eq (1-5)}$$

$$O_2^{2-} \text{ (ad)} + 2h^+ \rightarrow O_2 \text{ (g)} \qquad\qquad\qquad \text{Eq (1-6)}$$
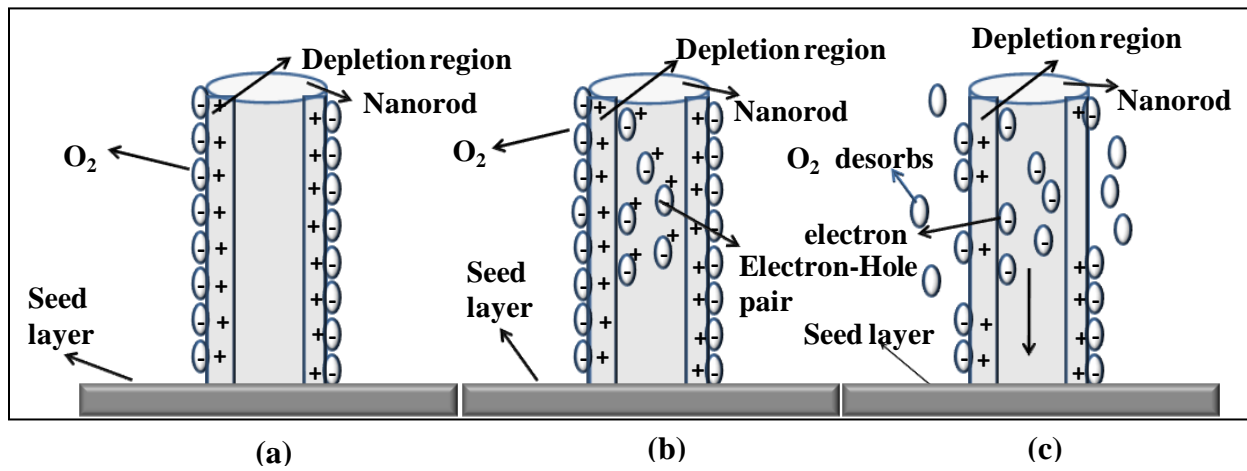
Figure 1-5   Schematic representation of the working mechanism of the ZnO NRs based photodetector (a) Formation of depletion region due to adsorption of oxygen on the NR surface (b) Generation of electron-hole pair on illumination with UV light (c) Desorption of oxygen due to recombination of hole with the electron of adsorbed oxygen ions (66).

The uncombined electron of the photogenerated electron-hole pair increases the concentration of the carriers in the rod. Hence, the concentration of the carriers in the rod is higher than the concentration of the carriers in the seed layer. This difference in the carrier concentration between rod and the seed layer causes the carriers to diffuse from the rod to the seed layer until the concentration between the rod and seed layer evens out. Thus, on exposure to UV light, the

concentration of the carriers in the seed layer increases, resulting in an increased current and this increase in current is directly proportional to the intensity of the incident UV light.

Though, MSM ZnO based detectors have the highest responsivity, the responsivity of these detectors can be affected by the ambient environment like temperature, pressure, and humidity. Thus for obtaining reliable results from these detectors, a stable environment should be maintained by means of external equipments. This would increase the cost of operation and net size of the detector system. If MSM detectors can be fabricated in such a way that the output of the detector depends on the ratio of the input bias, then the detector will have self calibration ability to offset the changes in the environment. A detector whose output is dependent on the ratiometric input can be realized if the detector can be operated by the Wheatstone bridge principle. This work is about the fabrication of the MSM ZnO based detector that can be operated in the Wheatstone bridge mode and its temperature stability. A newly designed interdigitated electrode pattern was used for the detector. The new pattern of the interdigitated electrode had a compact design with the fingers of the electrodes arranged in a square configuration that resembled a Wheatstone bridge. In order to understand how the newly designed pattern affected the responsivity of the detectors, a MSM detector similar to L. W. Ji et al. were fabricated (**57**). The new electrode pattern was used for the detectors. Detectors with electrodes having different dimensions and for different rod lengths were fabricated. Their I-V characteristics and transient responses of the fabricated detectors were studied. These studies gave useful insights about dependence of the responsivity on electrode dimension and length of the rods. With regard to the Wheatstone bridge structure, to determine the dependence of thermal stability on the symmetric nature of the four arms of the bridge (four arms of the bridge are

16

identical) and asymmetric bridge (four arms are not identical), devices were fabricated and their thermal stabilities were compared with a symmetric bridge.

The remaining chapters will discuss the optimization of ZnO rod growth, optimization of the Wheatstone bridge electrode dimension, fabrication and characterization of symmetric and asymmetric Wheatstone bridge, and concluded by fabrication and characterization of quasi-symmetric Wheatstone bridge.

2. OPTIMIZATION OF ZINC OXIDE NANOROD GROWTH

Compact devices have high market demand and to build compact devices with high performance, one way is to use nanotech. But the drawback of using nanotechnology is that the device fabrication may become more expensive. To keep the product cost at affordable level, fabrication techniques that are cheaper, less sophisticated and offer the feasibility for large scale production needs to be employed. For manufacturing compact devices, nanorods have become a promising enabling technology.

2.1 PROPERTIES OF ZINC OXIDE NANOROD

When it comes to choosing the best candidate from a pool of semiconductor materials for a nanorod-based device, ZnO outperforms all other materials due its unique combination of properties such as wideband gap, high binding energy, lack of center of symmetry, strong piezoelectric and pyroelectric properties, high binding energy of 60 meV and large electrochemical coupling ability. ZnO belongs to the II-VI semiconductor group with a wurtzite structure and has a bandgap of 3.3 eV [67-69]. Another positive attribute of ZnO material is that that it can be grown in many different shapes and sizes at nanoscale [70-72]. Hence, the optical and electrical properties of ZnO can be tailored [73-76]. ZnO structures can be realized in shapes such as nanobelts, nanotubes, nanowalls, nanodots, nanorods, nanowires, nanobridges, nanonails, polyhedral cages, nanohelixes, mesoporous single-crystal nanowires, and seamless nanorings [70-72]. Among these different nanostructures, nanorods and nanowires were more widely researched because of its ease of fabrication and for its device applications.

ZnO with its band gap of 3.3 eV, high exciton binding energy of 60 meV, high thermal conductivity, and high melting point makes it an excellent sensing element material for UV detection in high temperature applications ($> 60^0$C). High sensitivity (> 1 A/W) can be realized even at temperatures higher than room temperature with ZnO due to its high exciton binding energy of 60 meV. While the binding energy of other wide gap materials, which are also touted as excellent materials for UV detection application, are only 40 meV for ZnS, 25 meV for GaN, and 22 meV for ZnSe [68]. In addition to high responsivity, ZnO outperforms other materials in ease of fabrication.

2.2   GROWTH TECHNIQUES FOR ZINC OXIDE NANORODS

The different growth techniques employed for the growth of semiconductor nanostructures are phase transport technique, thermal decomposition of precursors, thermal oxidation of metal, metal organic vapor phase, and solution growth technique [68, 76-78]. Among these techniques, solution growth technique is cheapest and suitable for large scale production. The disadvantages for other techniques are moderate to high growth temperature and expense [76, 79, 80]. These techniques require costly insulating substrates for oriented growth and high vacuum deposition system. ZnO rods can be grown using a solution growth technique. Using solution growth, rods can be grown on cheaper substrates such as glass and plastic. Also, lack of stringent growth conditions and high vacuum makes this technique attractive and economical. In a solution growth technique, the density and diameter of the rod can be controlled by manipulating the density and size of the pre-deposited ZnO seed layer. The pre-deposited seed layer acts as the nucleation sites for the rods. Also, using solution growth, site specific growth is possible.

19

The dimension of the rod plays a crucial role in the responsivity of the UV detector. The responsivity of the detector can be improved by decreasing the diameter of the rods and by increasing the density of the rods [64]. The responsivity increases with a decrease in diameter of the rods because the total surface area increases when coupled with increased density, thereby, the amount of UV absorption increases. Also, the responsivity increases with decrease in diameter because the volume decreases, so the excited electron density increases. The UV adsorption per unit area can be increased by increasing the density of the rods. Both the density of the rods and diameter of the rods can be controlled in solution growth technique. The details of how the diameter and density can be controlled are explained in Section 2.3.

2.3 SYNTHESIS OF ZINC OXIDE NANORDS BY SOLUTION GROWTH

ZnO nanorods were synthesized by employing a two step hydrolysis process. The first step involved the deposition of the seeds on the substrate. The ZnO seeds served as the nucleation sites for the rod growth. The ZnO seeds were prepared from zinc acetate (Zn $(CH_3COO))_2$, Alfa Aesar, 99.98%) and ethanolamine ($HOCH_2CH_2NH_2$, Alfa Aesar, 99%) dissolved in ethanol solvent (Sigma Aldrich, 99.5%). In the next step the rods were grown by immersing the substrate coated with seed layer in an aqueous solution prepared by dissolving zinc nitrate hexahydrate ($Zn(NO_3)_26H_2O$, J. T. Baker, 99-100%) and hexamethylenetetramine (($CH_2)6N_4$, J. T. Baker, 99%) in distilled water and heating it in oven [81].

2.3.1 Preparation of Zinc Oxide Seed Layer

The ZnO seed layer served as the nucleation sites for the growth of vertical ZnO rods. The ZnO

seed layer solution was prepared by adding zinc acetate and ethanolamine in ethanol solution and stirring it for 1 hour at 75^0C. The solution was stored for one day to allow the sediments to settle. Then the seed layer solution was repeatedly spin coated for five times onto a Si/SiO$_2$ wafer. Prior to each coating the solvents from the spin coated film were removed by annealing the wafer at 170^0C. The seed layer solution was repeatedly spin coated for five times for uniform coverage of the seeds on the substrate. Each layer was spin coated at 1000 rpm for 20 sec. Then the wafer was annealed at 350^0C for two hours. On annealing at 350^0C, the zinc acetate decomposed into zinc and acetate. The acetate, ethanolamine and ethanol evaporated off. The zinc left behind on the wafer reacted with the oxygen in the atmosphere to form ZnO seeds. The radius of the grown nanorods depended on the size of the ZnO seeds. The size of the ZnO seeds was controlled by adjusting the concentration of the ethanolamine in the seed layer solution. The ethanolamine was added in the solution for the stabilization of the solvent. The ethanolamine formed a capping layer around the zinc acetate seeds which prevented the aggregation of the zinc acetate seeds as well as it improved the miscibility of the zinc acetate in the ethanol solvent. The density of ZnO rod growth was controlled by controlling the density of seeds on the wafer. The density of the seeds on the wafer was controlled by varying the concentration of the zinc acetate in the ethanol solution.

To know the optimal zinc acetate concentration in the ethanol solution that could give high density of ZnO seeds deposition on the wafer as well as a seed layer of uniform thickness on the wafer, seed layer solutions for different concentrations were prepared by varying the amount of zinc acetate in ethanol. The concentration of zinc acetate in the ethanol solvent was varied from 0.01 M to 0.1 M. The solution became supersaturated for concentrations higher than 0.1 M. The

concentration of the ethanolamine in the seed solution was maintained such that the ratio of ethanolamine and zinc acetate was a 1:1 ratio. The surface of the seed layer coated from seed layer solution for concentrations mentioned above was examined using an SEM (Philips, XL30 scanning electron microscope). The size of the seeds on the wafer were controlled by varying the concentration of ethanolamine in the solution. Seed layer solutions for different ethanolamine concentrations were prepared with zinc acetate concentration maintained at 0.1 M. The concentration of the ethanolamine was varied from 0.05 M to 0.3 M. The SEM analysis of the seed layer prepared for different concentrations of zinc acetate and ethanolamine will be discussed later in Section 2.4.1.

2.3.2   Preparation of Zinc Oxide Nanorods

Once the best condition out of the various chemical concentration studied for the ZnO seed layer preparation were determined, rods were grown on the seed layer by suspending the seed layer in zinc nitrate hexahydrate and hexamethylenetetramine aqueous solution and heating it in an oven at 90^0C for 4 hours. In the aqueous solution, zinc nitrate dissociated into zinc ions and nitrate ions and hexamethylenetetramine reacted with water to form ammonia. Ammonia formed in the aqueous solution dissociated into ammonium ion and hydroxyl ions. The hydroxyl ions reacted with zinc ions to form ZnO(s). The reaction mechanism is shown below,

$$Zn(NO_3)_2 = Zn^{2+} + NO_3^{2-} \hspace{5cm} Eq\ (2\text{-}1)$$

$$(CH_2)_6N_4 + 6H_2O = 6HCHO + 4NH_3 \hspace{4cm} Eq\ (2\text{-}2)$$

$$NH_3 + H_2O = NH_4^+ + OH^- \hspace{5cm} Eq\ (2\text{-}3)$$

$$2OH^- + Zn^{2+} = ZnO\ (s) + H_2O \hspace{4.5cm} Eq\ (2\text{-}4)$$

The rods were grown for different concentrations of the rod growth solution by varying the concentration of the hexamethylenetetramine from 0.015 M to 0.035 M with the concentration of the zinc nitrate hexahydrate maintained at 0.025 M. The influence of the seed orientation on the rod growth was also examined by orienting the seed layer horizontally as well as vertically in the growth solution. The schematic representation of the ZnO seed layer in the ZnO nanorod growth solution is shown in Figure 2-1. Figure 2-1(a) shows the horizontal orientation of the seed layer and Figure 2-1(b) for vertical orientation of the seed layer.

The rods grown for different concentrations of nanorod growth solution and orientation of the seed layer were examined using SEM for surface analysis, XRD for structural analysis (Rigaku X-ray diffractometer with CuKα radiation of wavelength 1.541874 Å) and EDAX for composition analysis (Philips, XL30 scanning electron microscope).
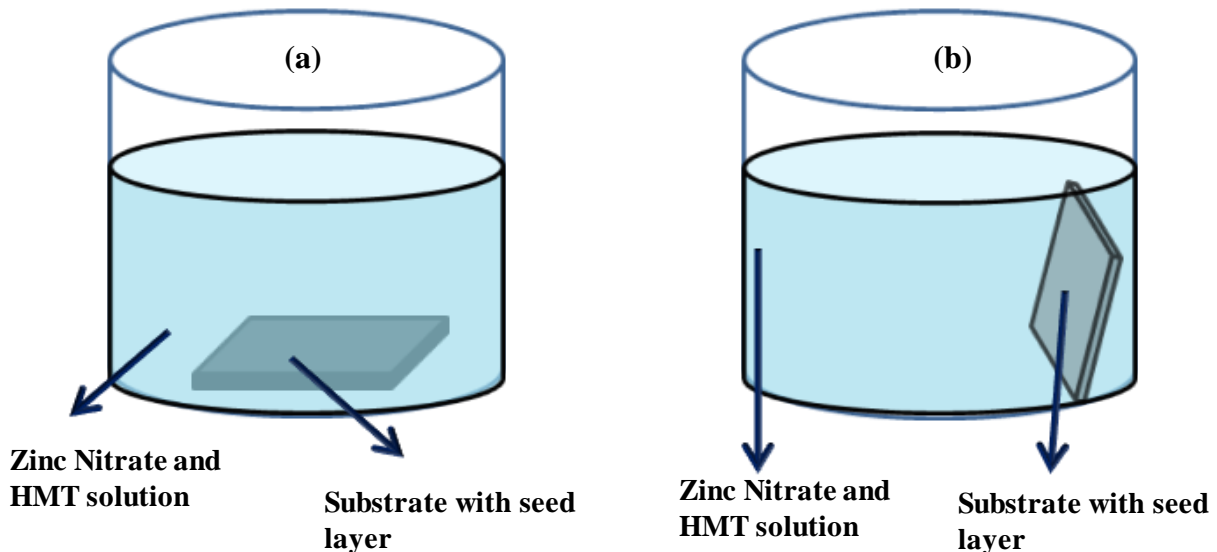
**Figure 2-1   Orientation of seed layer in the ZnO nanorod growth solution
(a) Horizontal (b) vertical**

2.4 CHARECTERIZATION OF ZINC OXIDE SEED LAYER AND RODS

2.4.1 SEM Characterization of the Seed Surface

The seed layer surface prepared for seed layer solutions with zinc acetate concentrations varied from 0.01 M to 0.1 M and ethanolamine concentrations the same as that of zinc acetate concentrations (i.e., the ratio of zinc acetate to ethanolamine concentration was 1:1) was examined using SEM . The seed layer had uniform coverage when the zinc acetate concentration was 0.1 M. The surface looked identical to the SEM image shown in Figure 2-2(a). While for other zinc acetate concentrations the surface image looked similar to Figure 2-2(c). The white spots in the image were the accumulation of ZnO seeds due to non-uniform coverage of the zinc acetate after spin coating, which on annealing at 350^0C was converted to ZnO.

The SEM images of the seed layer surface prepared for ethanolamine concentrations varied from 0.05 M to 0.3 M with zinc acetate concentration at 0.1 M is shown in Figure 2-2. The seed layer had uniform coverage for ethanolamine concentrations of 0.05 M and 0.1 M. While for the remaining ethanolamine concentrations the ZnO seeds were non-uniformly covered. The white spots seen on the surface were accumulations of ZnO seeds due to uniform coverage of the zinc acetate during spin coating. This showed that 0.05 M or 0.1 M could be used for preparation of uniform seed layer, but 0.1 M was used for seed layer because it would provide better capping of the zinc acetate seeds in the solution. Better capping of zinc acetate seeds in the solution gave ZnO seeds with sizes in the order of nanometer. Thus, the optimized concentration for seed layer solution preparation was zinc acetate (0.1 M) and ethanolamine (0.1 M) in ethanol and spin coated at 1000 rpm for 20 sec.

24
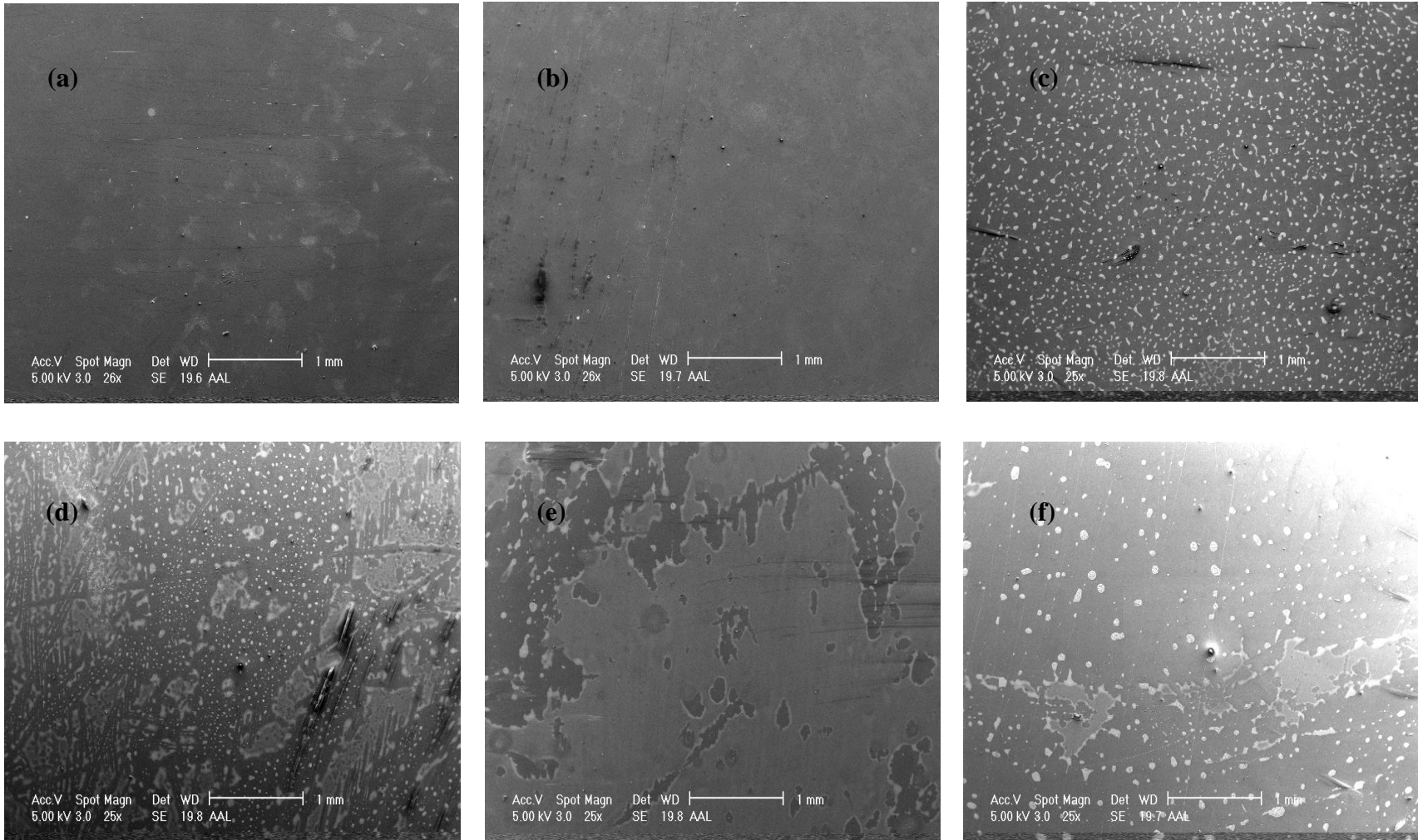
Figure 2-2   SEM image of the spin-coated seed layer for different ethanolamine concentration with a fixed concentration of zinc acetate at 0.1 M: (a) 0.05 M, (b) 0.1 M, (c) 0.15 M, (d) 0.2 M, (e) 0.25 M, and (f) 0.3 M [82].

The magnified SEM image of the ZnO seed layer prepared for optimized concentration after storing for one day is shown in Figure 2-3(a). The seeds had a diameter of 20-30 nm. To know whether the seed size was affected if the seed solution was stored for longer days, a seed layer was prepared after storing the solution for one month. The SEM image of the seed layer prepared after storing for one month is shown in Figure 2-3(b). Comparing Figure 2-3(a) and Figure 2-3(b) showed that the size of the seeds got bigger if the seed layer solution was stored for more
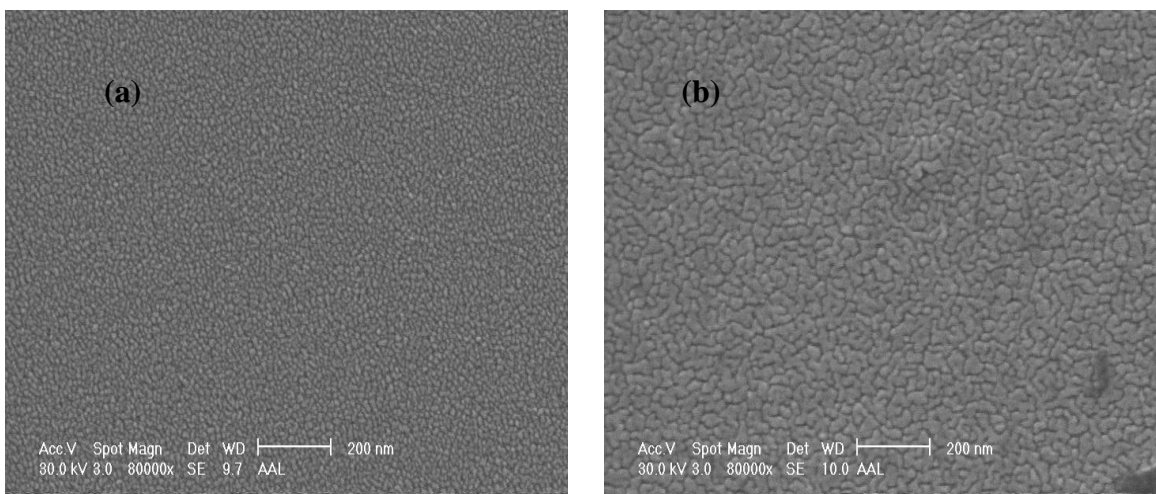
Figure 2-3   SEM image of the seed layer (a) Prepared after storing the solution for one day (b) after storing the solution for one month [82].

days. The increase in size of the seeds might be due to the coalescence of the smaller seeds. Thus for the growth of smaller diameter nanorods it would be better to use a freshly prepared seed layer. The seed layer prepared for this work's experimental studies were prepared from seed layer solutions that were not stored for more than a day.

2.4.2   SEM Characterization of the Zinc Oxide Rods

Rods were grown for both vertical and horizontal orientations of the seeded substrate in the

growth medium for different concentrations of hexamethylenetetramine (0.015 M, 0.02 M, 0.025 M, 0.03 M, and 0.035 M), while the concentration of zinc nitrate hexahydrate was fixed at 0.025 M. SEM studies showed that irrespective of the orientation and concentration of the growth medium the rods had the same diameter of about 30-40 nm, spacing of 20-40 nm, length of about 0.5 μm and shaped hexagonally. SEM images for 0.035 M hexamethylenetetramine concentration for both vertical and horizontal orientation are shown in Figure 2-4. The SEM images for the remaining concentrations and orientations looked similar to the images shown in Figure 2-4. One of the disadvantages of orienting the seeded layer horizontally in the growth medium was that the ZnO particles having sizes of the order of micrometers precipitated out from the solution and settled on the surface. Figure 2-5 shows the ZnO particles that settled on
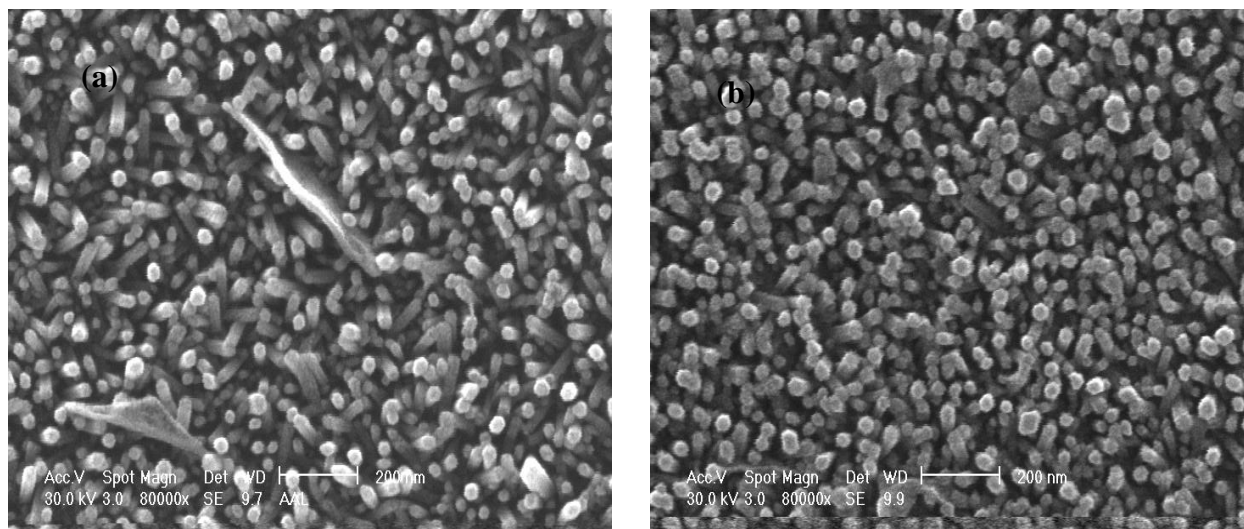
Figure 2-4   SEM images of the ZnO NRs grown with concentration of hexamethylenetetrami- -ne at 0.035 M and zinc nitrate hexahydrate at 0.025 M. (a) Horizontal orientation of the seed layer. (b) Vertical orientation of the seed layer [82].

the surface. The shape of the particles that settled on the surface depended on the concentration of the growth medium. Figure 2-5(a) shows the SEM image of the surface of the nanorods

grown from growth medium having HMT at 0.035 M and zinc nitrate at 0.025 M. The particles are cylindrical in shape. The SEM image of the surface of nanorods grown from growth medium having HMT at 0.015 M and zinc nitrate at 0.025 M is shown in Figure 2-5(b). The particles shown in Figure 2-5(b) are spindle shaped. The cause for the particles to grow in spindle shape might be due to low concentration of zinc ions, therefore there might not be enough ions that
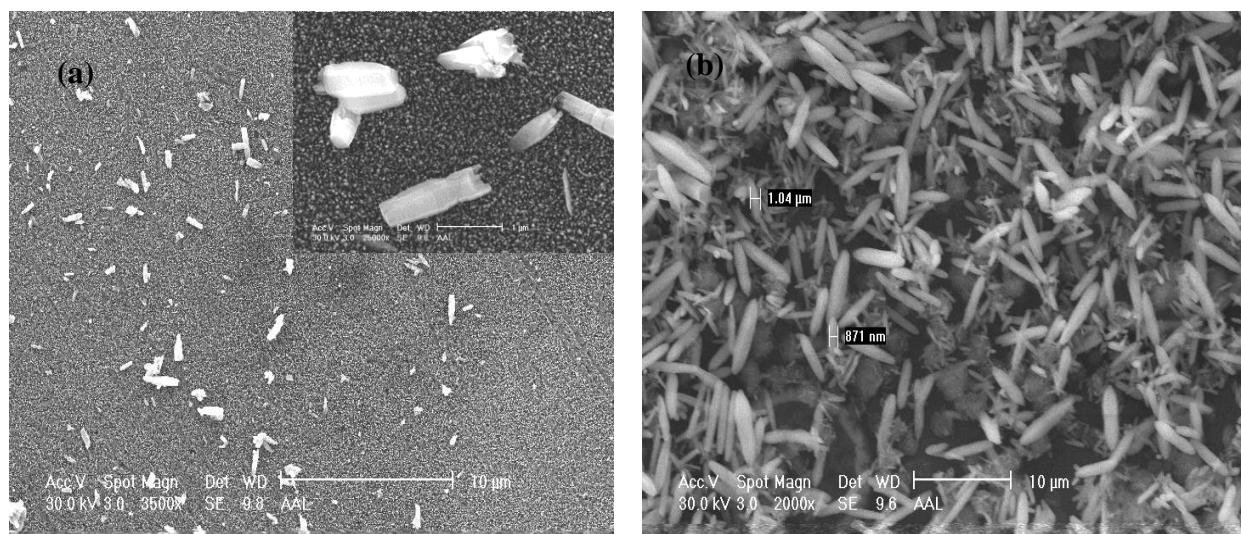
Figure. 2-5   SEM image of the ZnO particles that settles on the surface of ZnO nanorod film from the growth solution (a) 0.035 M of HMT (b) 0.015 M of HMT. Inset in Figure 2-5(a) shows the magnified image of the ZnO particles on the surface of the ZnO nanorod film [82].

were actually required as per the reaction rate at 90^0C. This resulted in a non-uniform growth of the particles along the axial direction resulting in spindle shape.

2.4.3   Structural and Compositional Analysis of Zinc Oxide Nanorods

A material can be identified if the planes of the material are determined. The planes of the material can be determined using X-ray diffraction (XRD) with Rigaku X-ray diffractometer

with CuKα radiation of wavelength 1.541874 Å. The XRD pattern of the rods grown for different orientations of the seeded substrate and concentration of the growth medium are shown in Figure 2-6. Figures 2-6(a), 2-6(b) and 2-6(c) represent the horizontal orientation of the seed layer in growth medium for HMT concentrations of 0.035 M, 0.025 M, and 0.015 M. The XRD spectra of rods grown with seed layer orientation perpendicular in the growth medium with concentrations 0.035 M, 0.025 M, and 0.015 M are shown in Figure 2-6(d), 2-6(e) and 2-6(f), respectively. Each peak in the spectrum represents the planes in the material investigated. The planes determined from the spectrum matched the planes for ZnO (ICDD no. 00-036-1451). A schematic representation of the structure and few of the planes of ZnO are shown in Figure 2-7. ZnO has a hexagonal wurzite structure. The (002) plane of the ZnO are planes perpendicular to c-axis. Hence the presence of peaks corresponding to (002) planes in the spectrum was an indication that the rods were aligned perpendicular to the substrate. The remaining peaks of the spectrum corresponded to the other planes of ZnO. When other peaks appeared in the spectrum, it was an indication that there were rods aligned parallel to the substrate. But the SEM image shown in Figure 2-4 shows that the rods were aligned perpendicular to the substrate. Hence, these peaks could be from particles that crystallized from the growth medium and settled on the surface parallel to the substrate. Now by comparing the XRD peaks for different concentration of growth medium and seed layer orientation few conclusions were drawn. Comparing the XRD spectra shown in Figure 2-6(a), 2-6(b) and 2-6(c) for seeds oriented horizontally in the growth medium, peaks corresponding to (002) planes were present in all the three spectrum. But the difference between these spectrums was that the intensity of the peak (100) varied with the concentration of HMT. The intensity of the (001) peak increased with decrease in HMT concentration. The increase in intensity of the (001) peak was due to the formation of ZnO

29
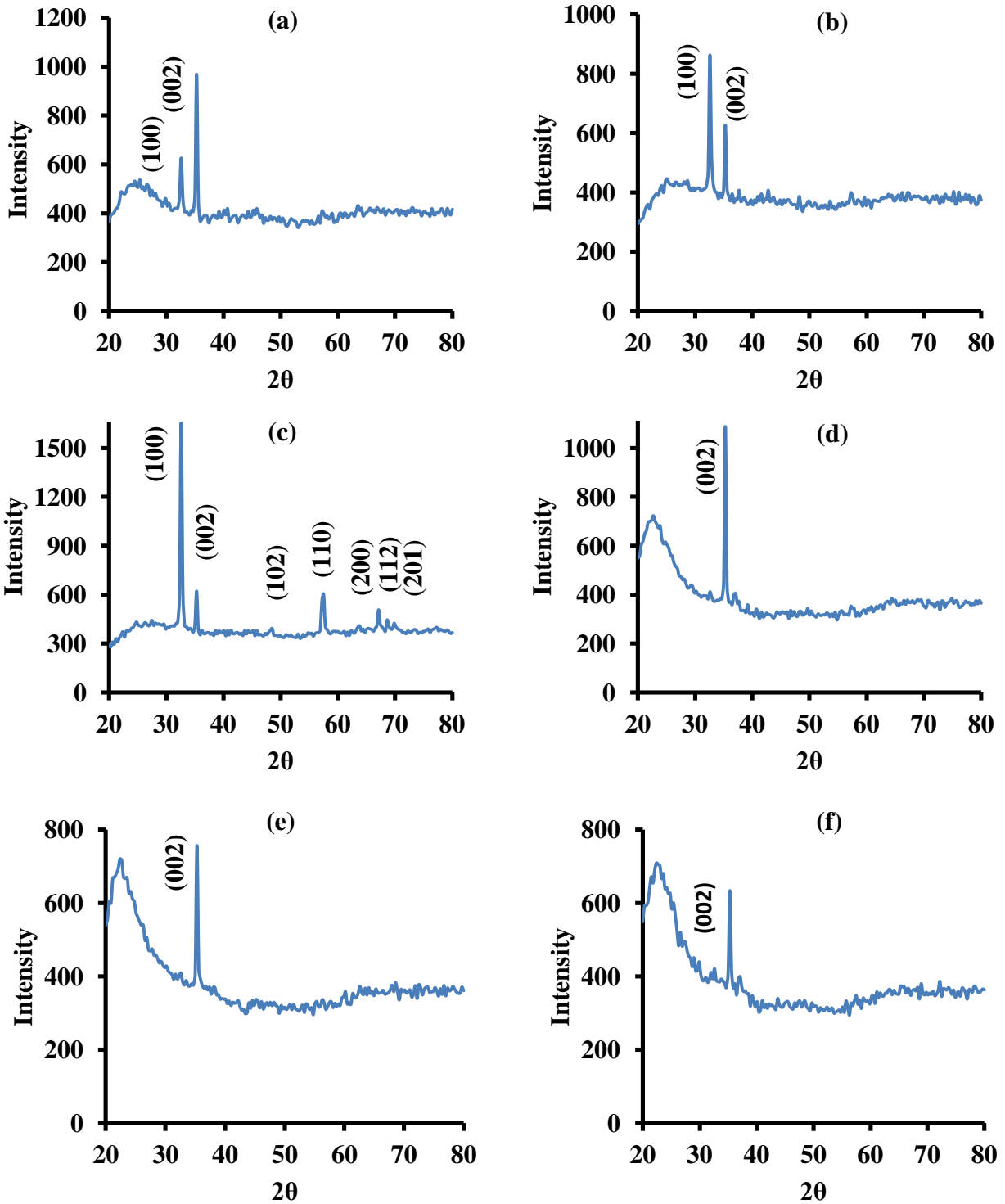
Figure 2-6   XRD patterns of ZnO NRs grown with the seed layer oriented horizontally and vertically for different HMT concentration and zinc acetate at constant molar concentration of 0.025 M. Horizontal orientation (a) 0.035 M, (b) 0.025 M, and (c) 0.015 M, and vertical orientation (d) 0.035 M, (e) 0.025 M, and (f) 0.015 M [82].
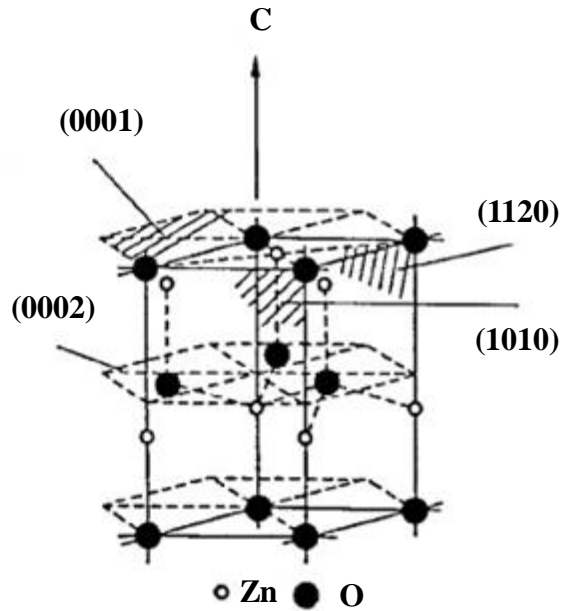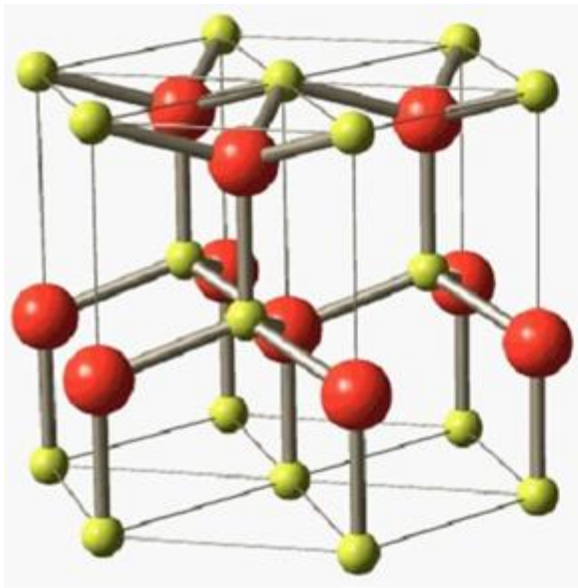
Figure 2-7   Schematic representation of the ZnO structure and its planes [Zn (red spheres) and oxygen (yellow spheres)] (83, 84)

particles and confirmed from the SEM image shown in Figure 2-5(b). The amount of particles crystallized increased with decrease in HMT concentration. When the spectra for the seed orientation horizontal and vertical were compared, for vertical orientation there were only (002) peaks. The (100) peaks were not seen in the spectrum for vertical orientation indicating that the settling of particles was avoided if the seed layer was oriented vertically. When growing the rods for UV detector application the deposition of these particles should be kept to a minimum because these particles can prevent the UV light from reaching the nanorods. As a result the responsivity of the detector will be affected. By orienting the seed layer vertically in the growth solution and using HMT of 0.035 M and 0.025 M of zinc nitrate hexahydrate, the best condition to avoid the settling of the particles on the surface of the nanorods was determined.

For further confirmation of the identity of the grown rods, the composition of the rods prepared

under various conditions was determined using EDAX analysis. Figure 2-8(a) shows the EDAX

spectrum of ZnO rods grown for vertical orientation of the seed layer with HMT 0.035 M and
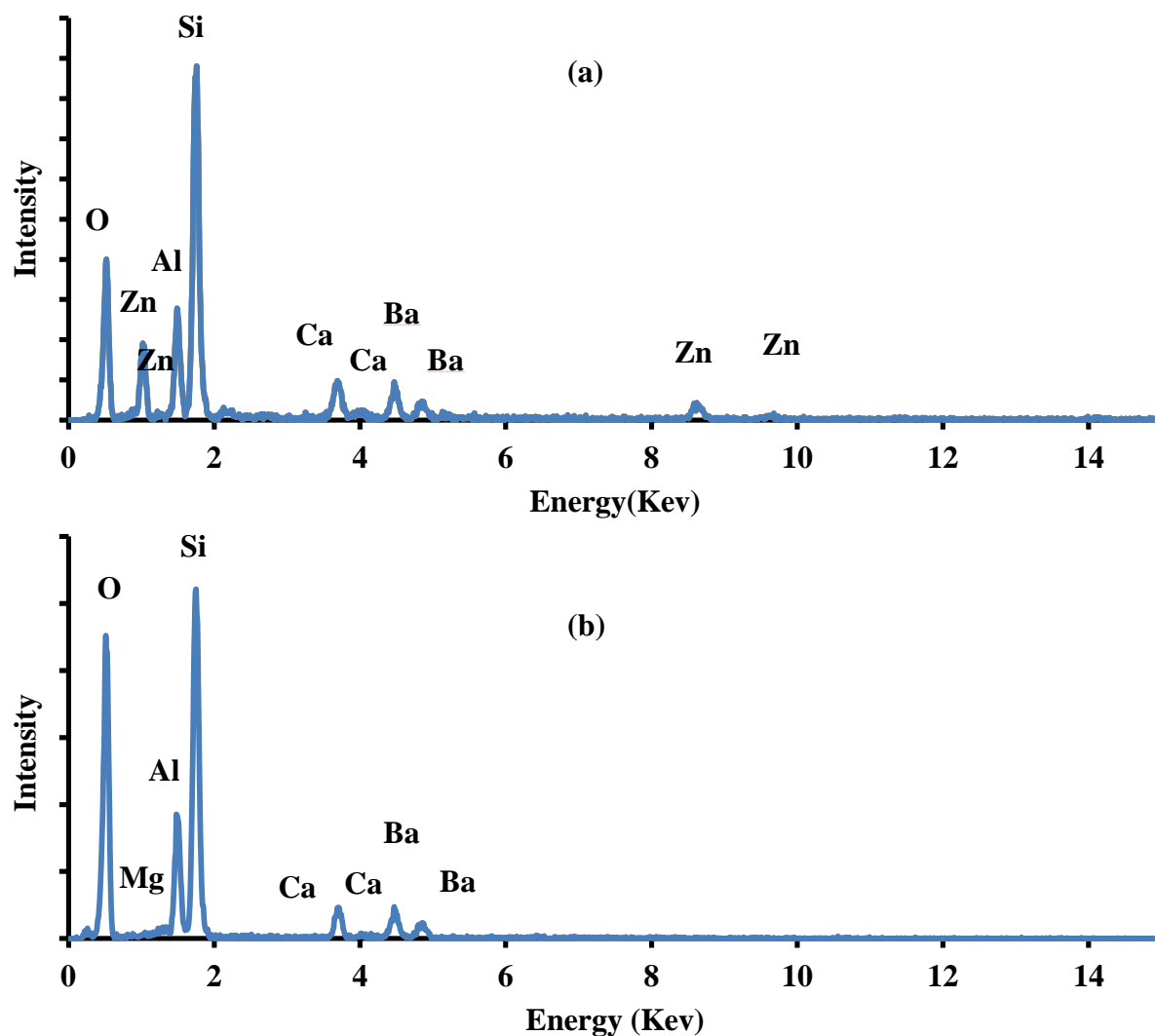
Figure 2-8   EDAX spectrum of (a) ZnO NRs on vertical orientation of seed layer grown with concentration of HMT 0.035 M and zinc nitrate hexahydrate at 0.025 M (b) substrate [82].

zinc nitrate 0.025 M. The spectrum confirmed the rods were made of zinc and oxygen. The

remaining peaks in the spectrum were from materials embedded in the substrate. Figure 2-8(b)

shows the EDAX spectrum of the substrate and this confirmed the presence of peaks other than zinc and oxygen in the EDAX spectrum shown in Figure 2-8(a). The spectrum obtained for the different orientation and concentration showed the presence of zinc and oxygen. The EDAX spectrum remained the same irrespective of the concentration of HMT and orientation of the seed layer. This meant that the density of the rod growth was unaffected by the orientation of the seed in the growth medium and the concentration of the growth medium. Hence, the decrease in intensity of the (002) peaks with decrease in HMT concentration could be due to decrease in crystallinity.

Thus, the optimum growth conditions of both the seed layer and nanorods were determined. ZnO seeds with size on the order of 20-30 nm were obtained for a zinc acetate concentration of 0.1 M and ethanolamine of 0.1 M in ethanol solution. While the optimum growth condition for rod growth was 0.035 M hexamethylenetetramine and 0.025 M of zinc nitrate hexahydrate with the seed layer oriented vertically in the growth medium.

3.   OPTIMIZATION OF WHEATSTONE BRIDGE ELECTRODES

Studies by different authors have shown that incorporation of nanorods improves the performance of ultraviolet detection (57, 85). The enhancement in UV detection with the incorporation of nanorods is due to the increase in carrier life time. Also, the reduced dimensionality of the active area in nanorod incorporated devices decreases carrier transit time, which in turn enhances the UV response (58-60). ZnO nanorod based metal-semiconductor-metal based detector fabricated by Ji et.al had responsivity of 40 A/W (57). Furthermore a high responsivity was achieved using solution grown ZnO nanorods using a simple metal-semiconductor-metal structure. Use of solution grown rods and simple metal-semiconductor-metal structure makes it feasible for large scale production as well as it is economical. Ji et. al. reported the responses of the detectors at room temperature (57). As described in the first chapter, the high response of ZnO based detector is due to electron-hole separation at the surface by the depletion region at the rod surface because of oxygen absorption. Studies have shown that the response of the ZnO based detector is affected by ambient conditions like temperature, pressure and humidity (86-89). The effects of changes in ambient conditions can be negated if the detector is operated in a Wheatstone bridge mode because in the Wheatstone bridge mode operation the output is the ratio of input. For fabrication of a Wheatstone bridge based detector a specially designed interdigitated electrode pattern needed to be used. The pattern of the interdigitated electrode in this work had compact design with the fingers of the electrodes arranged in square form that resembled a Wheatstone bridge. In order to understand how the newly designed pattern affected the responsivity of the detector, a MSM detector similar to Ji et. al. was fabricated with a new electrode pattern (57). Detectors with electrodes having different

dimensions and for different rod dimensions were fabricated. Their I-V characteristics and the transient responses of these devices were studied. These studies gave useful insights about dependence of detector responsivity on electrode dimension, length of the rod, crystallinity of the rods, and diameter of the rods, density of rods, and dimensions of the interdigitated electrode.

3.1   SIMPLE MSM UV DETECTOR

3.1.1   Structure of Simple MSM UV Detector

A simple MSM detector was fabricated on Si/SiO$_2$ wafer so that device integration into a system module was easier using the existing silicon integration technology. The structure of the fabricated ZnO based MSM ultraviolet detector is shown in Figure 3-1(a). The cross sectional view of the detector is shown in Figure 3-1(b). The structure of the simple MSM detector fabricated consisted of a ZnO seed layer spin coated over Si/SiO$_2$ wafer. ZnO rods which acted as the sensing element for the UV detection was grown over the ZnO seeds, which served as nucleation sites for the rod growth. The interdigitated electrode Wheatsone bridge pattern
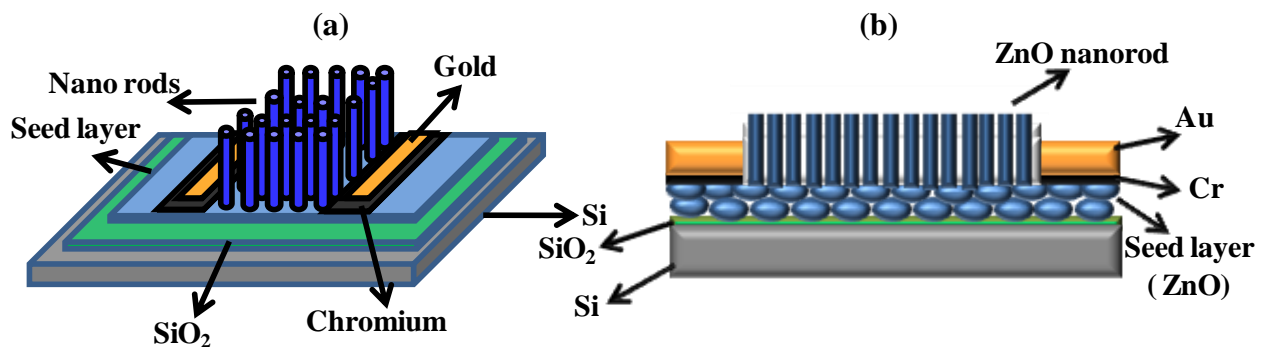
Figure 3.1   Structure of simple ZnO based MSM UV detector (a) top view (b) cross-sectional view (66).

35

consists of successive layers of chromium and gold grown over the ZnO seed layer. Chromium was used to improve adhesion of gold over ZnO seed layer.

3.1.2 Fabrication of Simple MSM UV Detector

The ZnO seed layer was prepared on the Si/SiO_2 wafer by spin coating seed layer solution prepared by dissolving 0.1 M zinc acetate and 0.1 M ethanolamine in ethanol solution by stirring for 1 hour at 75^0C, thereafter, storing for one day. The ZnO seed layer solution was repeatedly spin coated in succession for five times for uniform coverage of the seeds. Prior to each coating of the seed layer, the wafer was annealed at 170^0C to remove solvents from the film. The seed film was then annealed at 350^0C for 2 hours. On annealing, zinc acetate seeds were converted to ZnO seeds due to a reaction with atmospheric oxygen. Then, the Wheatstone bridge shaped electrode was patterned over the ZnO seed layer using a photolithography and lift-off technique. The electrode consisted of successive layers of 5 nm chromium and 100 nm of gold deposited using thermal evaporation at a deposition rate of 0.4 nm per sec. After the fabrication of the electrode on the seed layer, the sample was immersed in the nanorod growth solution prepared from 0.035 M of hexamethylenetetramine and 0.025 M of zinc nitrate and aged in oven at 90^0C for 4 hours. Instead of fabricating the electrode using an etching technique, a lift-off technique was used because the ZnO rods failed to grow on the seed layer after electrode fabrication using etching.

To determine the reason for the lack of ZnO growth on seed layer after electrode deposition and etching, three test samples with the following conditions were prepared: (1) seed layer coated with 5 nm chromium and 100 nm gold (2) seed layer coated with 100 nm gold, and (3) seed

layer. The metals on samples 1 and 2 were etched away using their respective etchants. After etching, samples 1 and 2 along with sample 3 were immersed in the same nanorod growth solution and aged in oven at 90^0C for 4 hours. SEM images of the samples 1 and 2 are shown in Figure3-2(a) and 3-2(b), which shows that the ZnO rods did not grow on the seed layer after using the gold or chromium etchant. However, ZnO rods grew on sample 3 which was not immersed in an etching solution.
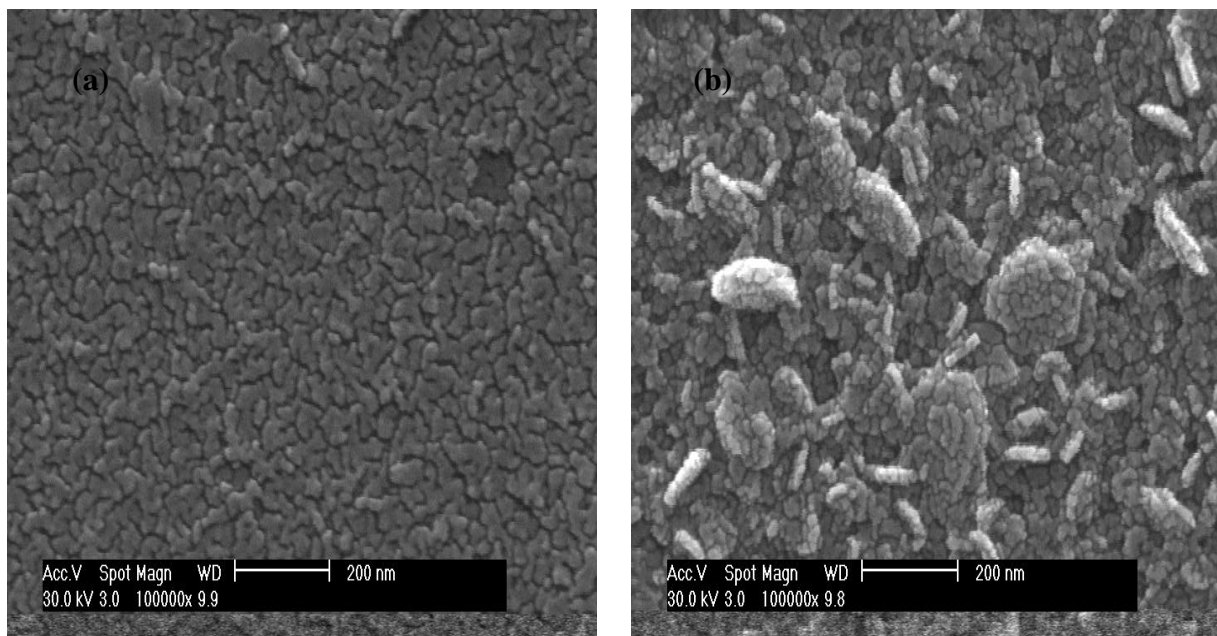
Figure 3.2   SEM images of test samples 1 and 2 after aging in nanorod growth solution for 4 hours (a) sample 1 (b) sample 2

Figure 3-3 shows the SEM image of sample 3, which was the seed layer not immersed in etchant solution. Thus, the etchant solution or the metal deposition on the surface modified the surface of the seed layer preventing the growth of nanorods. Hence, the electrodes were fabricated using a lift-off technique.

The schematic of the fabrication procedure is shown in Figure 3-4. To study the dependence of detector responsivity on the dimension of electrode, four electrode patterns having different dimension were used. The patterns used for the study are labeled as L_1, L_2, L_3 and L_4. Dimensions of the patterns L_1, L_2, L_3 and L_4 are shown in Table 3-1, and an image of the fabricated pattern on Si/SiO$_2$ wafer is shown in Figure 3-5. Also, to determine any dependence of detector response on dimensions of the nanorods, ZnO nanorods were grown for different
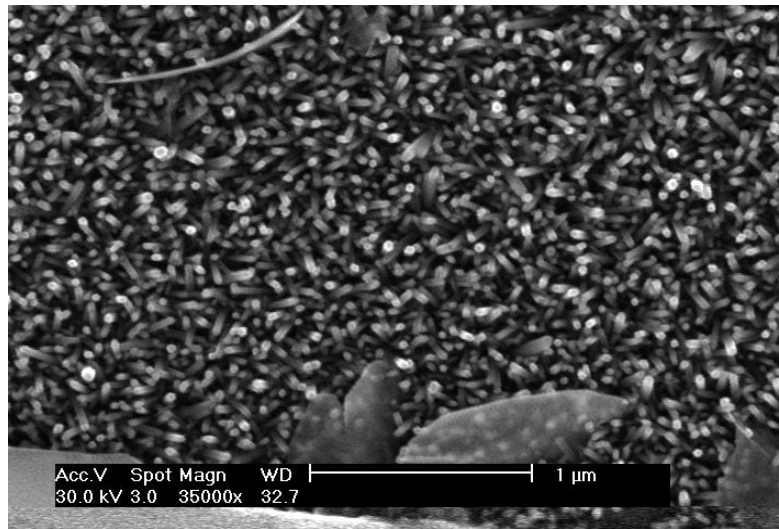
Figure 3.3   SEM images of test sample 3 after aging in the nanorod growth solution for 4 hours
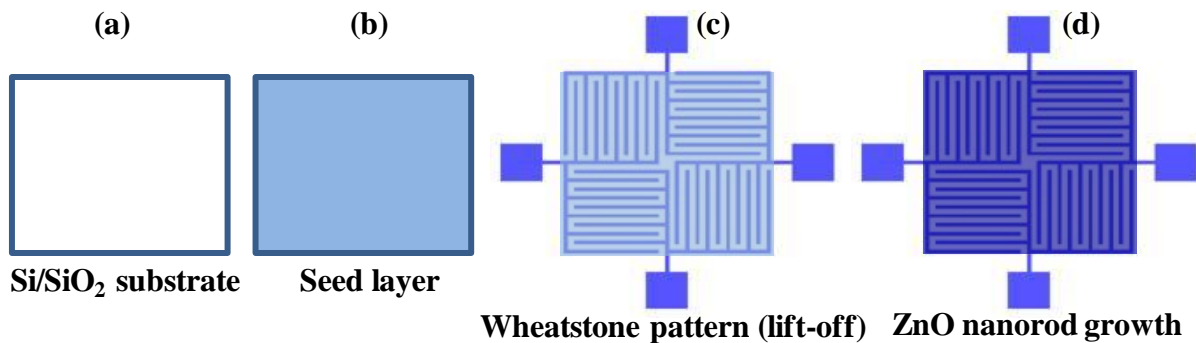
Figure 3.4   Fabrication of the simple MSM UV detector

Table 3-1   Dimensions of fabricated detector electrode pattern (66)

Pattern	Width of fingers (w) μm	Spacing between fingers (s) μm	Side length of pattern (b) μm	Active Area (cm^2)
L1	200	280	9800	5.72×10^{-1}
L2	40	45	760	3.10×10^{-3}
L3	50	45	1950	1.86×10^{-2}
L4	100	90	3900	7.44×10^{-2}
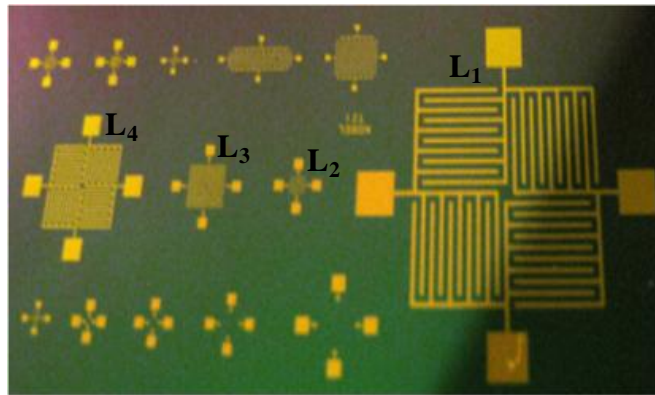
Figure 3.5   Fabricated electrode resembling Wheatstone bridge pattern on Si/SiO$_2$ wafer (66)

dimensions by varying its growth time. Rods were grown for growth time of 4 hours, 8 hours, and 16 hours. The dimensions of the rods for different growth time are shown in Table 3-2. SEM images of rods grown for different aging times are shown in Figures 3-6, 3-7, and 3-8. The length and diameter of the rods increased with increasing growth time.

When the seed layer with the fabricated electrode was immersed in nanorod growth solution, rod growth took place only on the exposed seed layer between the interdigitated electrodes. ZnO

rods did not grow on the surface of gold interdigitated electrode. The reason for lack of rod growth on the gold surface can be explained as follows. The ZnO from the nanorod growth solution can crystallize homogeneously in the growth solution or it can crystallize out heterogeneously on a substrate. But if the interfacial energy between crystal and solution is high compared to that of the crystal and substrate, ZnO from the solution prefers to crystallize heterogeneously onto a substrate. Now, comparing the interfacial energy between seed layer and ZnO from the solution and that between gold and ZnO from the solution, interfacial energy is

Table 3-2   Dimension of ZnO nanorods grown for different aging time

Aging time (Hours)	Length of the rod (µm)	Diameter of the rod (nm)	Density of the rod (cm^2)
4	0.54-0.58	20.0-30.0	9.5 x 10^{09}
8	0.60-0.70	30.0-40.0	> 9.5 x 10^{09}
16	1.15-1.75	45.0-60.0	> 9.5 x 10^{09}
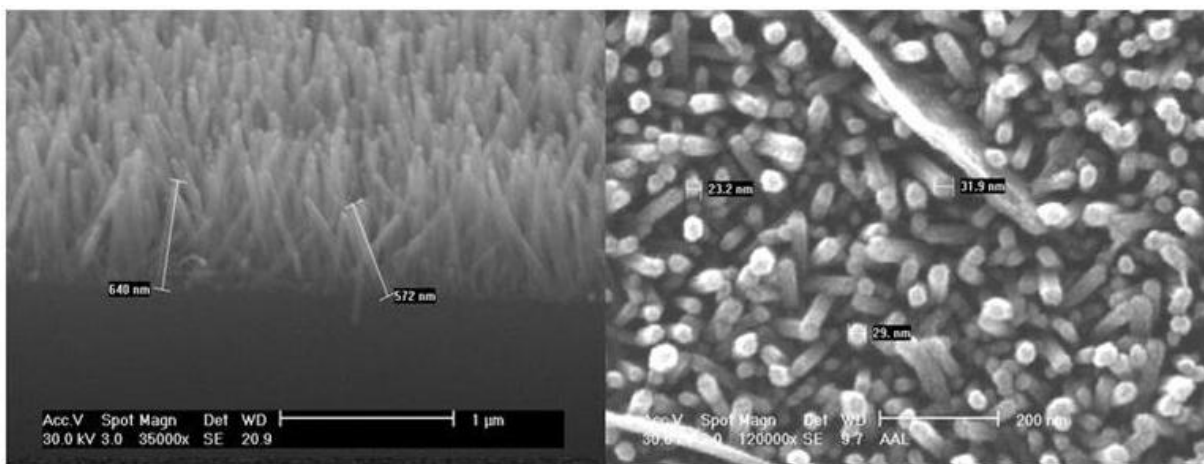
Figure 3-6   SEM images of the sample aged for 4 hours (66).
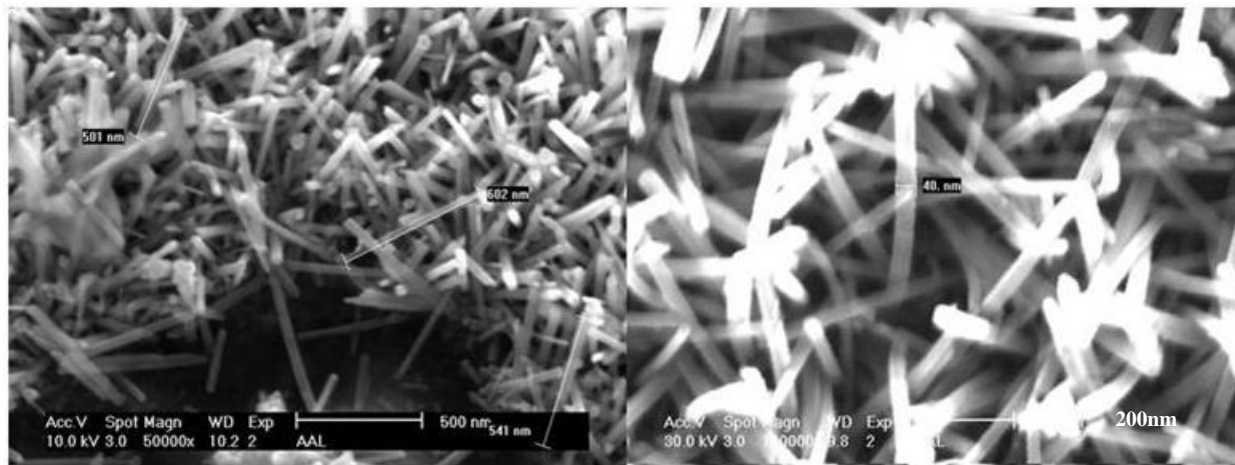
Figure 3-7   SEM images of the sample aged for 8 hours (66).
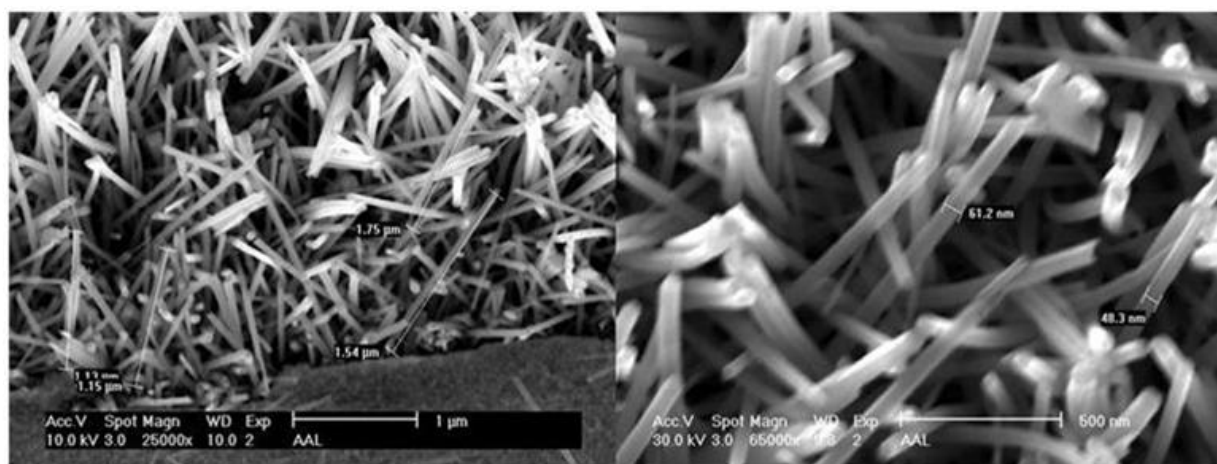
Figure 3-8   SEM images of the sample aged for 16 hours (66).

less for the seed layer and ZnO from the solution. Hence, rod growth on a seed layer is favored over a gold surface. Rod growth on a seed layer and no growth on gold surface can be seen in SEM image Figure 3-9 **(66)**. The dark colored surface in the image is the gold electrode and the brighter surfaces are rods grown on the seed layer. The magnified view of the rod is shown to the right side of the image.

41
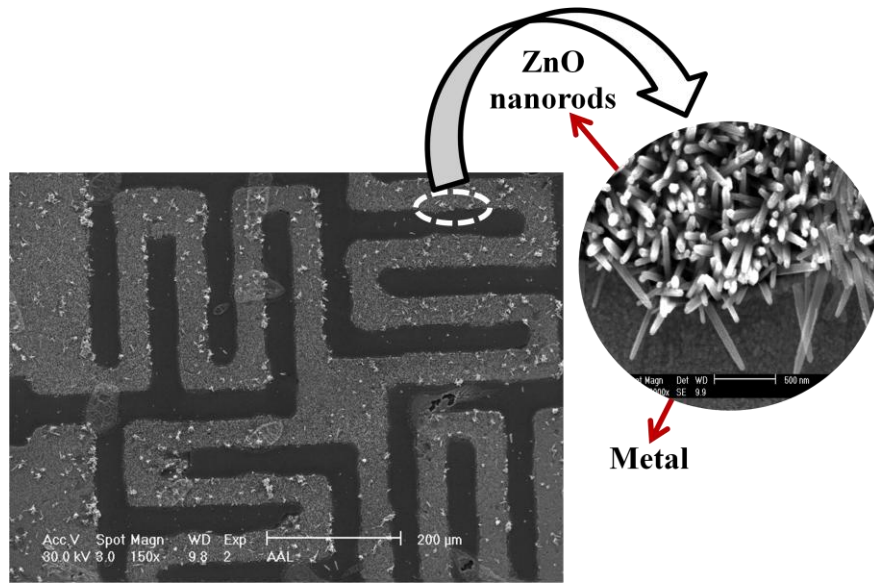
Figure 3-9   SEM image of UV detector with ZnO NRs selectively grown on the spacing between the electrodes (66).

3.2   CHARACTERIZATION OF SIMPLE MSM UV DETECTOR

3.2.1   I-V Response of Simple MSM UV Detector

Detectors fabricated for different electrode dimensions (L_1, L_2, L_3 and L_4) and for different rod length (0.54-0.58 µm, 0.60-0.70 µm, and 1.15-1.75 µm) were I-V characterized with and without illumination of 1 mW/cm^2 UV light by varying the bias from 0 to 10 V. For I-V characterization, each detector was biased as shown in Figure 3-10. The current densities of the detector for
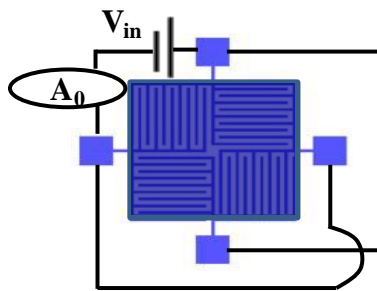
Figure 3-10   Connection diagram for I-V characterization of the simple MSM UV detector (66).

42

patterns L_1, L_2, L_3, and L_4 without rod and with rods of length 0.54-0.58 μm, 0.60-0.70 μm, and 1.15-1.75 μm without UV illumination are shown in Figure 3-11. Figure 3-11(a) is the dark current density of detector without rod growth on the seed layer. The dark current densities of detectors with rods of length 0.54-0.58 μm, 0.60-0.70 μm, and 1.15-1.75 μm are shown in Figure 3-11(b), Figure 3-11(c), and Figure 3-11(d). The dark current density for the detector without rods was of the order of 10^{-6} A/cm^2.
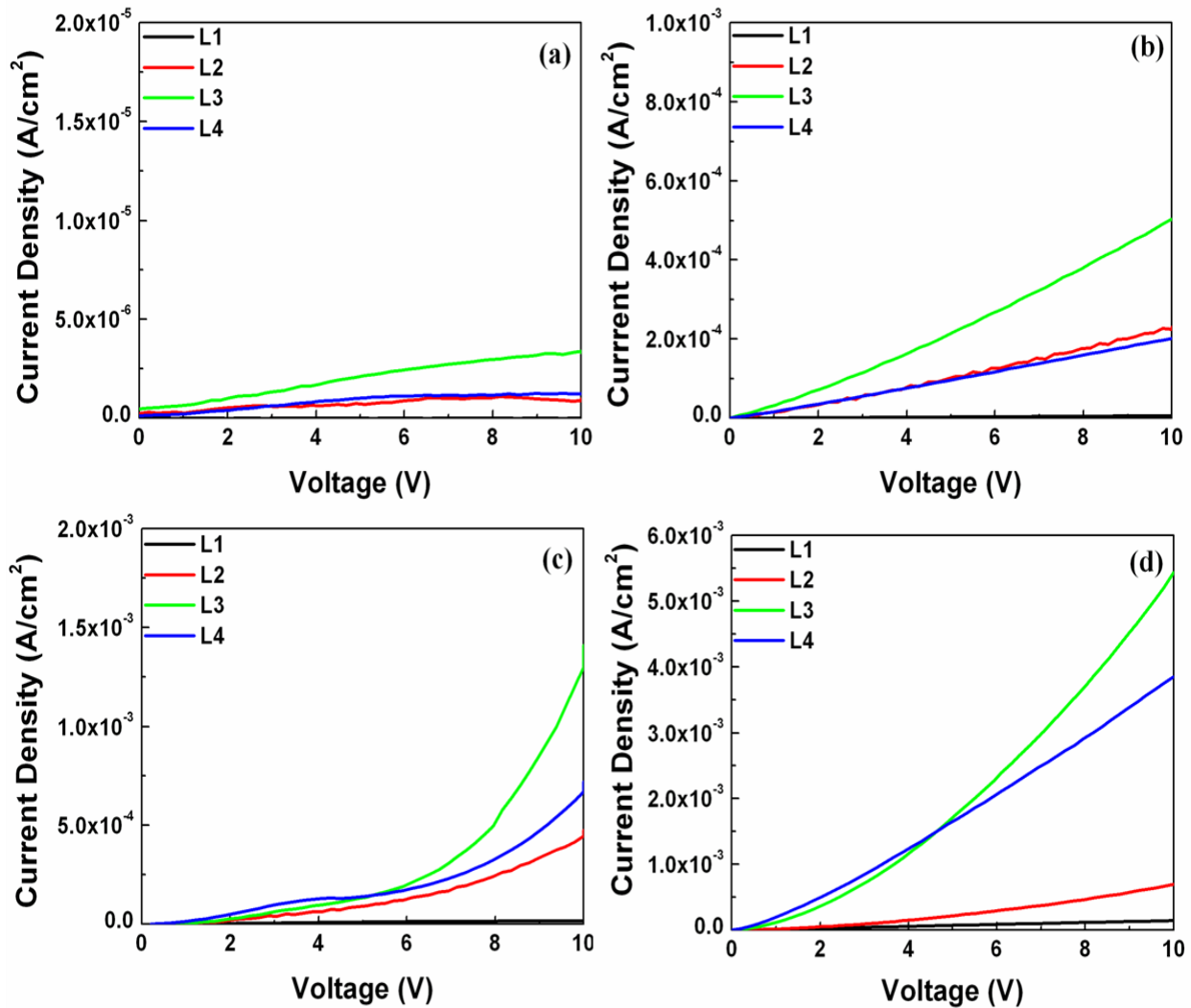
Figure 3-11 I-V characteristics of detector in absence of UV light (a) seed layer, and NRs of length (b) 0.54-0.58 μm (c) 0.60-0.70 μm (d) 1.15-1.75 μm (66).

For detectors with rods of length 0.54-0.58 µm, 0.60-0.70 µm, and 1.15-1.75 µm, dark current densities are of the order 10^{-4} A/cm^2, 10^{-4} A/cm^2, and 10^{-3} A/cm^2, respectively. The dark current densities of all four patterns L$_1$, L$_2$, L$_3$, andL$_4$, irrespective of the rod dimensions, increased with increasing bias voltage.

The increase in dark current with increasing bias voltage was explained by the Schottky diode equation for the metal-semiconductor-metal structure **(90)**. The Metal-Semiconductor-Metal structure (MSM) acts as two Schottky diodes connected back to back. When the MSM is biased, one Schottky diode is forward biased and the other Schottky diode is reverse biased. The current through the MSM is given by

$$I = AA^*T^2 \exp\left(-\frac{q\text{\O}_n}{KT}\right) \exp\left(\frac{q\Delta\text{\O}_n}{KT}\right)\left(1 - \exp\left(-\frac{q(V - IR)}{nKT}\right)\right) \qquad \text{Eq (3 – 1)}$$

where A is the area of the interdigitated fingers, A* is the Richardson constant, T is the absolute temperature, K Boltzmann constant, $\text{\O}_n$ is the barrier height, $\Delta\text{\O}_n$ is the Schottky barrier lowering, V is the potential drop across the reverse bias Schottky junction, n is the ideality factor, and R is the series resistance.

The decrease in barrier height $\Delta\text{\O}_n$ is given by,

$$\Delta\text{\O}_n = \left[\frac{2q^3NV}{16\pi^2\varepsilon_s{}^3}\right]^{1/4} \qquad \text{Eq (3 – 2)}$$

where N is the electron carrier concentration, ε_s is the permittivity of ZnO seed layer, and V is the potential drop across the reverse bias Schottky junction.

On increasing the applied bias, the barrier height decreased and so the number of carriers crossing the junction increased. Hence, the dark current density increased with increasing bias voltage. Comparing the same pattern for different rod dimensions, the dark current density increased with increase in nanorod length. A comparison of pattern L_3 for different rod length is shown in Figure 3-12. The current density was lowest for the seed layer and the dark current was highest for the detector with nanorods of length 1.15-1.75 μm.

Rod growth on the seed layer increased dark current density because previous studies had shown that the barrier height for a seed layer decreased with rod growth **(90)**. Decrease in barrier height with rod growth was due to the increase in carrier concentration of the seed layer. An increase in carrier concentration of the seed layer with rod growth was due to higher bulk defects in the nanorods **(91).**

Though dark current density for a detector with rods of length 0.60-0.70 μm was expected to
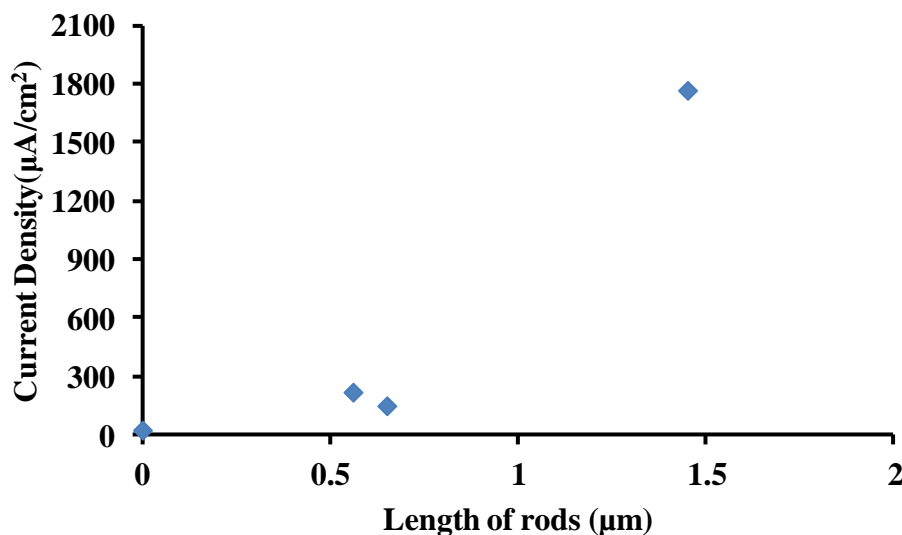
Figure 3-12   Comparison of dark current density of pattern L_3 for different rod length

be higher than for detectors with rods of length 0.54-0.58 μm, the dark current density for detectors with rods of length 0.60-0.70 μm was lesser by 7 x 10^{-5} A/cm^2. This was due to the increase in rod diameter from 20.0-30.0 nm to 30.0-40.0 nm when rods length increases to 0.60-0.70 μm. When the rod diameter increased the surface area increased, this increased the absorption of oxygen on the surface, thereby, decreasing the carrier concentration of the rod. Hence, the barrier height increases.

Comparing patterns L_1, L_2, L_3, and L_4 for the same rod length 1.15-1.75 μm, the dark current of pattern L_3 was higher than the other patterns. Comparison of dark current density of patterns L_1, L_2, L_3, and L_4 for detectors with rods of length 1.15-1.75 μm is shown in Figure 3-13. The current density was higher for pattern L_3 due to smaller spacing (45 μm) between interdigitated electrodes compared to other patterns. Detector dark current density was inversely proportional to electrode spacing because carrier transit time decreased with decreasing spacing between electrodes. Transit time 'T' can be written as,
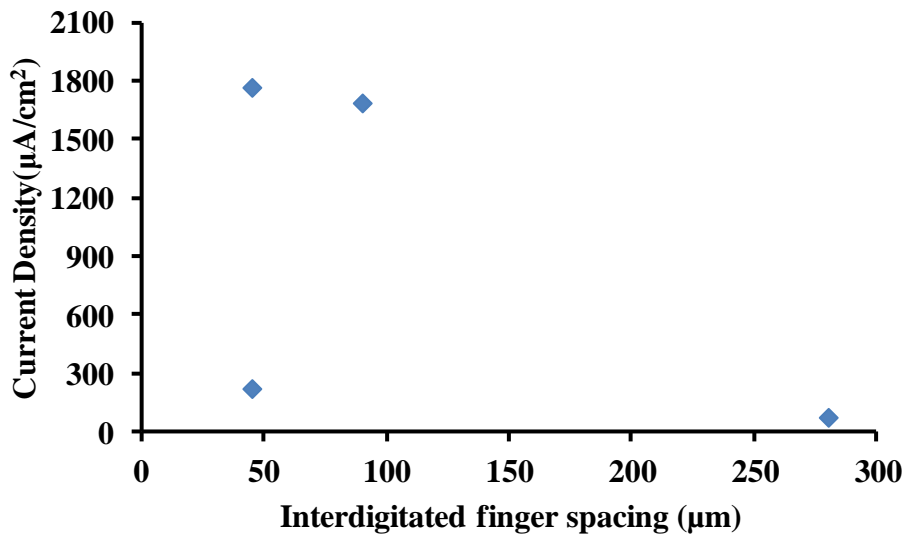
Figure 3-13   Comparison of dark current density of detector with rods of length 1.15-1.75 μm for different pattern dimension

$$T = \frac{S^2}{\mu V} \qquad\qquad\qquad\qquad\qquad \text{Eq } (3-3)$$

where S is the spacing between electrodes, μ is the carrier mobility, and V is the applied

bias **(92)**.

Based on the concept that detector dark current will increase with decreasing electrode spacing,

patterns L_2 (45 μm) and L_3 (45 μm) should have had the same dark current density. But the dark

current of density of L_3 was higher than L_2. This was explained by comparing the ratio of

electrode area to active region of the detector. The ratio of electrode area to active region of the

detector for L_2 was 0.87, while for L_3 it was 1.04. Since voltage drop across the Schottky diodes

decreased when series resistance increased, the voltage drop across Schottky diodes for L_3 was

higher than L_2. Hence, dark current density of pattern L_3 was higher than L_2.

The dark density for interdigitated electrode L_4 (90 μm) was higher than L_2 (45 μm) for detectors

with rods of length 1.15-1.75 μm by 1.47 A/cm^2. But the difference in current density between

these two patterns decreased as length of the rod decreased. This was due to higher growth

density of rods in pattern L_4 than L_2 because of larger seed area available for rod growth in L_4

than L_2 **(113)**. The seed layer area in pattern L_4 was 7.44 x 10^{-2} cm^2 and for L_2 it was 3.1 x 10^{-3}

cm^2. Due to higher growth density in L_4, rods get into contact with neighboring rods, thereby

reducing series resistance and increasing the biasing of Schottky junction. Hence, dark current

density of pattern L_4 was higher than L_2 for detectors with rods of length 0.60-0.70 μm and 1.15-

1.75 μm.

Dependence of detector response on length of rods was understood by comparing response of

detectors for patterns L_1, L_2, L_3, and L_4 without rods and with rods of length 0.54-0.58 μm, 0.60-0.70 μm, and 1.15-1.75 μm to UV light of intensity 1 mW/cm^2 shown in Figure 3-14. Responsivity of detector without rods and with rods of length 0.54-0.58 μm and 0.60-0.70 μm was on the order of 10^1 A/W but for rods with length 1.15-1.75 μm it was 10^2 A/W. Responsivity of all the four patterns L_1, L_2, L_3, and L_4 to UV light, increased with increasing bias voltage. Irrespective of rod length, responsivity of pattern L_3 was higher than other patterns. Comparison of patterns L_1, L_2, L_3, and L_4 for rods of length 1.15-1.75 μm at bias of 5 V is shown in Figure 3-15. Responsivity of pattern L_3 was higher due to lower electrode spacing between the interdigitated electrodes and high ratio of electrode area to active region of 1.04.

Comparison of responsivity of detector having same pattern for different growth time is shown in Figure 3-16. Figures 3-16(a), 3-16(b), 3-16(c) and 3-16(d) compare responsivity of detectors without rod and with rods for patterns L_1, L_2, L_3, and L_4, respectively. For all patterns, responsivity of detector with rods of length 1.15-1.75 μm was higher. High responsivity of detector with rods of length 1.15-1.75 μm was due to high absorption of UV light. Absorption of UV light is higher for rods of length 1.15-1.75 μm because absorption area was higher due to bigger rod length (1.15-1.75 μm).

Comparison of responsivity of pattern L_3 with rods grown for different length and biased at 5 V is shown in Figure 3-17. This comparison shows that the responsivity of detector increased with inclusion of nanorods and it increased with increasing nanorod length. Though the responsivity of rods with length 0.60-0.70 μm was expected to be higher than rods with length 0.5-0.58 μm, responsivity of rods with length 0.54-0.58 μm was higher than that of rods with length
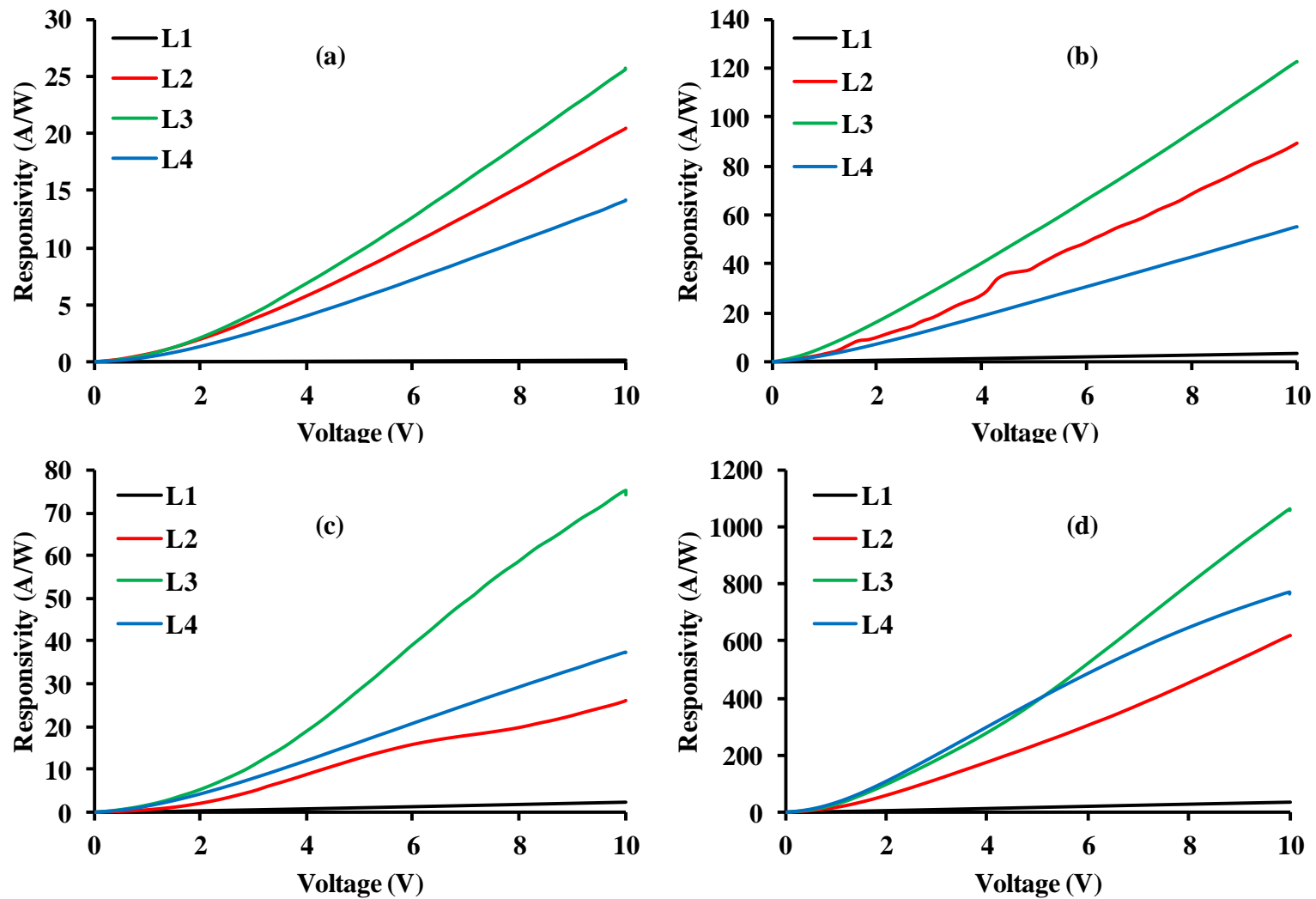
Figure 3-14 Response of detector in the presence of UV light (a) seed layer, and NRs of length (b) 0.54-0.58 μm (c) 0.60-0.70 μm (d) 1.15-1.75 μm (66).
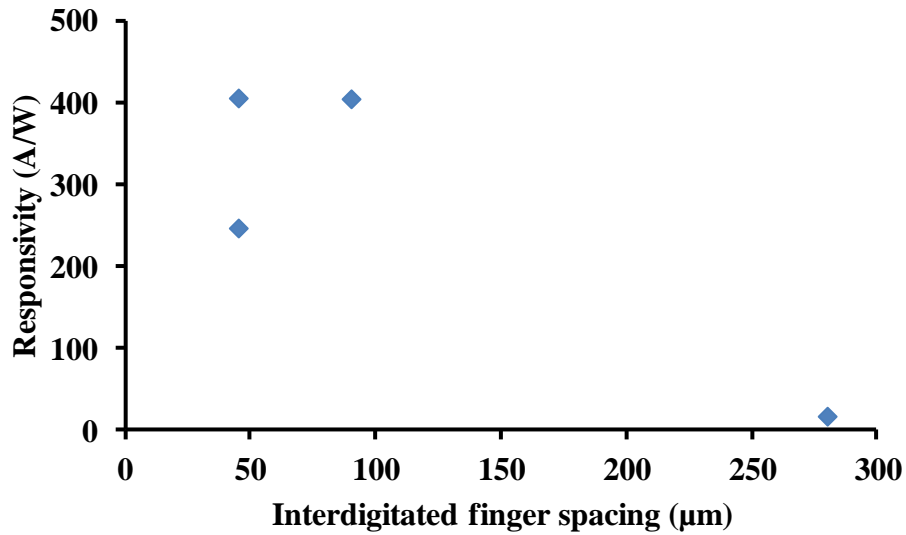
Figure 3-15   Comparison of responsivity of detector between different pattern dimensions having rods of length 1.15-1.75 μm.

0.6-0.7 μm by 25 A/W. This was explained by comparing the diameter of the rods with length 0.54-0.58 μm, 0.60-0.70 μm. The length of rods are not significantly different, but the diameter was higher for rods with length 0.60-0.70 μm.

Studies show that the responsivity of nanorod based detector decreases with increasing diameter of the rods **(65)**. Hence, responsivity was higher for detector with rods of length 0.54-0.58 μm than that of rods with length 0.60-0.70 μm.

3.2.2   Transient Response of the Detector

Comparing responsivity for different pattern, pattern L_3 had high responsivity. To determine the response time of the detector, transient responses of the detector for pattern L_3 with rods of length 0.54-0.58 μm and 1.15-1.75 μm were examined. The responses are shown in Figure 3-18. When detector was illuminated with UV light, initially for few seconds, the current increased
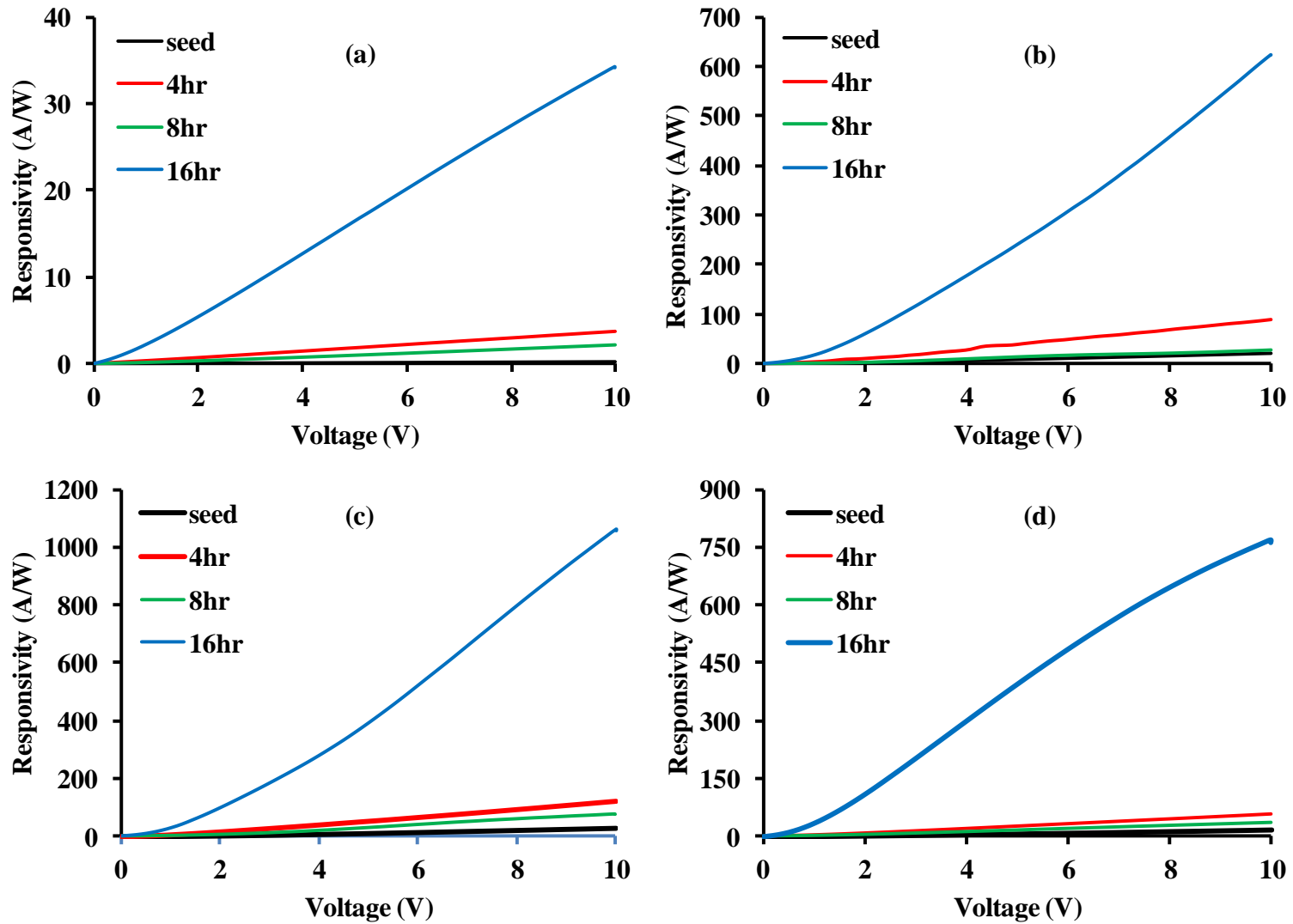
Figure 3-16   Comparison of samples with same pattern aged in growth solution for different growth periods (a) L1 (b) L2 (c) L3 and (d) L4 (66).
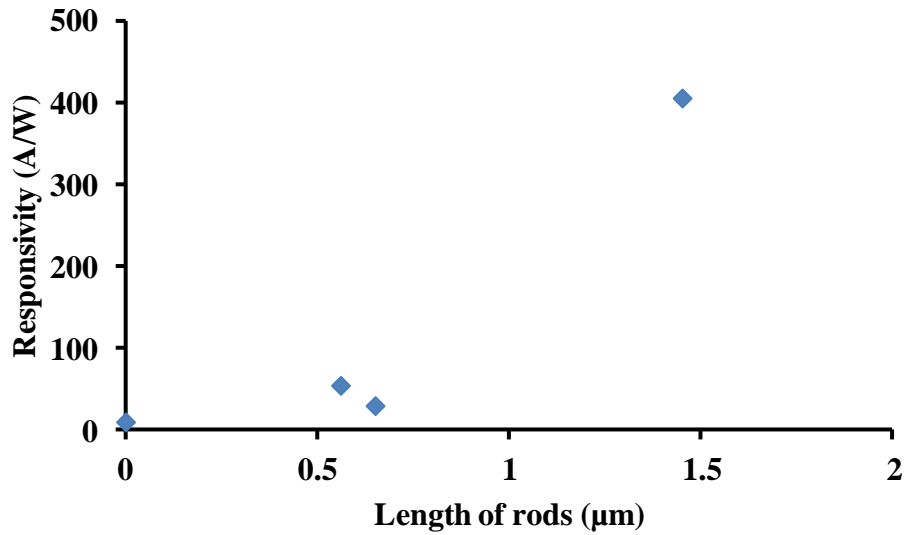
Figure 3-17   Comparison of detector responsivity of pattern L₃ with for different rod length
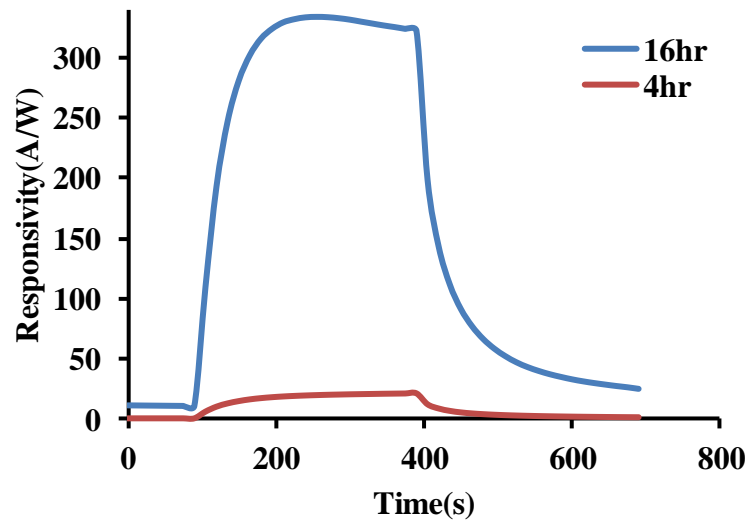
Figure 3-18   Comparison of transient response of detector with pattern L₃ and rods with length 0.54-0.58 μm and 1.15-1.75 μm (66).

rapidly due to diffusion of electrons from rods to seed layer from optically generated electron-hole pairs. Thereafter, the slow rise in current was due to diffusion of those electrons left behind

after recombination of the hole from optically generated electron-hole pair with electrons attached to the adsorbed oxygen on the rod surface. On switching off the UV light, initially, the current decreased rapidly due to electron-hole recombination. Thereafter, the slow decrease in current was due to the recombination of electrons in the rod with the holes released from surface of rods on re-absorption of oxygen. The current decay of detector, on switching of UV light, follows a second order exponential decay. The time constants for the rise process and decay process of the transient photocurrent curve were determined by fitting with exponential curve as follows:

The rise process: $I = I_0 \left(1 - \exp\left(-\frac{t}{\tau}\right)\right)$ $\qquad\qquad$ Eq $(3-4)$

The decay process: $I = I_0 \exp\left(-\frac{t}{\tau_1}\right) + I_0' \exp\left(-\frac{t}{\tau_2}\right)$ $\qquad\qquad$ Eq $(3-5)$

where I is the transient photocurrent, I_0 and $I_0{}'$ is the steady photocurrent, t is the time, and τ is the relaxation time constant **(93)**. The time constant of detector for exponential raise and exponential decay, are shown in Table 3-3. For exponential rise, the time constant of detector with rod length 1.15-1.75 µm was 32 sec and for rods with length 0.54-0.58 µm was 54 sec. Hence, detector current saturation value was quicker in detector with rods of length 1.15-1.75 µm . This

Table 3-3   Time constant of detector with rods of length 0.54-0.58 µm and 1.15-1.75 µm.

Rod length (µm)	Rise (sec)	Decay	
		Fast (sec)	Slow (sec)
0.54-0.58	54	25	111
1.15-1.75	32	27	102

might be due to larger surface area of rods with length 1.15-1.75 μm, which improves the absorption of oxygen on the surface. Time constant for faster decay due to band-to-band recombination was about the same for rods with length 0.54-0.58 μm and 1.15-1.75 μm and the average value is about 26 sec. For the slow decay part due to recombination of electrons with the holes at the surface, the decay was faster for rods with length 1.15-1.75 μm than rods of length 0.54-0.58 μm. The time constant for slow decay in detector with rods of length 1.15-1.75 μm was 102 sec and for rods with length 0.54-0.58 μm it was 111 sec. Again, the difference in time constant for rods with length 0.54-0.58 μm and 1.15-1.75 μm was due to larger surface area of rods with length 1.15-1.75 μm. Comparing the maximum responsivity of the transient response, responsivity was higher for rods with length 1.15-1.75 μm than rods with length 0.54-0.58 μm, due to higher absorption of photons. Photon absorption was higher for rods with length 1.15-1.75 μm because optical path length was higher for rods with length 1.15-1.75 μm than for rods with length 0.54-0.58 μm.

The effects of bias voltage on responsivity of detector were also examined by comparing the transient response of detector having pattern L_3 and rods with length 1.15-1.75 μm for bias voltages of 1V, 5 V, and 10 V. Transient responses for different bias voltages is shown in Figure 3-19. Maximum responsivity of detector increased with increasing bias voltage. This increase in responsivity was due to decrease in transit time and barrier lowering. Time constant of the transient response for different voltages, is shown in Table 3-4. For the rise portion of the transient curve, the time constant decreased with increasing bias voltage. This might be due to higher injection of carrriers in the seed layer because of barrier lowering with increase in bias voltage **(90)**. Comparing the decay time, the time constants for both slow and fast decays were

54

the same for different bias voltage. The average time constant for slow decay is 105 sec and

for fast decay is 25 sec.
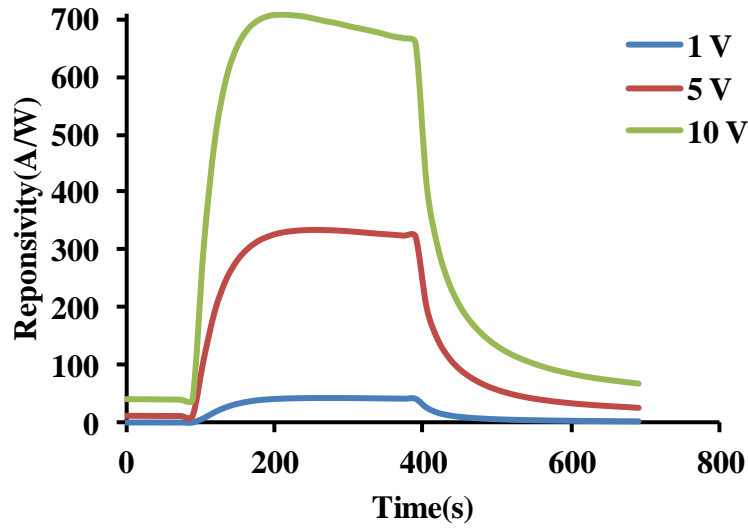
Figure 3-19   Comparison of transient response of detector with pattern L$_3$ and rods with length 1.15-1.75 μm for different bais voltages (66).

Table 3-4   Time constant of detector with pattern L$_3$ and rods with length 1.15-1.75 μm for different bias voltage

Volt (V)	Rise (sec)	Decay	
		Fast (sec)	Slow (sec)
1	39	23	109
5	32	27	102
10	23	25	105

3.3   RESPONSE DEPENDENCE ON THICKNESS OF ZINC OXIDE SEED LAYER AND CRYSTALLINITY OF ZINC OXIDE SEEDS AND RODS

The above studies for different electrode dimensions and different rod dimensions showed that that the responsivity is higher for pattern L_3 with rods of length 1.15-1.75 μm. Studies were also conducted to determine the dependence of detector response on thickness and crystallinity of the seed layer and crystallinity of the rods.

3.3.1   Response Dependence on Thickness of Zinc Oxide Seed Layer

For uniform growth of ZnO nanorods, the seed layer which acted as the nucleation sites for the ZnO nanorods needed to be uniformly deposited on the substrate. Hence, the seed layer was repeatedly spun coated in succession over the substrate. Repeated coating with seed solution increased the thickness of the seed layer, thereby decreasing the resistance of the seed layer. This increased the dark current of the detector. Detectors with high dark current will quickly drain the source powering the detector.

The thickness of the seed layer can be decreased either by decreasing the number of coating or by increasing the spin speed of coating. The drawback of decreasing the number of coatings of the seed solution was that the uniform growth of ZnO nanorods was affected. The advantage of decreasing the thickness of the seed layer by increasing the spin speed is that uniform growth is possible and studies shows that the orientation of the ZnO rods changes with higher the spin speed used for the seed layer deposition (**49, 50**).

 But despite the disadvantage of the decreasing the thickness of the ZnO seed layer by

decreasing the number of coatings, this method was tested to determine the minimum number of coatings required to obtain a low dark current and high UV response. The decrease in thickness by increasing the spin speed will also be studied since this helped in understanding the effects of orientation of the rods on the UV response of the detector. ZnO nanords were grown over the seed layer with different thicknesses under the same growth conditions. The UV response of these samples were measured and compared to determine the effects of thickness of the seed layer and orientation of the rods.

The different conditions for varying the thicknesses of the seed layer by increasing the number of repeated coatings of the seed layer is shown in the Table 3-5 and the change in thickness by varying the spin speed of coating is shown in Table 3-6. The seeds layers were spin coated at 1000 RPM. The number of repeated coatings of the seed later was varied from 2 to 5. Rods were grown on the different samples under the same growth conditions. The maximum responsivity of the samples prepared as per the conditions shown in Table 3-5 was measured by biasing the detector as shown in Figure 3-10 and powered with a 5 V supply. The maximum response attained by these samples is shown in Figure 3-20. The responsivity of the detector increased with number of repeated seed layer coatings. As per Eq (3-1), the current through the detector increased with increasing voltage drop across the Schottky junction. Since the series resistance of the detector decreased with increasing number of seed layer coatings (the dark current density of the detector for different number of seed layer coating with rods of length 1.15-1.75 µm is shown in Figure 3-21), the bias voltage drop across the Schottky junction increased. Also, the increase in response with increasing number of seed layer coatings could be attributed to the increase in density of the rod growth with increase in number of repeated seed layer coatings. The increase

in rod growth density with increase in number of times the seed layers were coated was confirmed by comparing the XRD pattern of the samples. The XRD patterns of the samples with rods grown over seed layers prepared by two repetitive coatings and five repetitive coatings are shown in Figures 3-22 and 3-23, respectively. The increase in (002) peak was an indication of

Table 3-5   Growth conditions for studying the dependence of detector response on thickness of the seed layer by varying the no of seed layer coatings

No.	Spin speed-ZnO seed layer (rpm)	No. of coating-ZnO seed layer	Growth time-ZnO rods (Hours)
1	1000	2	16
2	1000	3	16
3	1000	4	16
4	1000	5	16

Table 3-6   Growth conditions for studying the dependence of detector response on thickness of the seed layer by varying the spin speed of coating

No.	Spin speed-ZnO seed layer (rpm)	No. of coating-ZnO seed layer	Growth time- ZnO rods (Hours)
1	1000	5	16
2	2000	5	16
3	3000	5	16
4	4000	5	16
5	5000	5	16
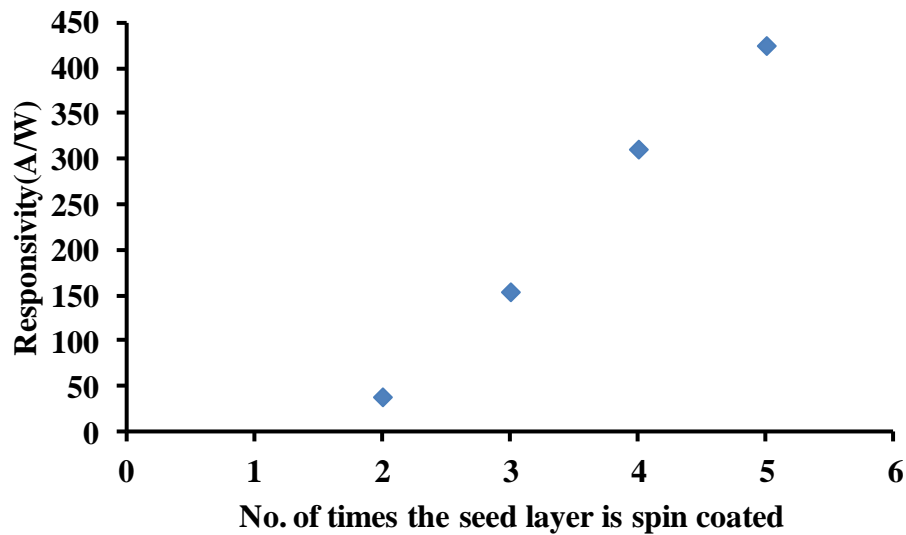
Figure 3-20 Maximum responsivity of UV detector fabricated by varying the number of repetitive coating of the seed layer.
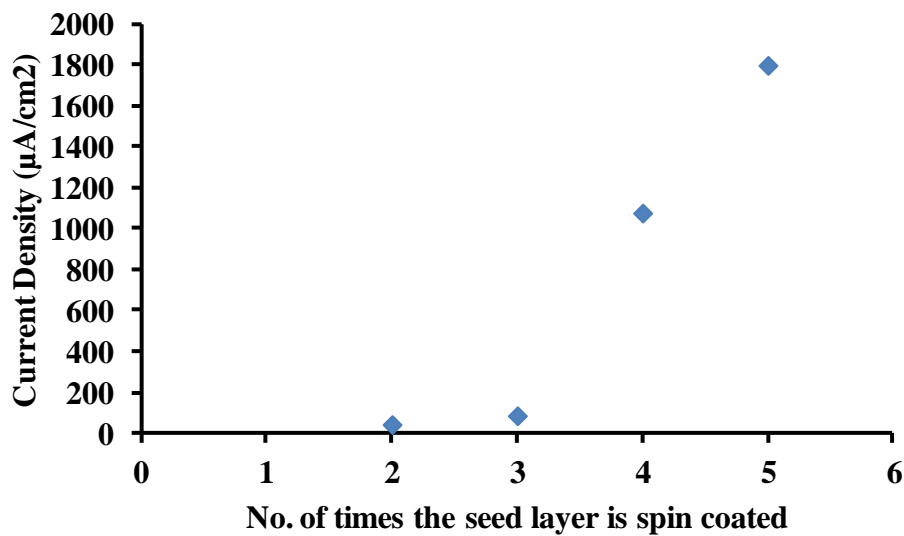
Figure 3-21 Dark current desnity of UV detector fabricated by varying the number of repetitive coating of the seed layer.

the increase in the number of (002) planes available to reflect the X-rays. Since the rods were grown over samples with different number of seed layer coating under the same growth condition, the only possibility of increase in the number of (002) planes was with increase in rod density **(114)**.
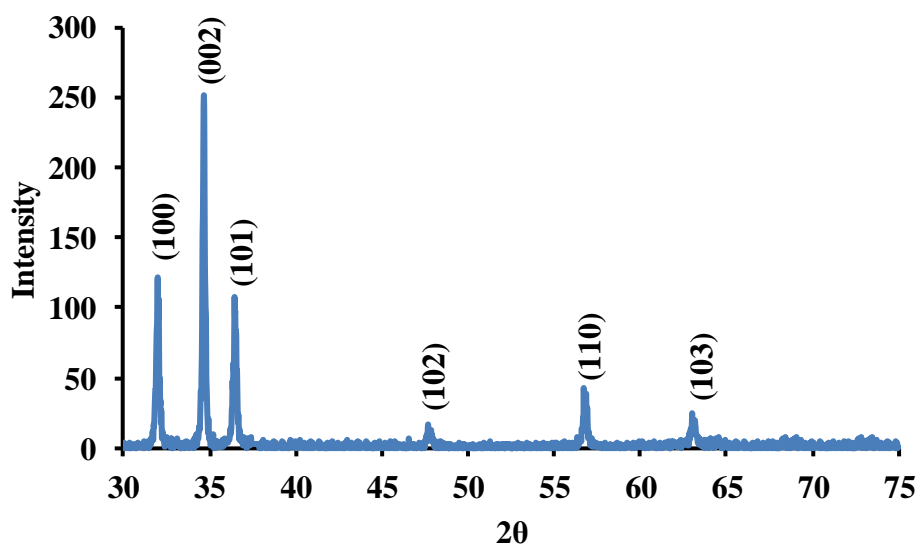
Figure 3-22   XRD pattern of ZnO nanorods grown over ZnO seed layer spin coated for two times
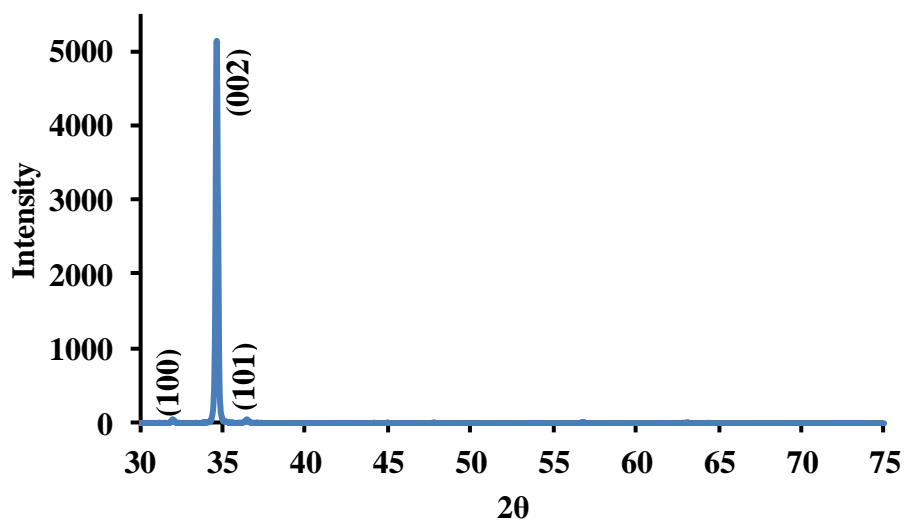
Figure 3-23   XRD pattern of ZnO nanorods grown over ZnO seed layer spin coated for five times

The conditions for which the seed layer thickness was varied by changing the spin speed of ZnO seed layer coating is shown in Table 3-6. The seed layer was repeatedly spin coated for five times with the spin speed varied from 1000-5000 RPM and the rods were grown on the samples

60

for 16 hours. The maximum responsivity of the samples for different spin speeds at which the ZnO seed layers were coated is shown in figure 3-24. Increasing the spin speed from 1000 RPM to 2000 RPM, the responsivity decreased, but for 3000 RPM and higher speeds the responsivity increased. The decrease in response at 2000 RPM could be due to the decrease in thickness of the ZnO seed layer (the dark current density of the detector is shown in Figure 3-25). The increase in response on coating at speeds 3000 RPM and above could be due to the change in orientation of the ZnO rods (106). Comparing the XRD pattern for the sample with a ZnO seed layer coated at 1000 RPM shown in Figure 3-23 and for the sample coated at 5000 RPM shown in Figure 3-26 it was observed that the intensity of the (002) planes decreased with increasing spin speed at which the ZnO seed layers were coated. The decrease in (002) planes was caused by increasing spin speed at which the ZnO seed layer were coated. The decrease in (002) planes with increasing spin speed at which the ZnO seed layer was coated might be due to majority of the rods orienting away from vertical orientation. When the rods are not oriented vertically, the (002) planes are no
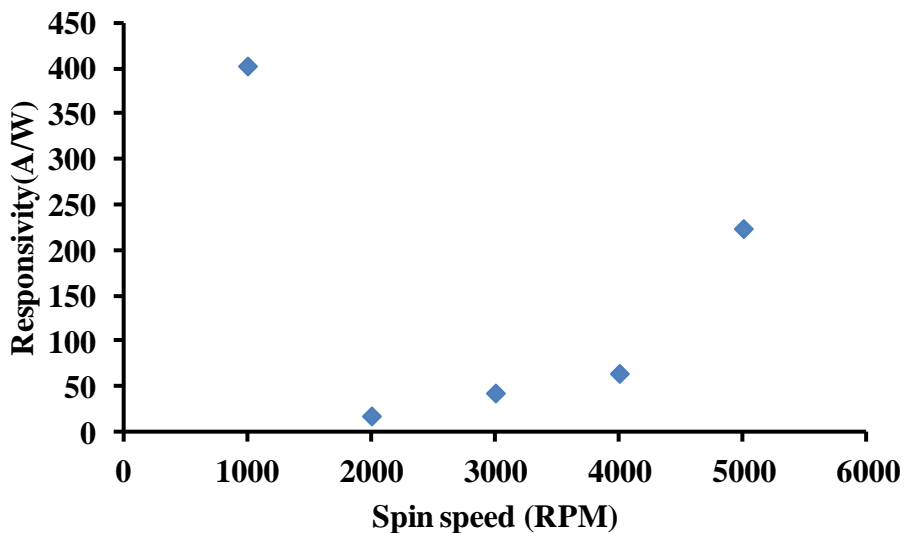
Figure 3-24 Maximum responsivity of UV detector fabricated by varying the spin speed of ZnO seed layer coating
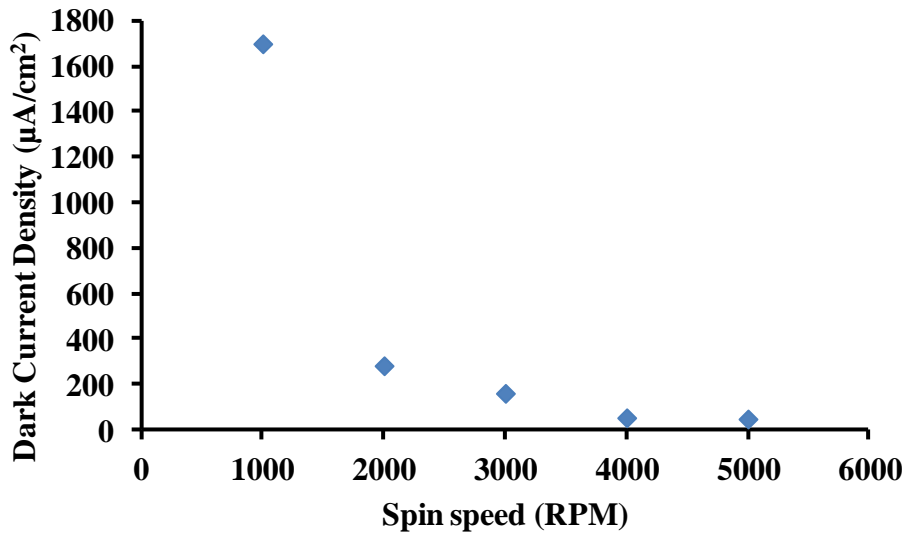
Figure 3-25 Dark current density of UV detector fabricated by varying the spin speed of ZnO seed layer coating
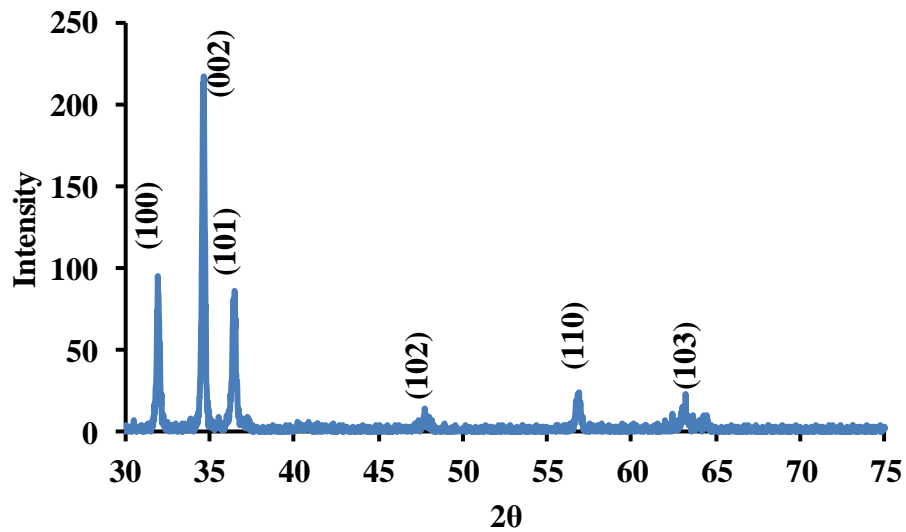
Figure 3-26 XRD pattern of ZnO nanorods grown over ZnO seed layer spin coated at 5000 RPM

longer parallel to the substrate. Hence, the intensity of (002) peaks decreases. The (002) intensity peak visible in the XRD pattern shown in Figure 3-26 is of those rods which are oriented vertically.

3.3.2 Response Dependence on Crystallinity of Zinc Oxide Seed Layer and Rods

The crystallinity of the ZnO rods grown could affect the sensitivity and the response time of the detector. Rods with good crystallinity improves photogeneration and photocarrier lifetime thereby, affecting the responsivity and response time of the detector **(107, 108)**. The crystallinity of the rods can be improved by improving the crystallinity of the seed layer or by annealing the rods **(109)**. To study the effects of crystallinity of the seed layer and the rods on the characteristics of the detector, seed layer and rods were prepared under the conditions shown in the table 3-5. The structural changes of the rods and seed layer were studied using XRD with CuK_α radiation of wavelength 1.5418 Å.

To determine the dependence of detector response on the temperature at which the seed layer is annealed, samples were prepared for growth conditions shown in Table 3-7. The maximum response of the detector samples prepared for different annealing temperature of the seed layer is shown in Figure 3-27. The responsivity of the detector increased on increasing the annealing

Table 3-7 Growth conditions for studying the dependence of detector response on annealing temperature of the seed layer

No.	Spin speed- ZnO seed layer (rpm)	Annealing- ZnO seed layer (^{0}C)	Growth time- ZnO rods (Hours)
1	1000	350	16
2	1000	450	16
3	1000	550	16
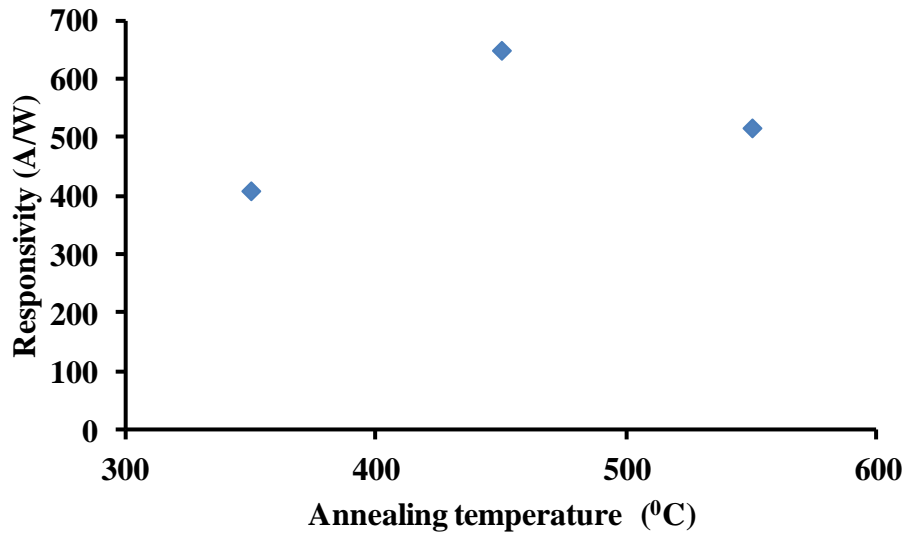
Figure 3-27 Maximum responsivity of UV detector fabricated by growing rods over ZnO seed layer annealed at different temperature

temperature from 350^0C to 450^0C, but when annealed at 550^0C the responsivity decreased. The possible reason for the increase in response when the seed layer was annealed at 450^0C was explained with XRD patterns of ZnO seed layer annealed at 350^0C, 450^0C and 550^0C shown in Figure 3-28. The XRD peak intensity for (002) planes of ZnO seed layer increased with an increase in annealing temperature. The increase in intensity of the (002) planes of seed layer with annealing was due to improvement in crystallinity. The XRD pattern of the rods grown over these annealed ZnO seed layer is shown in Figure 3-29. The increase in intensity could have been due to increases in density of the rod growth or due to the improved rod crystallinity. Studies shows that the density of rod growth decreses with increase in annealing temperature (**110**). Also, if the increase in (002) planes was due to improved rod growth density, then the responsivity of the detector should increase with increase in rod growth density. Though the responsivity increased for seed layer annealed at 450^0C, the responsivity dropped for the seed layer annealed at 550^0C. Hence, the increase in intensity of the (002) was not due to increase in

64
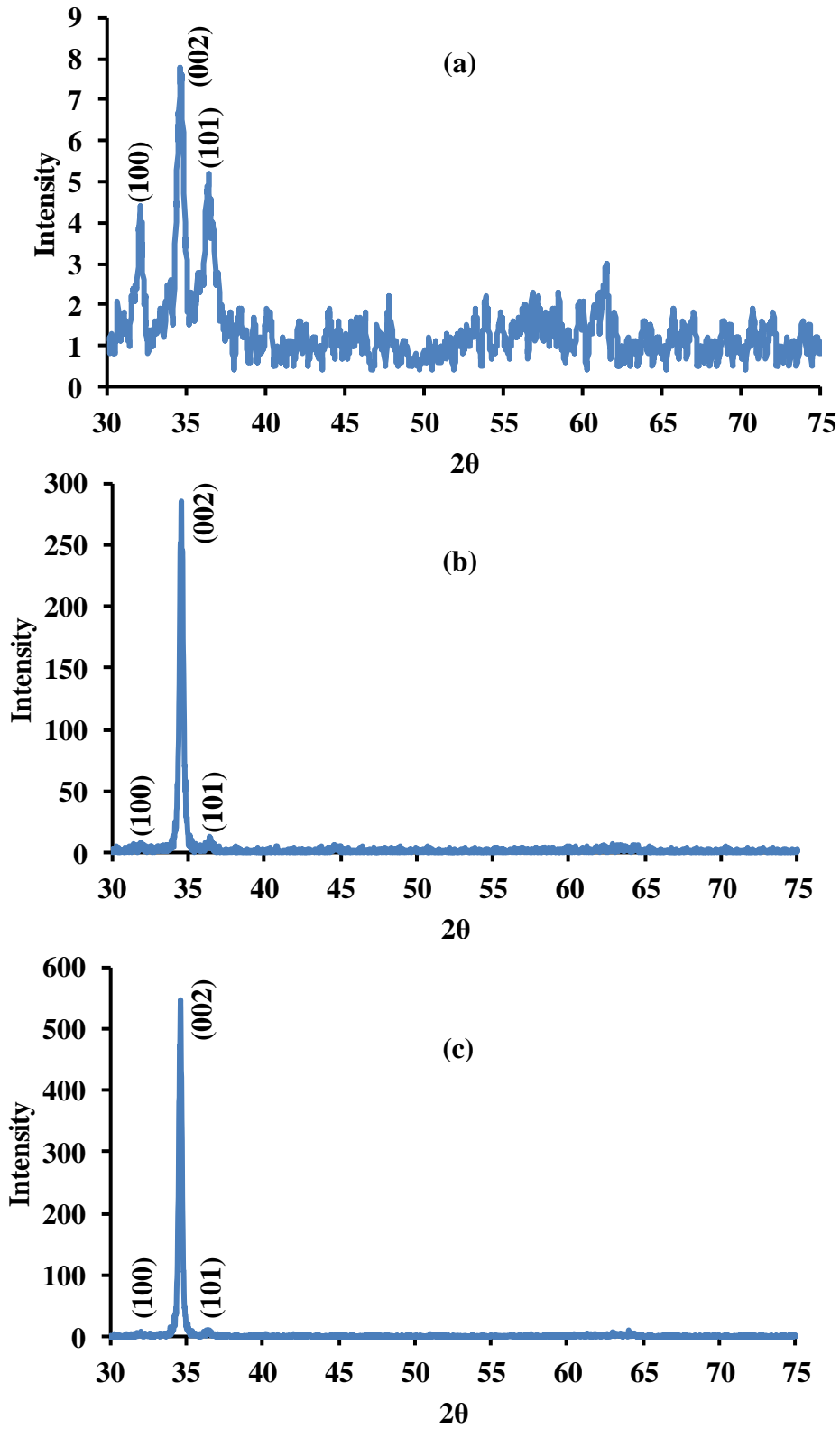
Figure 3-28   XRD pattern of ZnO seed layer annealed at different temperature (a) 350^{0}C (a) 450^{0}C (a) 550^{0}C
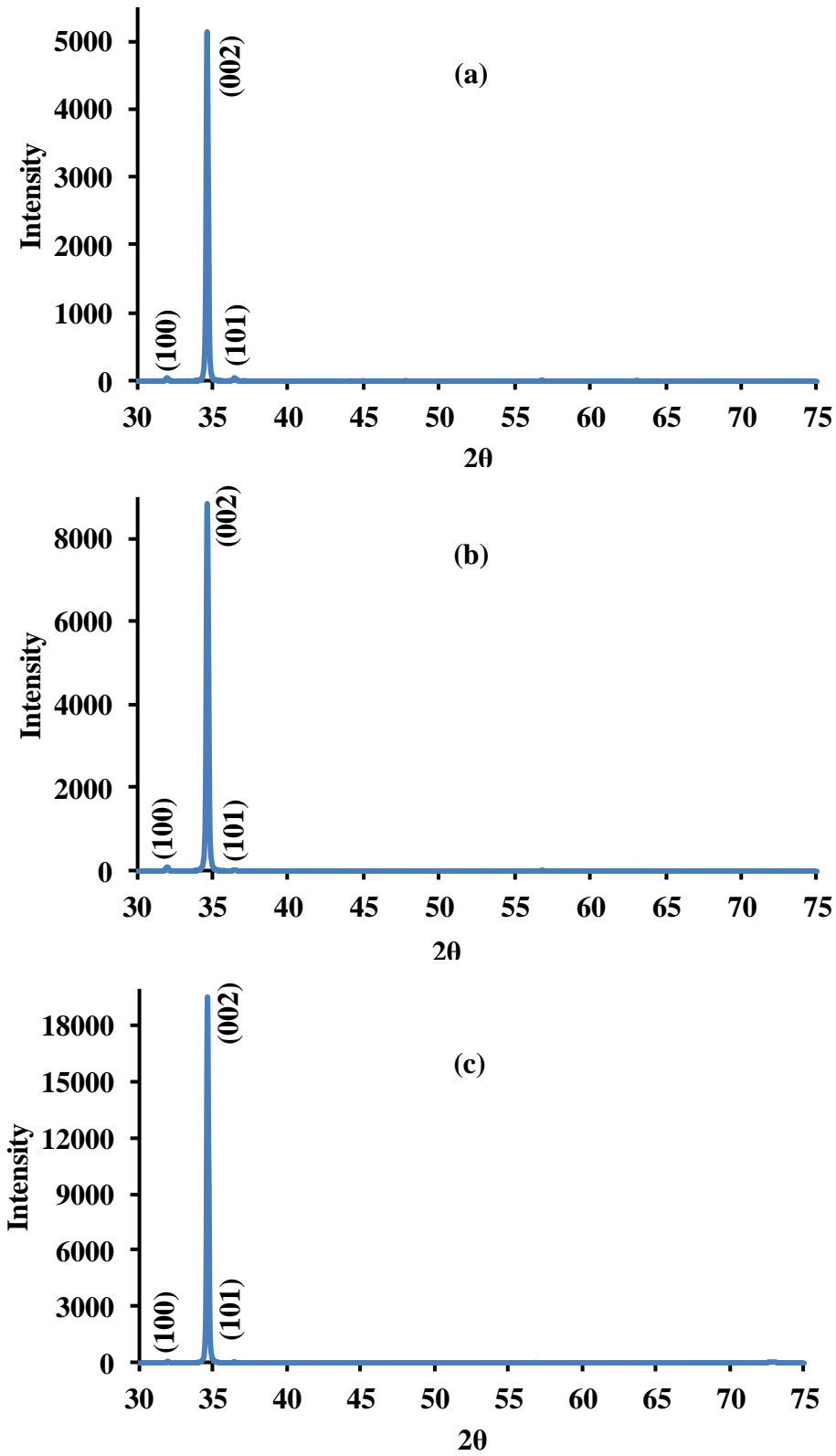
Figure 3-29   XRD pattern of ZnO rods grown over ZnO seed layer annealed at different temperature (a) 350^{0}C (a) 450^{0}C (a) 550^{0}C

rod growth density but due to improved crystallinity. The drop in responsivity at 550^0C in spite of improved crystallinity could have been due to a decrease in surface defects. A decrease in surface defects decreases the oxygen absorption on the rod surface, thereby, reducing the carrier generation due to hole-oxygen recombination (**107, 108, 111**).

The effect of annealing the rods grown over seed layer annealed at 350^0C was also studied. The rod growth conditions and the temperature at which the rods were annealed are shown in Table 3-8. The seed layer of all the four samples were spin coated at 1000 rpm and annealed at 350^0C. The rods grown on these four samples were annealed at 100^0C to 250^0C. The maximum

Table 3-8   Growth conditions for studying the dependence of detector response on annealing temperature of the seed layer

No.	Spin speed- ZnO seed layer (rpm)	Annealing- ZnO seed layer (^{0}C)	Growth time- ZnO rods (Hours)	Annealing- ZnO rods (^{0}C)
1	1000	350	16	100
2	1000	350	16	150
3	1000	350	16	200
4	1000	350	16	250

responsivity of these samples is shown in Figure 3-30. The responsivity increased with increase in annealing temperature up to 200^0C, but on annealing at 250^0C the responsivity started to decrease. This behavior is similar to that observed for the samples prepared by growing rods on samples annealed at different temperature. On annealing the rods at different temperature, the intensity of (002) planes increased. Hence, the decrease in response on annealing at 250^0C was due to decrease in surface defects (**107, 108, 111**).
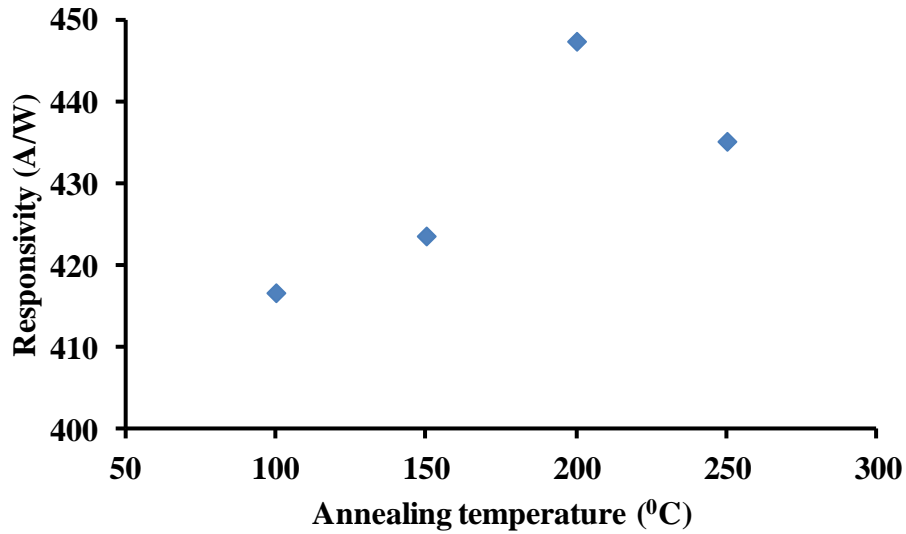
Figure 3-30 Maximum responsivity of UV detector with rods annealed at different temperature

A summary of observations drawn from the above studies about the responsivity dependence of a MSM UV detector on properties of ZnO seed layer, rods and electrodes is presented here. With regard to the seed layer, though the dark current was decreased by decreasing the thickness of the seed layer, the responsivity decreases if the seed layer thickness was below 40-50 nm. Annealing the seed layer improved the crystallinity of the rods. Hence, the responsivity of the UV detector increased. But when annealed at 550^0C the responsivity dropped. The drop in responsivity was due to a decrease in surface defects. The decrease in surface defects increased the response time of the detector. Similarly the repsonsivity increased on annealing the ZnO rods up to 200^0C, but on annealing at 250^0C the responsivity dropped due to a decrease in surface defects. With regard to the dimension of the rods, the responsivity increased with increase in length of the rods. In the case of the dimension of the electrodes, the responsivity increased with increase in width of the electrode and decrease in spacing between the electrodes.

4. WHEATSTONE BRIDGE UV DETECTOR (SYMMETRIC AND ASYMMETRIC)

The physical properties of ZnO material allow operation of ZnO based detector in harsh environments (temperature greater than 333 K and radiation of energy greater than 124 eV), still responsivity of ZnO based detectors can be affected when operated at temperatures greater than 333 K. The reason for change in detector response when operated at temperatures greater than 333 K can be understood by examining the actual mechanism involved for the high response of the ZnO based material. Responsivity of ZnO based detectors is high (> 1 A/W) compared to other materials due to high excitonic binding energy (60 meV) and separation of the optically generated electron-hole pairs by the depletion region formed due to oxygen adsorption at the surface of the nanorods **(64, 65)**. Hence, responsivity of ZnO rods to UV light can be affected by both ambient temperature and atmospheric pressure **(86-88)**. The effects of these ambient conditions on the responsivity of a ZnO based detector can be isolated if output of the detector depends on a ratio of inputs. Such a ratiometric configuration is possible if a detector is fabricated to operate using the Wheatstone bridge principle.

4.1 SYMMETRIC WHEATSTONE BRIDGE UV DETECTOR

4.1.1 Structure of Symmetric Wheatstone Bridge UV Detector

The schematic diagram of the ZnO nanorod based UV detector with a Wheatstone bridge design is shown in Figure 4-1(a). Figure 4-1(b) depicts different layers of the detector structure. The detector structure shown in Figure 4-1(a) is a symmetric Wheatstone bridge, i.e., all four arms or quadrants of the bridge are identical. As shown in Figure 4-1(b), each quadrant consist of a ZnO

69
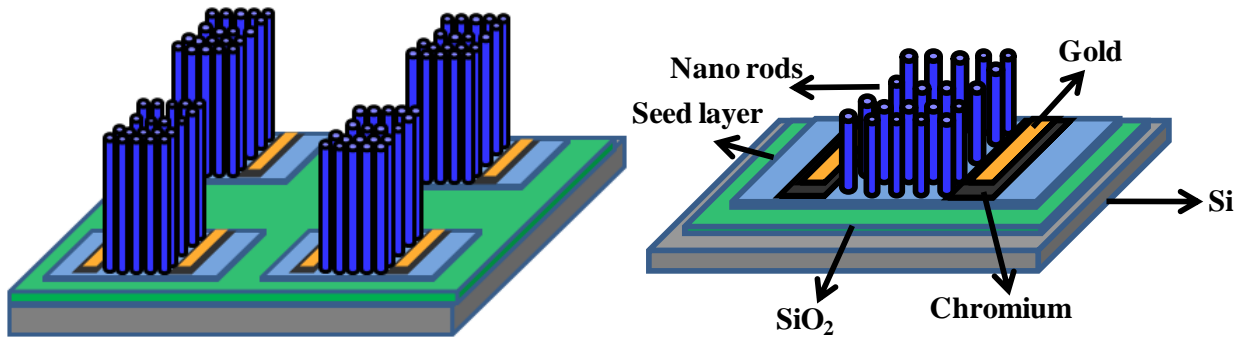
Figure 4-1   Wheatstone bridge UV detector (a) Structure of the detector (b) Cross-sectional view of the detector quadrant.

seed layer, an electrode made of chromium and gold layer, and ZnO nanorods. The detectors are fabricated on a Si/SiO_2 wafer to isolate the detector from the Si substrate and to prevent the Si substrate from shorting the four quadrants. The four quadrants are connected to each other by means of an interdigitated electrode. If a detector is fabricated to operate in Wheatstone bridge mode, then its input voltage (V_{in}) is related to output voltage by the relation,

$$V_o = \left[\left(\frac{R_3}{R_2 + R_3}\right) - \left(\frac{R_4}{R_1 + R_4}\right)\right] V_{in}$$

Eq $(4-1)$

where R_1, R_2, R_3, and R_4 are the resistance of the four arms of a Wheatstone bridge and biased as shown in Figure 4-2.
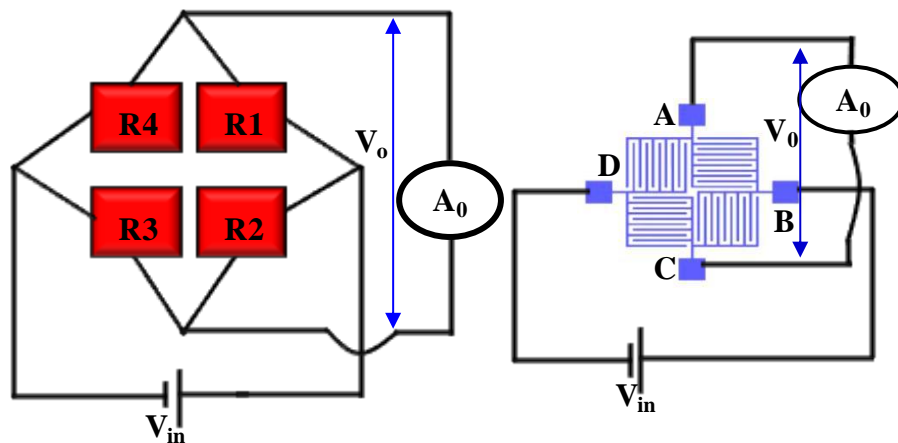
Figure 4-2   Schematic diagram of the Wheatstone bridge circuit (a) Wheatstone bridge (b) connection diagram for Wheatstone bridge operation of the UV detector.

70

4.1.2   Fabrication of Symmetric Wheatstone Bridge UV Detector

A schematic representation of the fabrication procedure for a symmetric Wheatstone bridge detector is shown in Figure 4-3. The ZnO seed layer was coated on Si/SiO_2 wafer by spin coating seed layer solution prepared by dissolving 0.1 M zinc acetate and 0.1 M ethanolamine in ethanol

(a)	(b)	(c)
Si/SiO$_2$ substrate	Seed layer	Etching

(d)	(e)
Wheatstone pattern on seed layer	Nanorod growth
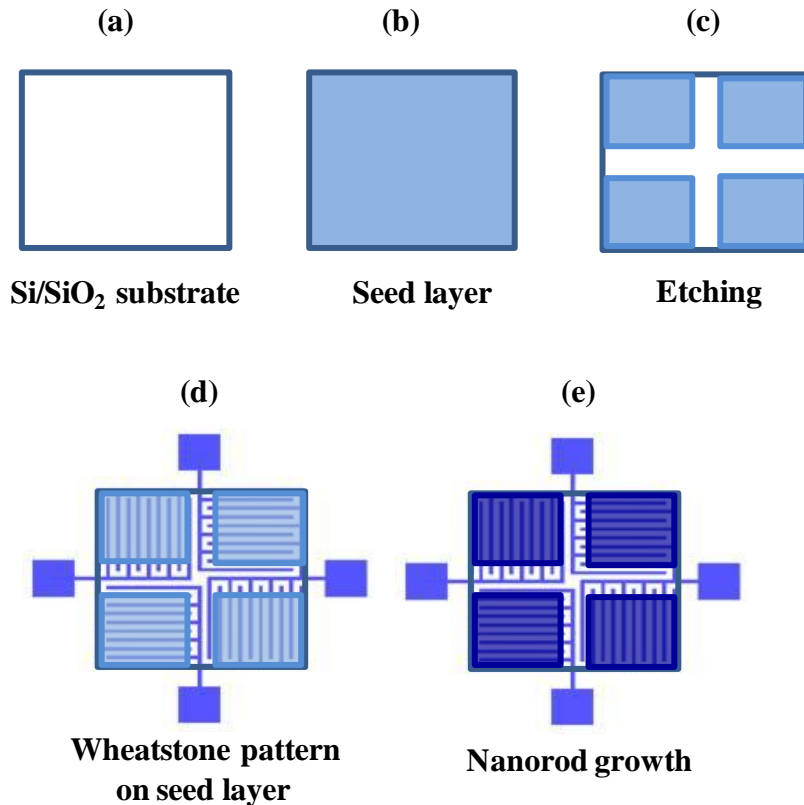
Figure 4-3   Schematic representation for fabrication of ZnO nanorod based symmetric Wheatstone bridge detector.

solution by stirring for 1 hour at 75^0C, thereafter, storing for one day **(82)**. The ZnO seed layer solution was repeatedly spin coated in succession for five times for uniform coverage of the seeds. Prior to each coating of seed layer the wafer was annealed at 170^0C to remove solvents from the film. The seed film was then annealed at 350^0C for 2 hours. On annealing, zinc acetate seeds were converted to ZnO seeds due to reaction with atmospheric oxygen. The ZnO seed

layer was then etched into four equal sized quadrants using diluted HCl (1:1000). Then, a Wheatstone bridge shaped electrode was patterned over the four quadrants of ZnO seed layer using photolithography and lift-off techniques. The electrode consisted of successive layers of 5 nm chromium and 100 nm of gold deposited using thermal evaporation at a deposition rate of 0.4 nm per sec. After fabrication of the electrode (pattern L_1) on seed layer, the sample was immersed in nanorod growth solution prepared from 0.035 M of hexamethylenetetramine and 0.025 M of zinc nitrate and aged in an oven at 90 ^{0} C for 16 hours (82).

4.1.3 Theoretical Output Voltage of Symmetrical Wheatstone Bridge UV Detector

Response of the symmetric Wheatstone bridge detector to UV light was measured by either exposing all four quadrants or three or two or one quadrant of the detector. To determine which exposure mode gave maximum output voltage, the theoretical output voltage of a detector with pattern L_1 and rods grown for length 1.15-1.75 µm was calculated using Eq. (4-1) for different exposure modes. For calculating theoretical output voltage of the detector using eq. (4-1), the resistance of the four quadrants of the detector with pattern L_1 and rods grown for length 1.15-1.75 µm, was measured. The resistance of the four quadrants without UV light and with UV light is shown in Table 4-1.

The output voltages calculated using Eq.(4-1), corresponding to an input voltage V_{in}= 5 V, for pattern L_1 and rods grown for length 1.15-1.75 µm is shown in Table 4-2. Output voltage of the detector was maximum for the exposure mode exposing the diagonal quadrants R_1 and R_3 or R_2 and R_4. The output voltage on exposing R_1 and R_3 is -4.9 V and for R_2 and R_4 it was 4.88 V. Thenegative sign for the output voltage when quadrants R_1 and R_3 are exposed means that the

72

Table 4-1   Resistance of the four quadrants of symmetric Wheatstone bridge UV detector

	Resistance without Illumination [Ω]	Resistance with Illumination [Ω]
R1	R1D=1.68 X 10^{06}	R1L=1.61 X 10^{04}
R2	R2D=1.31 X 10^{06}	R2L=1.47 X 10^{04}
R3	R3D=1.14 X 10^{06}	R3L=1.46 X 10^{04}
R4	R4D=1.68 X 10^{06}	R4L=1.56 X 10^{04}

Table 4-2   Output voltage of symmetric Wheatstone bridge for different exposure modes

Exposure mode	Voltage [V]
R1D, R2D, R3D, R4D	-0.12
Single quadrant exposed	
R1D, R2D, R3D, **R4L**	2.74
R1D, R2D, **R3L**, R4D	-2.15
R1D, **R2L**, R3D, R4D	2
R1L, R2D, R3D, R4D	-2.92
Two quadrant exposed	
R1L, **R2L**, R3D, R4D	-0.37
R1D, **R2L**, **R3L**, R4D	-0.0003
R1D, R2D, **R3L**, **R4L**	0.23
R1L, R2D, R3D, **R4L**	-0.0068
R1L, R2D, **R3L**, R4D	-4.9
R1D, **R2L**, R3D, **R4L**	4.88
Three quadrant exposed	
R1L, **R2L**, **R3L**, R4D	-2.34
R1L, **R2L**, R3D, **R4L**	2.54
R1L, R2D, **R3L**, **R4L**	-2.52
R1D, **R2L**, **R3L**, **R4L**	2.37
Four quadrant exposed	
R1L, **R2L**, **R3L**, **R4L**	0.03

output voltage direction reversed on exposing quadrants R_2 and R_4, but the magnitude was about

the same due to the symmetric nature of the bridge. As per the theoretical calculation, the

magnitude of the output voltage was maximum when only the diagonal quadrants were exposed. Hence, the transient response of symmetric Wheatstone bridge detector was measured for different temperature by exposing only the diagonal quadrants. Though pattern L_3 had the highest responsivity, pattern L_1 was used for studying the transient response of symmetric Wheatstone bridge detector. This was because, for obtaining maximum voltage, diagonal quadrants were masked. A UV masking film was used to mask the quadrants, so patterns with bigger dimension were more appropriate for the studies.

4.2 ASYMMETRIC WHEATSTONE BRIDGE UV DETECTOR

4.2.1 Structure of Asymmetric Wheatstone Bridge UV Detector

To ascertain the effects of the symmetrical nature of the Wheatstone bridge on stability of the detector, asymmetric Wheatstone bridges were fabricated. In case of symmetrical Wheatstone bridge, rods were grown on all the four quadrants. The schematic diagram for the asymmetricWheatstone bridge is shown in Figure 4-4.
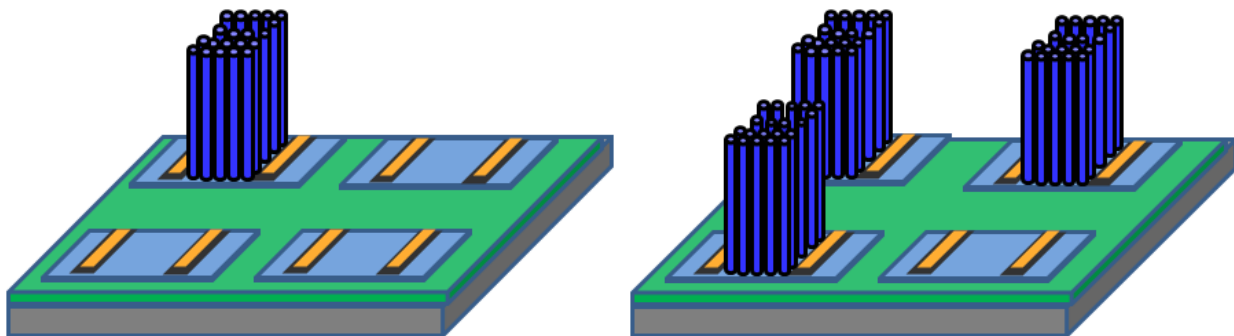
Figure 4-4   Asymmetric Wheatstone bridge (a) rod growth in one quadrant (b) rod growth in three quadrants

74

4.2.2 Fabrication of Asymmetric Wheatstone Bridge UV Detector

An asymmetric Wheatstone bridge can be fabricated by either growing rods only on one quadrant or on three quadrants. The fabrication steps for an asymmetric bridge are almost the same as that of a symmetric Wheatstone bridge. For an asymmetric bridge detector, rod growth should be prevented on specific quadrants. This was achieved by masking respective quadrants where rod growth should be prevented with photoresist. Rods were grown on the unmasked quadrants by immersing the detector sample in the rod growth solution and heating it in an oven for 16 hours. After rod growth, the photoresist masking was stripped off. A schematic representation of the fabrication procedure of an asymmetric Wheatstone bridge with rods grown only on one quadrant is shown in Figure 4-5. SEM images of an asymmetric Wheatstone bridge with rod growth only in one quadrant of pattern L_2 (rods grown for 16 hours) are shown in
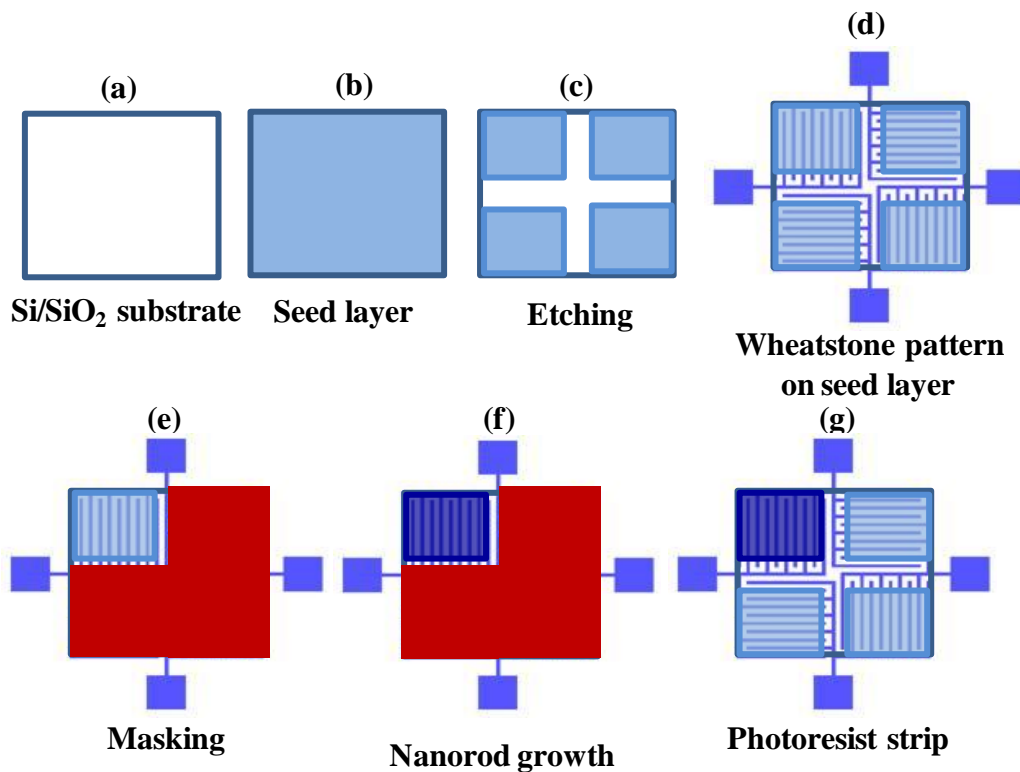
Figure 4-5   Schematic representation for fabrication of ZnO nanorod based asymmetric Wheatstone bridge detector.

Figure 4-6. For fabrication of an asymmetric Wheatstone bridge with rod growth on three quadrants, only one quadrant was masked before immersing the structure in rod growth solution. Microscope images of symmetric and asymmetric detectors with pattern L_2 and rods grown for 16 hours are shown in Figure 4-7.

(a) (b)

(c) (d)
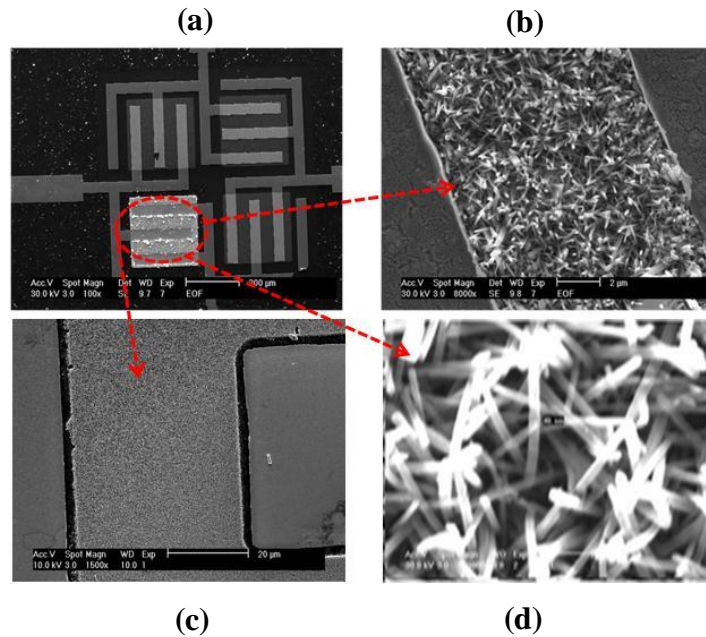
Figure 4-6   SEM images of asymmetric Wheatstone bridge detector (a) UV detector having dimension b= 760 µm, w=40 µm, s=45 µm with rod growth only in one quadrant (b),(c) and (d) Magnified images of the rods in between the interdigitated electrode

(a) (b) (c) (d)

w/s=200/280 µm

Nanorods   Nanorods are absent

b=760 µm
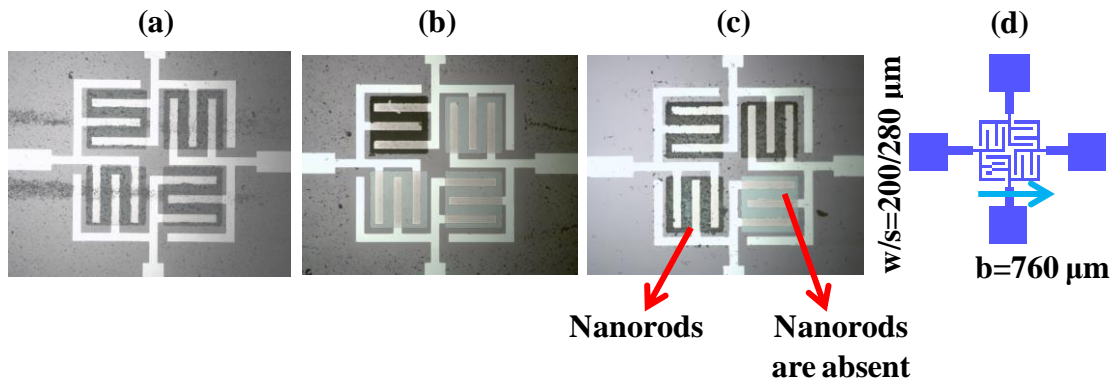
Figure 4-7   Microscope image of symmetric and asymmetric Wheatstone bridge detector (a) Detector with rods in all four quadrants (b) Detector with rods in one quadrant (c)Detector with rods in three quadrants (d) Dimensions of the electrode pattern.

4.3   TRANSIENT RESPONSE OF WHEATSTONE BRIDGE UV DETECTOR

The transient response of the UV detector was measured by biasing the detector as shown in Figure 4-1(b). The response of detector was measured for UV light of wavelength 365 nm with an intensity of 1 mW/cm^2 and the detector biased at 5 V.

4.3.1   Transient Response of Symmetric Wheatstone Bridge UV Detector

The transient response of a symmetric Wheatstone bridge detector for pattern L_1 with rods grown for 16 hours is shown in Figure 4-8. Irrespective of the ambient temperature, when the detector was exposed to UV light the current initially rose fast (linear region) at the rate of few seconds, thereafter, it rose slowly at the rate of 299 sec. Initially, current rose fast due to diffusion of electrons from photogenerated electron-hole pairs. The following slow rise in current was due to diffusion of electrons, separated from the excitons due to recombination of holes, to the oxygen
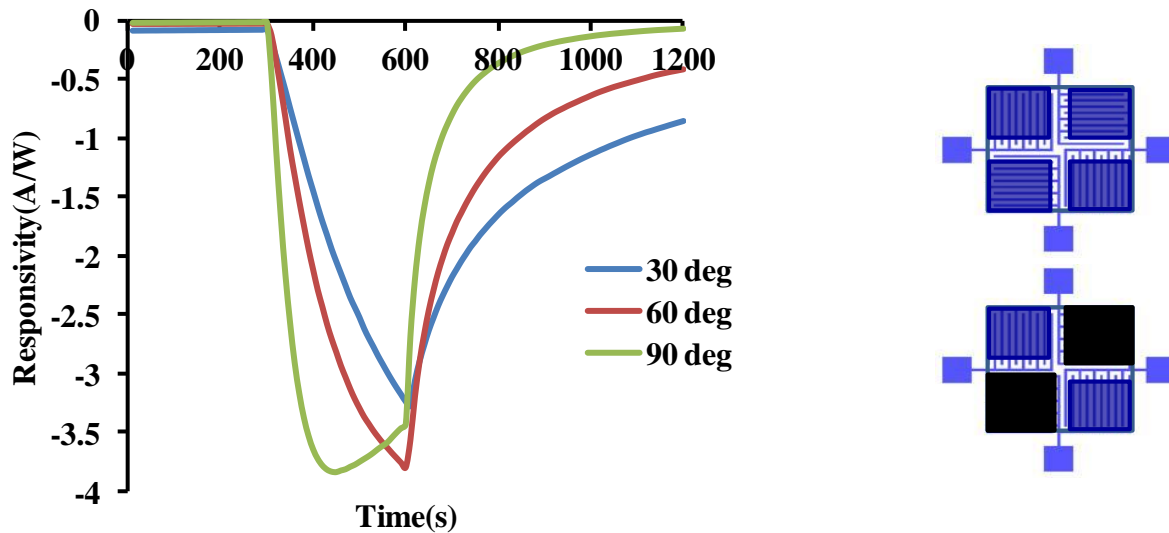
Figure 4-8   Response of the Symmetric Wheatstone bridge detector with pattern L_1 and rods grown for 16 hours to UV light for different temperature (Figure on the right top shows detector before masking and figure at right bottom after masking the diagonal quadrants with UV blocking film sheets for measuring the UV response)

atoms on the surface of the nanorod. On switching off the UV light, current initially fell drastically at the rate of 59 sec due to recombination of free electrons with holes in the bulk of the rods. Thereafter, the current fell very slowly due to recombination of electrons with holes on the surface of nanorods (**64, 65, 94, 95**). This process was very slow because electrons had to overcome the potential barrier in depletion region to reach the surface of rods. The fast and slow portion of the transient response of the detector at room temperature is shown in Figure 4-9.
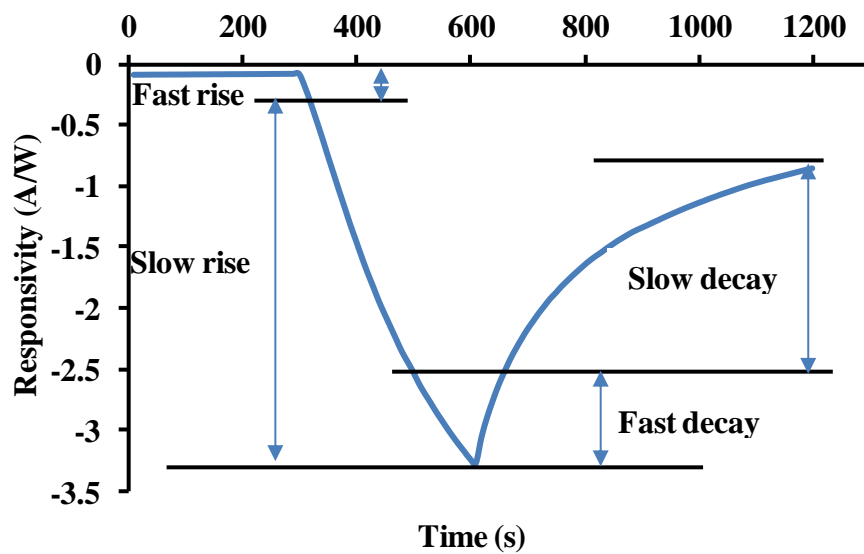
Figure 4-9   The fast and slow portion of the raise and decay curve of the transient response of the symmetric Wheatstone bridge detector measured at room temperature

At low temperature i.e., at room temperature and 60^0C, the current did not saturate even after 300 sec had elapsed. But at 90^0C the current saturated started to drop before 300 sec had elapsed. The detector response reached saturation at 90^0C but the response failed to saturate at room temperature and 60^0C because when temperature was raised the carriers gained sufficient energy to overcome the potential barrier of the depletion region due to the high temperature. Apart from that, the oxygen desorbed from the nanorod surface due to hole recombination were flushed out of the rods due to the high temperature. Hence, the oxygen concentration on the rod surface

started depleting, so the responsivity of the detector started to drop. Comparing the transient response curve for different temperatures, the trace followed different paths. This was an indication that the bridge was not able to completely cancel the affect of temperature on the responsivity of the detector. Comparing the maximum responsivity attained at different temperatures before the UV light was switched off, the responsivity value at 60^0C and 90^0C changes from the room temperature responsivity by 17%. Comparison of the maximum responsivity attained at different temperatures before the UV light was switched off is shown in Figure 4-10. To know whether the Wheatstone bridge actually helped in cancelling the effects of
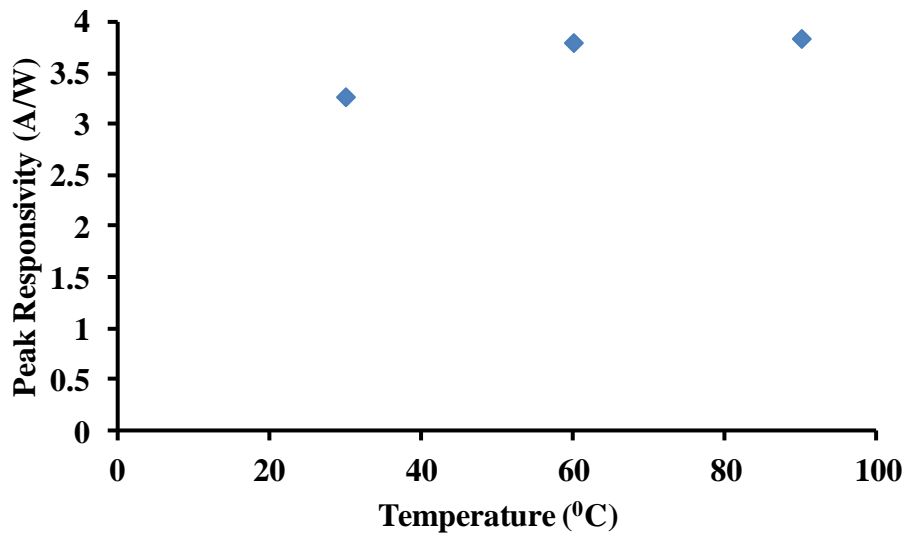
Figure 4-10   Comparison of the maximum responsivity attained at different ambient temperature by symmetric Wheatstone bridge (pattern L₁) before the UV light is switched off

temperature, the transient response of individual quadrants of a symmetric Wheatstone bridge detector to UV light at different temperatures was examined. The transient response of the individual quadrants of a symmetric Wheatstone bridge at temperatures of 30^0C, 60^0C, 90^0C are shown in Figure 4-11. The connection diagram for measuring the response of individual

quadrants of a symmetric Whetstone bridge is also shown in Figure 4-11. The response curve had different traces for different temperatures. The responsivity at 90^0C dropped after the response saturated. The maximum responsivity of the response trace at different temperatures for individual quadrants of the symmetric Wheatstone bridge detector were compared with the response trace of the symmetric Wheatstone bridge detector operated in Wheatstone bridge mode. The deviation of the maximum response attained at different temperatures before the UV light was switched off was 40% when not operated in Wheatstone bridge mode. But the absolute responsivity value was less when the detector is operated in Wheatstone bridge mode. For
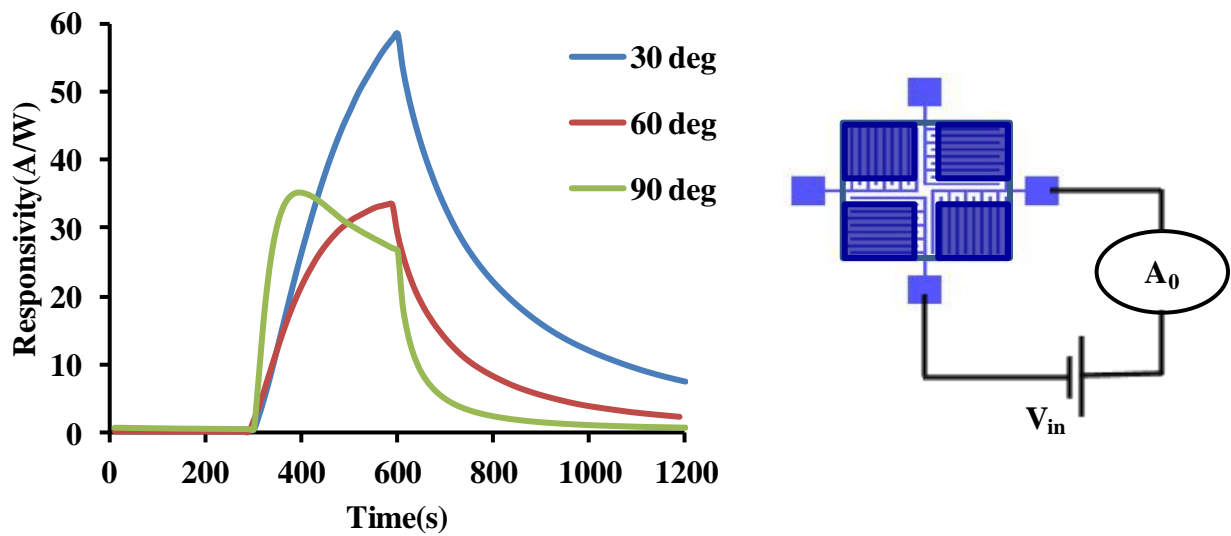
Figure 4-11 Response of the individual quadrant of symmetric Wheatstone bridge detector with pattern L$_1$ and rods grown for 16 hours to UV light for different temperature (Figure on the right depicts the connection diagram for measuring the UV response)

example, the maximum responsivity at room temperature when operated in Wheatstone bridge mode was only 3.3 A/W (Figure 4-8), but the responsivity of individual quadrant of the symmetric Wheatstone was about 58.5 A/W (Figure 4-11). A comparison of maximum responsivity reached at different temperatures for individual quadrants of a symmetric

Wheatstone bridge is shown in Figure 4-12. On comparing Figure 4-12 with Figure 4-10, it shows that deviation of the maximum responsivity at different temperatures for individual quadrants was 40% and for symmetric Wheatstone it was 17%. Hence, operation of detector in Wheatstone bridge mode was able to partly cancel the effects of temperature variation.
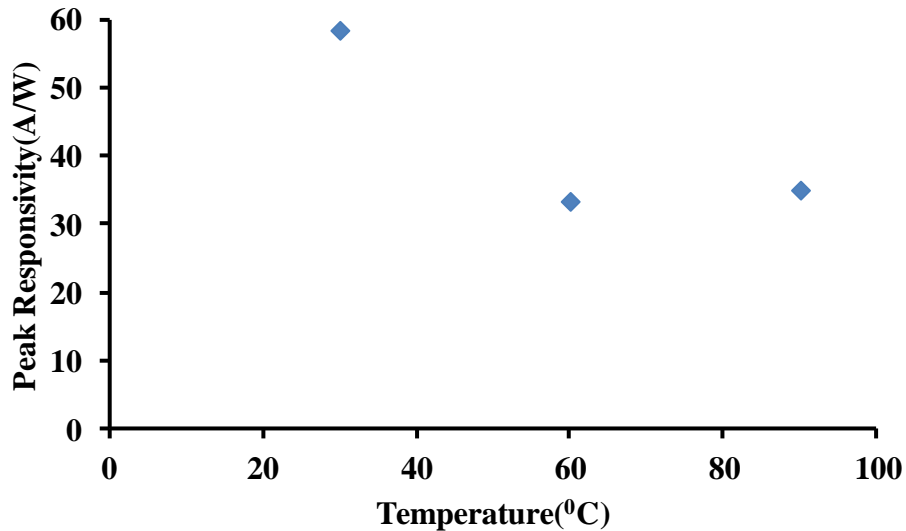
Figure 4-12   Comparison of the maximum responsivity attained at different ambient temperature by individual quadrant of symmetric Wheatstone bridge before the UV light is switched off

4.3.2   Transient Response of Asymmetric Wheatstone UV Detector

For probing the advantages of fabricating the detector symmetrically, the transient response of an asymmetrically fabricated detector was examined. Figure 4-13 shows the transient response of an asymmetric Wheatstone bridge detector with rod growth only in one quadrant at different temperatures. The response was measured by masking the diagonal quadrants to UV light (as shown on the right side of Figure 4-13) and biasing the circuit as shown in Figure 4-1(b). The transient response traces of an asymmetric Wheatstone bridge with rod growth in one quadrant, follow different paths for different temperatures. For symmetric Wheatstone bridge the response failed to saturate at room temperature before the UV light was switched off. However, for

asymmetric Wheatstone the room temperature response reached its saturation before the UV light was switched off. At 60^0C and 90^0C, the response reached saturation in 100 sec and 40 sec, respectively, after the UV light was switched on and then started to drop. This was due to surface area of the seed layers less by 10^3 times compared to rods, thereby, reducing the oxygen adsorption amount on the surface **(45, 96, 97)**. Comparison of the maximum responsivity reached
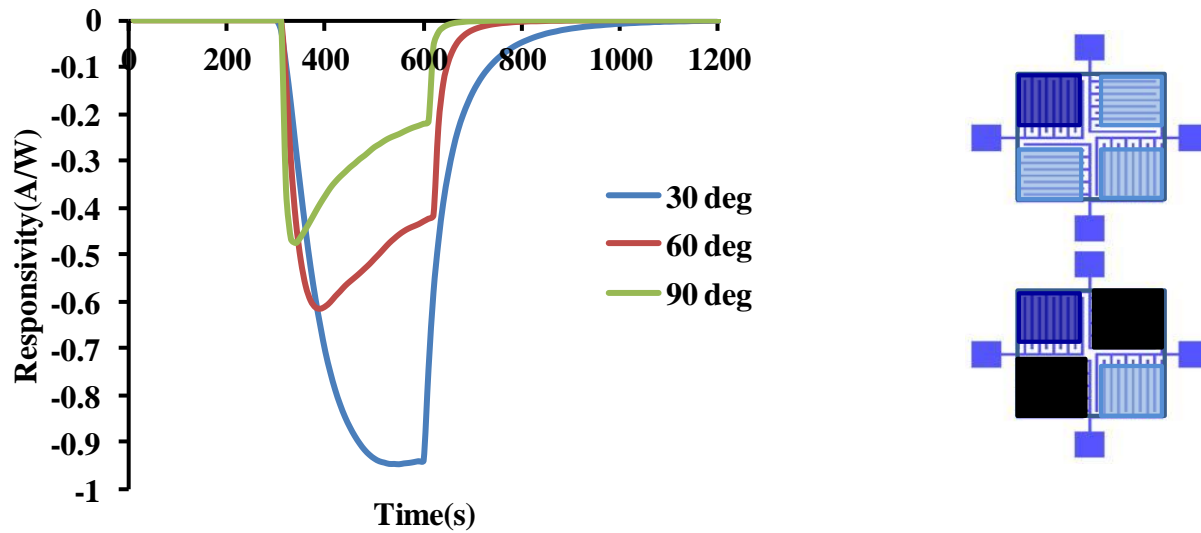
Figure 4-13   Response of the asymmetric Wheatstone bridge detector with pattern L$_1$ and rods grown for 16 hours only in one quadrant to UV light for different temperature (Figure on the right top shows detector before masking and figure at right bottom after masking the diagonal quadrants with UV blocking film sheets for measuring the UV response)

for the transient response of an asymmetric Wheatstone bridge with rods grown only in one quadrant at different temperatures is shown in Figure 4-14. The maximum responsivity attained at 60^0C and 90^0C changed from the room temperature response by 35% and 50%, respectively. The maximum absolute responsivity value was less for asymmetric Wheatstone bridge with rods in one quadrant. The maximum absolute responsivity value was less for asymmetric Wheatstone bridge with rods in one quadrant due to quadrants without rods whose response was about 10^2

times less compared to quadrants with rods. Comparing the variation of an asymmetric detector having rods in one quadrant (Figure 4-14) with a symmetric Wheatstone bridge detector at different temperature (Figure 4-10), the variation was two to three times more for an asymmetric Wheatstone bridge detector. While comparing it with the response of individual quadrants of symmetric Wheatstone bridge at 90^0C (Figure 4-12), the variation was 10% more for asymmetric Wheatstone bridge detector.
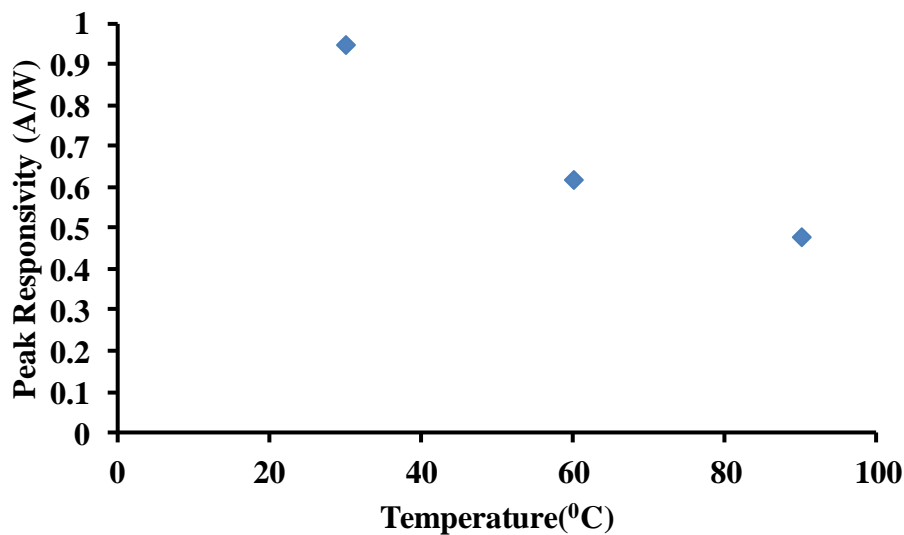
Figure 4-14   Comparison of the maximum responsivity attained at different ambient temperature before the UV light is switched off by asymmetric Wheatstone bridge with rod grown only in one quadrant.

The ability of a symmetric Wheatstone bridge to negate the effects of temperature can be well appreciated by looking at the response of an asymmetric Wheatstone bridge with rods in three quadrants grown for 16 hours. The transient response of an asymmetric Wheatstone bridge with rods in three quadrants is shown in Figure 4-15. When rod growth was increased from one quadrant to three quadrants, though the response traces follow different paths for different temperatures, the variation in maximum responsivity before the UV light is switched off for different temperatures was 6% from the room temperature response. Comparison of the

83

maximum responsivity of the asymmetric Wheatstone bridge with rod growth in three quadrants before the UV light was switched off is shown in Figure 4-16. The absolute value of maximum
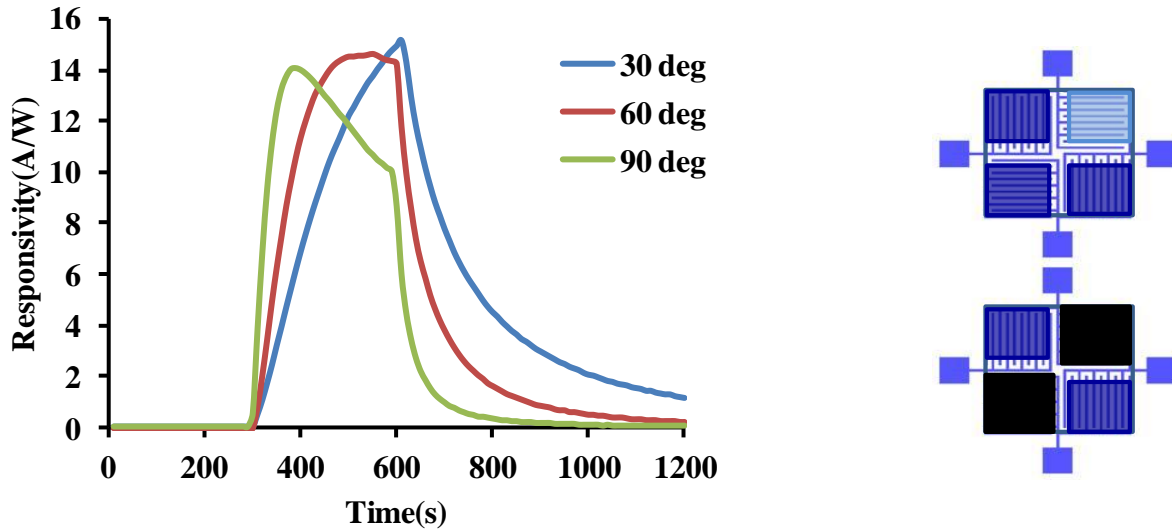
Figure 4-15 Response of the asymmetric Wheatstone bridge detector with pattern L_1 and rods grown for 16 hours in three quadrant, to UV light for different temperature (Figure on the right depicts masking of the diagonal quadrants using UV blocking film sheets for measuring the UV response)
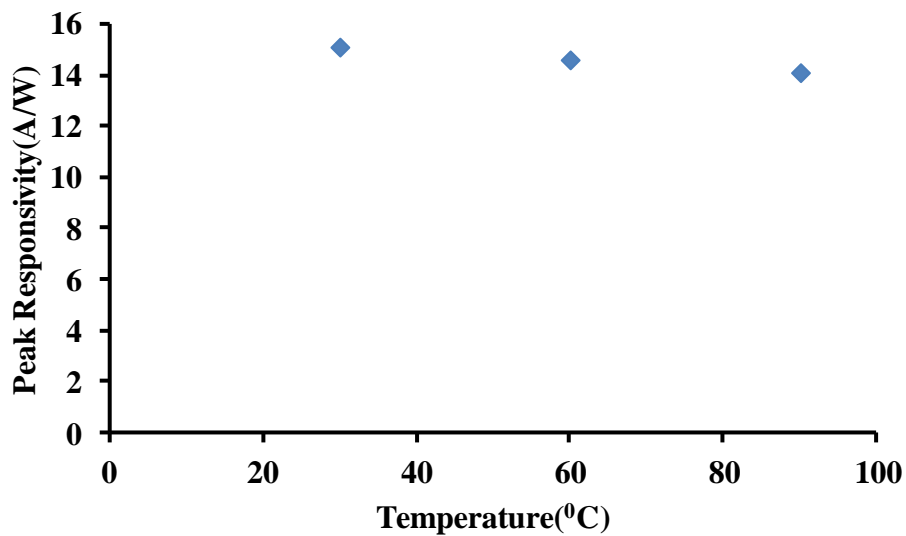
Figure 4-16 Comparison of the maximum responsivity attained at different ambient temperatures before the UV light is switched off by asymmetric Wheatstone bridge with rod growth in three quadrants.

responsivity before the UV light was switched off for the asymmetric Wheatstone bridge with rod growth in three quadrants for different temperatures was higher than the symmetric Wheatstone bridge detector by 11 A/W and for the asymmetric Wheatstone bridge detector with rod growth in one quadrant by 14 A/W. The absolute value of maximum responsivity was higher for the asymmetric Wheatstone bridge detector with rods grown in three quadrants due to combination of unbalanced nature of the bridge as well as exposure of diagonal quadrants with rods to UV light.

The peak responsivity at different temperature for symmetric, individual quadrants, asymmetric (with rod in one quadrant), asymmetric (with rod in three quadrant) plotted on a single graph is shown in Figure 4-17.
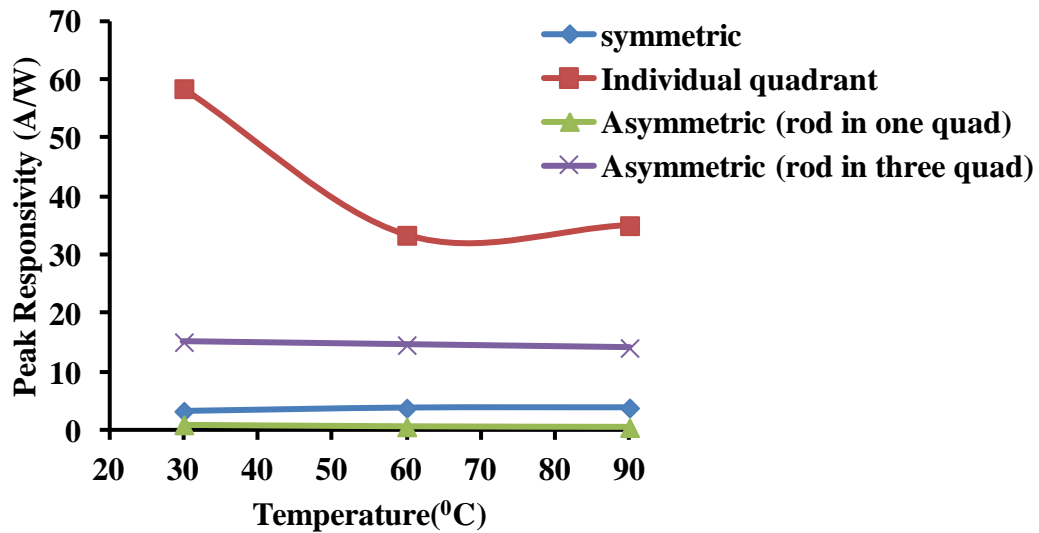
Figure 4-17   Comparison of the maximum responsivity attained at different ambient temperatures before the UV light is switched off for symmetric, individual quadrant, asymmetric (rods in one quadrant) and asymmetric (rods in three quadrants) Wheatstone bridge UV detector.

4.3.3 Time constant of the Transient Response of Wheatstone Bridge UV Detector

The time constants for the rise process and decay process of the transient photocurrent curve of the symmetric and asymmetric Wheatstone bridges were determined by fitting the data with exponential curves as follows:

The rise process: $I = I_0\left(1 - \exp\left(-\frac{t}{\tau}\right)\right)$ Eq (4-1)

The decay process $I = I_0 \exp\left(-\frac{t}{\tau_1}\right) + I_0' \exp\left(-\frac{t}{\tau_2}\right)$ Eq (4-2)

where I is the transient photocurrent, I_0 and and I_0' is the steady photocurrent, t is the time, and τ is the the relaxation time constant (93).

The time constants of the transient response curves for symmetric Wheatstone bridges, individual quadrants of the symmetric Wheatstone bridge and asymmetric Wheatstone bridges are shown in Table 4-3. Table 4-3 shows the time constants for rise portion and fast and slow part (Figure 4-9) of the decay portion of the transient response at different temperatures. Comparison of the time constants for rise portion and fast and slow parts of the decay portion at different temperatures for different detector configurations are shown in Figures 4-18, 4-19, and 4-20, respectively. The time constant was less for asymmetric Wheatstone bridge with rods in one quadrant. This was because seed layer has a less surface area than rods, so oxygen adsorption was less for the seed layer (45, 96, 97). Hence, the response was faster for the seed layer. As the number of quadrants with rods in the detector was increased, the response time also increased due to high adsorption of oxygen on the rod surface. When the ambient temperature was increased, the time constant decreased. The decrease in time constant with increase in temperature was due to an increase in diffusion velocity of electrons from the rod to the seed

86

layer, and also due to the increases in energy to overcome the depletion potential at the rod surface.

Table 4-3   Time constants of the transient response curve of symmetric Wheatstone bridge, individual quadrant of the symmetric Wheatstone bridge and asymmetric Wheatstone bridge at different temperatures.

Temperature [^{0}C]	Raising portion [sec]	Decay portion	
		Faster decay [sec]	Slower decay [sec]
Symmetric Wheatstone bridge (Rods in four quadrants)			
30	299	59	345
60	146	40	217
90	49	29	126
Non- Wheatstone bridge			
30	257	63	262
60	129	45	190
90	32	26	121
Asymmetric Wheatstone bridge (Rods only in one quadrant)			
30	71	26	89
60	22	12	42
90	7	5	23
Asymmetric Wheatstone bridge (Rods in three quadrant)			
30	217	50	202
60	71	35	125
90	28	25	93
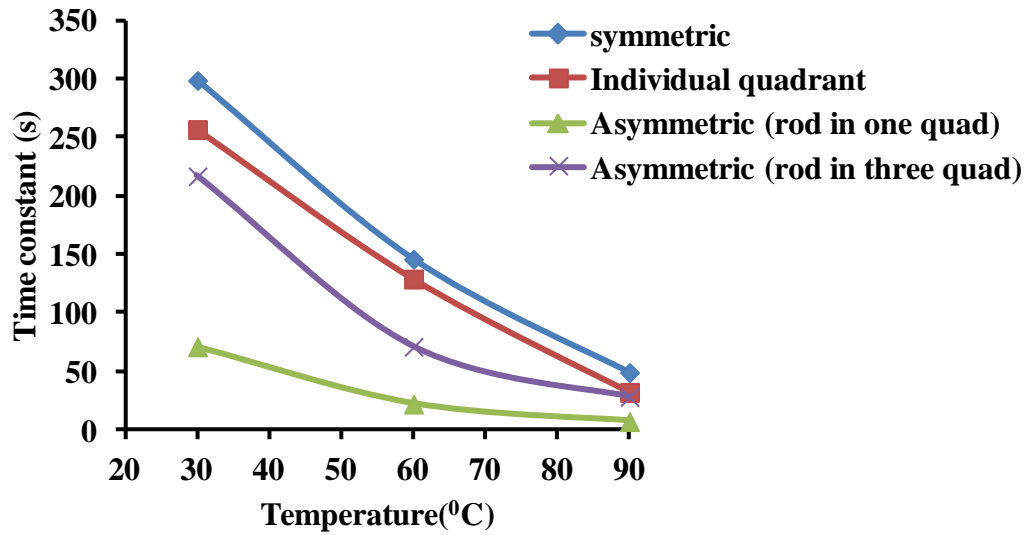
Figure 4-18　Comparison of the time constants of rise portion of transient response curve at different temperatures for different configurations
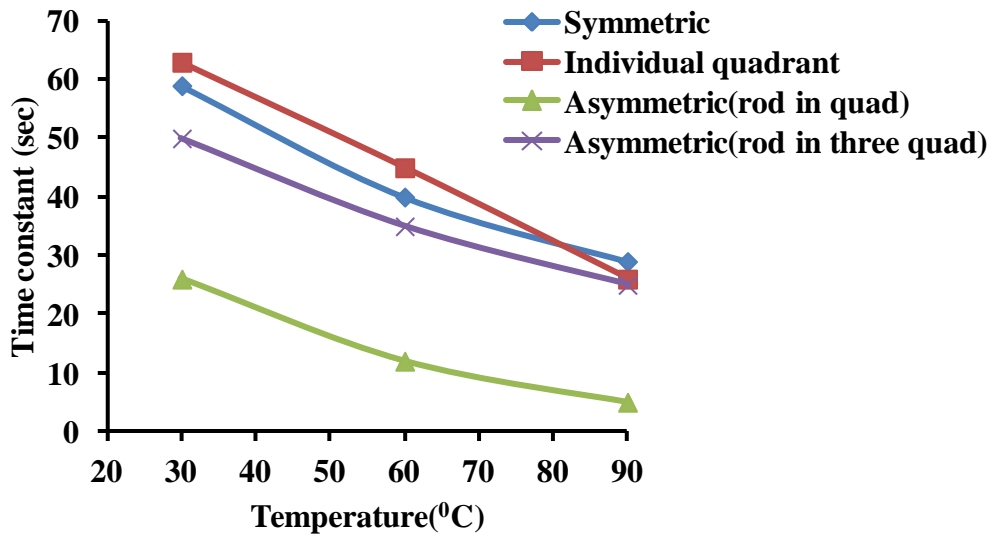
Figure 4-19　Comparison of the time constants of fast decay portion of transient response curve at different temperatures for different configurations
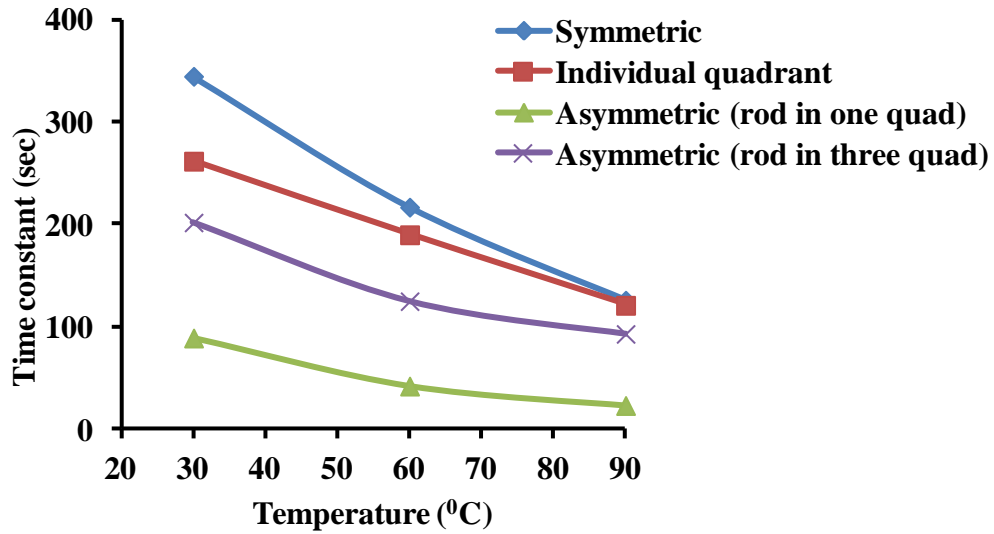
Figure 4-20   Comparison of the time constants of slow decay portion of transient response curve at different temperatures for different configurations

4.4   RESPONSE STABILITY OF SYMMETRIC WHEATSTONE UV DETECTOR

The expectation was that a symmetric Wheatstone bridge would be able to bring down the effects of temperature variation on the response of detector below 10%. The response of a symmetric Wheatstone bridge at different temperatures showed that complete cancellation did not occur. The reason for this was that the response of the detector was measured by masking the diagonal quadrants. Though when the diagonal quadrants were masked, the change in resistance of all four quadrants of the detector before UV exposure was the same, hence they cancel out. But change in UV response of the exposed quadrants at different temperatures is not cancelled out since only two quadrants were exposed. Showing mathematically that cancellation of the temperature effects on UV response is not possible by exposing only the two quadrants was examined.

As shown in Figure 4-2, resistance of the four quadrants is represented as R_1, R_2, R_3 and R_4. The detector is biased along one of the diagonals with input voltage V_{in}, the output voltage along the other diagonal is represented as V_0 and the bridge current along the diagonal is represented as A_0. The relation of the output voltage V_0 to the resistances of the four quadrants is given by,

$$V_o = \left[\left(\frac{R_3}{R_2 + R_3}\right) - \left(\frac{R_4}{R_1 + R_4}\right)\right] V_{in} \qquad \text{Eq } (4-2)$$

Let R_1, R_2, R_3 and R_4 be the resistances of the four quadrants at room temperature. For symmetric Wheatstone bridge $R_1=R_2=R_3=R_4=R$. Then the output voltage at room temperature before exposure to UV light can be rewritten as,

$$V_o = \left[\left(\frac{R}{R + R}\right) - \left(\frac{R}{R + R}\right)\right] V_{in} = 0 \qquad \text{Eq } (4-3)$$

If ΔR_T is the increase in resistance for a temperature T above the room temperature, let ΔR_I be the decrease in resistance on exposure to UV light at room temperature and $\Delta R_{I(T)}$ be the increase in resistance on exposure to UV light at a temperature T above the room temperature.

The output voltage at room temperature when exposed to UV light is then given by,

$$V_o = \left[\left(\frac{R - \Delta R_I}{R + R - \Delta R_I}\right) - \left(\frac{R}{R - \Delta R_I + R}\right)\right] V_{in} \qquad \text{Eq } (4-4)$$

$$V_o = \left[\frac{-\Delta R_I}{(R - \Delta R_I) + R}\right] V_{in} \qquad \text{Eq } (4-5)$$

The net resistance of the circuit before UV exposure is given by,

$$R_o = \left[\left(\frac{R_3 R_2}{R_3 + R_2}\right) + \left(\frac{R_1 R_4}{R_1 + R_4}\right)\right] \qquad \text{Eq } (4-6)$$

90

$$R_o = \left[\left(\frac{RR}{R+R}\right) + \left(\frac{RR}{R+R}\right)\right]$$

Eq (4 − 7)

$$R_o = \left(\frac{2R^2}{2R}\right) = R$$

Eq (4 − 8)

The net resistance of the circuit after UV exposure is given by,

$$R_o = \left[\frac{2(R - \Delta R_I)R}{(R - \Delta R_I) + R}\right]$$

Eq (4 − 9)

The net output current on UV exposure is given by

$$I_o = \frac{V_o}{R_o} = \left[\frac{-\Delta R_I}{2(R - \Delta R_I)R}\right] V_{in}$$

Eq (4 − 10)

The output voltage at room temperature when exposed to UV light at temperature T above the room temperature is then given by,

$$V_o = \left[\left(\frac{R + \Delta R_T - \Delta R_I + \Delta R_{I(T)}}{R + \Delta R_T - \Delta R_I + \Delta R_{I(T)} + R + \Delta R_T}\right)\right.$$

$$\left. - \left(\frac{R + \Delta R_T}{R + \Delta R_T - \Delta R_I + \Delta R_{I(T)} + R + \Delta R_T}\right)\right] V_{in}$$

Eq (4 − 11)

$$V_o = \left[\left(\frac{-\Delta R_I + \Delta R_{I(T)}}{R + \Delta R_T - \Delta R_I + \Delta R_{I(T)} + R + \Delta R_T}\right)\right] V_{in}$$

Eq (4 − 12)

$$V_o = \left[\left(\frac{-\Delta R_I + \Delta R_{I(T)}}{(R - \Delta R_I) + R + 2\Delta R_T + \Delta R_{I(T)}}\right)\right] V_{in}$$

Eq (4 − 13)

The net resistance of the circuit after UV exposure for a temperature T above room temperature is given by,

91

$$R_o = \left(\frac{2\left(R + \Delta R_T - \Delta R_I + \Delta R_{I(T)}\right)\left(R + \Delta R_T\right)}{\left(R + \Delta R_T - \Delta R_I + \Delta R_{I(T)}\right) + \left(R + \Delta R_T\right)} \right) \qquad \text{Eq (4-14)}$$

$$R_o = \left(\frac{2\left(R + \Delta R_T - \Delta R_I + \Delta R_{I(T)}\right)\left(R + \Delta R_T\right)}{\left(R - \Delta R_I\right) + R + \Delta R_{I(T)} + 2\Delta R_T} \right) \qquad \text{Eq (4-15)}$$

The net output current on UV exposure for temperature T above room temperature is given by

$$I_o = \frac{V_o}{R_o} = \left[\left(\frac{-\Delta R_I + \Delta R_{I(T)}}{2\left(R + \Delta R_T - \Delta R_I + \Delta R_{I(T)}\right)\left(R + \Delta R_T\right)} \right) \right] V_{in} \qquad \text{Eq (4-16)}$$

$$I_o = \frac{V_o}{R_o} = \left[\left(\frac{-\Delta R_I + \Delta R_{I(T)}}{2\left(\left(R - \Delta R_I\right) + \left(\Delta R_T + \Delta R_{I(T)}\right)\right)\left(R + \Delta R_T\right)} \right) \right] V_{in} \qquad \text{Eq (4-17)}$$

$$I_o = \frac{V_o}{R_o} = \left[\left(\frac{-\Delta R_I + \Delta R_{I(T)}}{\begin{array}{l} 2[(R - \Delta R_I)R + (R - \Delta R_I)\Delta R_T + \\ R\left(\Delta R_{I(T)} + \Delta R_T\right) + \left(\Delta R_T + \Delta R_{I(T)}\right)\Delta R_T] \end{array}} \right) \right] V_{in} \qquad \text{Eq (4-18)}$$

Since ΔR_T and $\Delta R_{I(T)}$ are smaller ($<10^2$) compared to the room temperature resistance R and the change in resistance on ΔR_I, the output voltage can be approximated as,

$$I_o = \frac{V_o}{R_o} \sim \left[\frac{-\Delta R_I + \Delta R_{I(T)}}{2(R - \Delta R_I)R} \right] V_{in} \qquad \text{Eq (4-19)}$$

Hence, the response of a symmetric Wheatstone bridge measured by masking the diagonal quadrants for different temperatures is dependent on temperature term $\Delta R_{I(T)}$. The temperature dependence can be avoided if all the four quadrants are exposed to UV light. But for a symmetric Wheatstone detector the output will be zero if all the four quadrants are exposed to UV light. This could be overcome if the dimension of the rods grown along the diagonal quadrants were

equal but different from the other diagonal. This structure is known as quasi-symmetric Wheatstone bridge. The details of quasi-symmetric Wheatstone bridge are discussed in the next chapter.

5.   WHEATSTONE BRIDGE UV DETECTOR (QUASI-SYMMETRIC)

The previous chapter dealt with the fabrication of a symmetric bridge and an asymmetric Wheatstone bridge (rods in three quadrants and rods in one quadrant) based UV detector for obtaining a stable UV response with change in ambient temperature. Both the symmetric and the asymmetric Wheatstone bridge detector where operated by exposing the diagonal quadrants to UV light while the other two diagonals where masked from UV light. The studies on the response of the symmetric and asymmetric based detectors showed that the response of the detector for the symmetric configuration is better compared to the asymmetric Wheatstone bridge detector, since the change in responsivity from room temperature when temperature is raised is only 17 %. By analyzing the transient response curve of the symmetric Wheatstone bridge it was seen that the trace of the rising part of the curve, the decay curve, and the maximum photoresponse for the same UV exposure time was different for different ambient temperatures. In the previous chapter it was shown that this was because the unbalanced bridge current for different temperatures on UV exposure was dependent on the response of the exposed quadrants along the diagonal. In other words, since only two of the quadrants along one of the diagonal were exposed to UV light while the other two quadrants along the other diagonal were not exposed to UV light, there was no cancellation of the temperature effects on the UV response. In this chapter, studies of the length of the rods grown on symmetric Wheatstone bridge was tailored to determine if this would improve temperature stability.

5.1 QUASI-SYMMETRIC WHEATSTONE BRIDGE UV DETECTOR

5.1.1 Structure of Quasi-Symmetric Wheatstone Bridge UV Detector

To know whether the effects of temperature on the UV response variation could be kept below 17% if all the four quadrants of the symmetric bridge are exposed to UV light but the problem with exposing all four quadrants of a symmetric bridge is that the bridge current will be zero because of the symmetric nature of the quadrants of the detector. Simultaneously exposing all four quadrants of the detector as well as obtaining a bridge current is possible if rods are grown along the four quadrants such that the rod length along the diagonal quadrants are equal but different from the length of the rods in the other diagonal of the Wheatstone detector **(112)**. This kind of detector structure is known a quasi-symmetric Wheatstone bridge structure. The schematic diagram of the quasi symmetric Wheatstone bridge structure is shown in Figure 5-1.
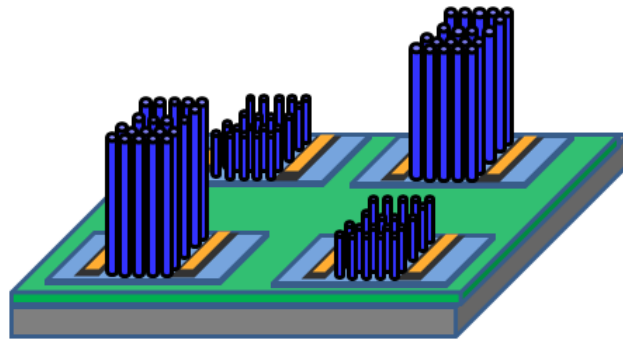
Figure 5-1   Schematic diagram of the quasi-symmetric Wheatstone bridge structure

5.1.2 Theoretical Output of Quasi-symmetric Wheatstone Bridge UV Detector

The negation of the temperature effects of the UV response by employing a quasi symmetric Wheatstone bridge can be explained using the Eq. (5-1) that relating the bridge voltage along the diagonals opposite to that of the biasing diagonal with the resistance of the four quadrants. The

schematic diagram of the Wheatstone bridge circuit is shown in Figure 5-2. As shown in Figure 5-2 the resistance of the four quadrants is represented as R_1, R_2, R_3 and R_4. The detector is biased along one of the diagonals with input voltage V_{in}, the output voltage along the other diagonal is represented as V_0, and the bridge current along the diagonal is represented as A_0. The relation of the output voltage V_0 to the resistance of the four quadrants is given by,

$$V_o = \left[\left(\frac{R_3}{R_2 + R_3}\right) - \left(\frac{R_4}{R_1 + R_4}\right)\right] V_{in} \qquad \text{Eq } (5-1)$$
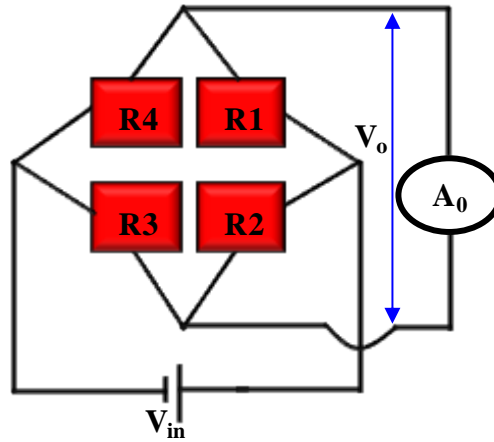
Figure 5-2   Schematic diagram of the Wheatstone bridge circuit

Let R_1, R_2, R_3 and R_4 be the resistance of the four quadrants at room temperature. In case of quasi symmetric Wheatstone bridge $R_1=R_3$ and $R_2=R_4$. If $R_1=R_3=R$ and $R_2=R_4=R'$, then the output voltage at room temperature before exposure to UV light can be rewritten as,

$$V_o = \left[\left(\frac{R}{R' + R}\right) - \left(\frac{R'}{R + R'}\right)\right] V_{in} \qquad \text{Eq } (5-2)$$

If ΔR_T and $\Delta R'_T$ are the increase in resistances for a temperature T above the room temperature, ΔR_I and $\Delta R'_I$ are the decrease in resistance on exposure to UV light at room temperature, and

$\Delta R_{I(T)}$ and $\Delta R^{'}_{I(T)}$ are the increases in resistance on exposure to UV light at a temperature T above the room temperature corresponding to the quadrants R_1, R_3 and R_2, R_4, respectively, then output voltage at room temperature when exposed to UV light is given by,

$$V_o = \left[\left(\frac{R - \Delta R_I}{R' - \Delta R'_I + R - \Delta R_I}\right) - \left(\frac{R' - \Delta R'_I}{R - \Delta R_I + R' - \Delta R'_I}\right)\right] V_{in} \qquad \text{Eq (5-3)}$$

$$V_o = \left[\left(\frac{(R - \Delta R_I) - (R' - \Delta R'_I)}{(R' - \Delta R'_I) + (R - \Delta R_I)}\right)\right] V_{in} \qquad \text{Eq (5-4)}$$

The net resistance of the circuit before UV exposure is given by,

$$R_o = \left[\left(\frac{R_3 R_2}{R_3 + R_2}\right) + \left(\frac{R_1 R_4}{R_1 + R_4}\right)\right] \qquad \text{Eq (5-5)}$$

$$R_o = \left[\left(\frac{R_3 R_2}{R_3 + R_2}\right) + \left(\frac{R_1 R_4}{R_1 + R_4}\right)\right] \qquad \text{Eq (5-6)}$$

$$R_o = \left[\left(\frac{RR'}{R + R'}\right) + \left(\frac{RR'}{R + R'}\right)\right] \qquad \text{Eq (5-7)}$$

$$R_o = \left(\frac{2RR'}{R + R'}\right) \qquad \text{Eq (5-8)}$$

The net resistance of the circuit after UV exposure is given by,

$$R_o = \left(\frac{2(R - \Delta R_I)(R' - \Delta R'_I)}{(R - \Delta R_I) + (R' - \Delta R'_I)}\right) \qquad \text{Eq (5-9)}$$

The net output current on UV exposure is given by

$$I_o = \frac{V_o}{R_o} = \left[\frac{(R - \Delta R_I) - (R' - \Delta R'_I)}{2(R - \Delta R_I)(R' - \Delta R'_I)}\right] V_{in} \qquad \text{Eq (5-10)}$$

97

The output voltage when exposed to UV light at temperature T above the room temperature is given by,

$$V_o = \left[\left(\frac{R + \Delta R_T - \Delta R_I + \Delta R_{I(T)}}{R' + \Delta R'_T - \Delta R'_I + \Delta R'_{I(T)} + R + \Delta R_T - \Delta R_I + \Delta R_{I(T)}}\right)\right.$$

$$\left.- \left(\frac{R' + \Delta R'_T - \Delta R'_I + \Delta R'_{I(T)}}{R + \Delta R_T - \Delta R_I + \Delta R_{I(T)} + R' + \Delta R'_T - \Delta R'_I + \Delta R'_{I(T)}}\right)\right] V_{in} \qquad \text{Eq (5 − 11)}$$

$$V_o = \left[\left(\frac{R + \Delta R_T - \Delta R_I + \Delta R_{I(T)} - R' - \Delta R'_T + \Delta R'_I - \Delta R'_{I(T)}}{R' + \Delta R'_T - \Delta R'_I + \Delta R'_{I(T)} + R + \Delta R_T - \Delta R_I + \Delta R_{I(T)}}\right)\right] V_{in} \qquad \text{Eq (5 − 12)}$$

If the properties of the rods are such that the effects of temperature is same in all the four quadrants then,

$$\Delta R_{I(T)} = \Delta R'_{I(T)} \text{ and } \Delta R_T = \Delta R'_T$$

$$V_o = \left[\left(\frac{(R - \Delta R_I) - (R' - \Delta R'_I)}{R' + \Delta R'_T - \Delta R'_I + \Delta R'_{I(T)} + R + \Delta R_T - \Delta R_I + \Delta R_{I(T)}}\right)\right] V_{in} \qquad \text{Eq (5 − 13)}$$

$$V_o = \left[\left(\frac{(R - \Delta R_I) - (R' - \Delta R'_I)}{(R - \Delta R_I) + (R' - \Delta R'_I) + 2\Delta R_{I(T)} + 2\Delta R_T}\right)\right] V_{in} \qquad \text{Eq (5 − 14)}$$

The net resistance of the circuit after UV exposure for a temperature T above room temperature is given by,

$$R_o = \left(\frac{2(R + \Delta R_T - \Delta R_I + \Delta R_{I(T)})(R' + \Delta R'_T - \Delta R'_I + \Delta R'_{I(T)})}{(R + \Delta R_T - \Delta R_I + \Delta R_{I(T)}) + (R' + \Delta R'_T - \Delta R'_I + \Delta R'_{I(T)})}\right) \qquad \text{Eq (5 − 15)}$$

$$R_o = \left(\frac{2(R + \Delta R_T - \Delta R_I + \Delta R_{I(T)})(R' + \Delta R'_T - \Delta R'_I + \Delta R'_{I(T)})}{(R - \Delta R_I) + (R' - \Delta R'_I) + 2\Delta R_{I(T)} + 2\Delta R_T}\right) \qquad \text{Eq (5 − 16)}$$

The net output current on UV exposure for temperature T above room temperature is given by

$$I_o = \frac{V_o}{R_o} = \left[\left(\frac{(R - \Delta R_I) - (R' - \Delta R'_I)}{2(R + \Delta R_T - \Delta R_I + \Delta R_{I(T)})(R' - \Delta R'_T + \Delta R'_I - \Delta R'_{I(T)})}\right)\right] V_{in} \qquad Eq\ (5-17)$$

$$I_o = \frac{V_o}{R_o} = \left[\left(\frac{(R - \Delta R_I) - (R' - \Delta R'_I)}{2(R + \Delta R_T - \Delta R_I + \Delta R_{I(T)})(R' - \Delta R'_T + \Delta R'_I - \Delta R'_{I(T)})}\right)\right] V_{in} \qquad Eq\ (5-18)$$

$$I_o = \frac{V_o}{R_o} = \left[\left(\frac{(R - \Delta R_I) - (R' - \Delta R'_I)}{2[(R - \Delta R_I)(R' - \Delta R'_I) + (R - \Delta R_I)(\Delta R_{I(T)} + \Delta R_T) + (R' - \Delta R'_I)(\Delta R_{I(T)} + \Delta R_T) + (\Delta R_{I(T)} + \Delta R_T)^2]}\right)\right] V_{in} \qquad Eq\ (5-19)$$

If $\Delta R_{I(T)}$, $\Delta R'_{I(T)}$, ΔR_T and $\Delta R'_T$ are neglected then the output voltage can be approximated as,

$$I_o = \frac{V_o}{R_o} \sim \left[\frac{(R - \Delta R_I) - (R' - \Delta R'_I)}{2(R - \Delta R_I)(R' - \Delta R'_I)}\right] V_{in} \qquad Eq\ (5-20)$$

Which is equal to the output current at room temperature.

5.1.3   Fabrication of Quasi-symmetric Wheatstone Bridge UV Detector

The fabrication procedure for the quasi-symmetric Wheatstone bridge was almost similar to that of the symmetric and asymmetric Wheatstone bridges. For growing rods of same length along the diagonal but different from the other diagonal, the quadrants along one of the diagonal were masked with photoresist. Thus rod growth took place only on the unmasked quadrants along the other diagonal. After growing rods for a desired length on the unmasked quadrants, rods were grown on the unmasked as well as masked quadrants after stripping the photoresist. The schematic representation of the different fabrication steps involved in the fabrication of quasi symmetric bridge is shown in Figure 5-3. Quasi symmetric Wheatstone bridges with the different

combinations of rod lengths that were grown for the fabrication of quasi-symmetric Wheatstone bridge are shown in Table 5-1.

Table 5-1   Rod combinations for the quasi symmetric Wheatstone bridge (note that rod dimension were based on an earlier study)

Sample No.	Quadrant 1 and 3			Quadrant 2 and 4		
	Growth time (hr)	Length of rods (μm)	Diameter of rods (nm)	Growth time (hr)	Length of rods (μm)	Diameter of rods (nm)
Q1	0	0	0	4	0.54-0.58	20.0-30.0
Q2	0	0	0	8	0.60-0.70	30.0-40.0
Q3	0	0	0	16	1.15-1.70	45.0-60.0
Q4	4	0.54-0.58	20.0-30.0	8	0.60-0.70	30.0-40.0
Q5	4	0.54-0.58	20.0-30.0	16	1.15-1.70	45.0-60.0
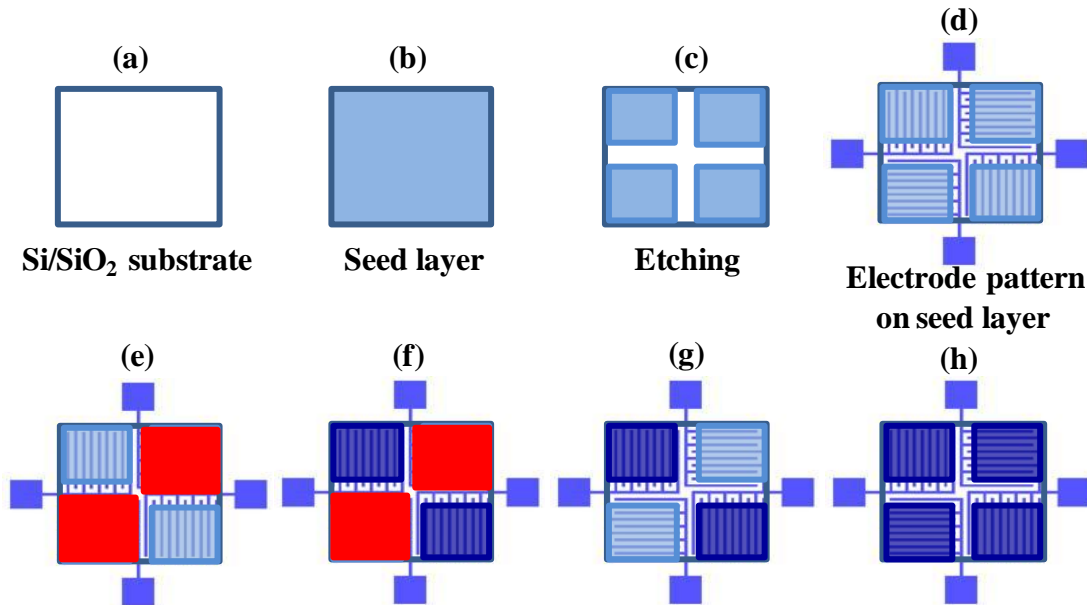
Figure 5-3   Fabrication steps for quasi-symmetric Wheatstone bridge

For a better explanation of the rod growth for the quasi-symmetric Wheatstone bridge, consider the quasi-symmetric detector with rods of length 0.54-0.58 μm on quadrants 1 and 3 and 1.15-1.75 μm on quadrants 2 and 4. Before the rod growth, quadrants 1 and 3 were masked with photoresist while quadrants 2 and 4 were not masked with photoresist. The sample was immersed in the nanorod growth solution for 12 hours so that rod growth took place only on quadrants 2 and 4. After 12 hours of rod growth, the sample was removed from the growth solution, then the masking on the quadrants 1 and 3 was removed by stripping the photoresist. The sample was again immersed in the growth solution for 4 hours, so that rod growth took place on all the four quadrants. Thus, quadrants 2 and 4 were exposed to the growth medium for 16 hours while quadrants 1 and 3 were exposed just for 4 hours.

5.2 RESPONSE OF QUASI-SYMMTERIC WHEATSTONE BRIDGE UV DETECTOR

5.2.1 Transient Response of Wheatstone Bridge UV Detector

The transient response of the fabricated quasi-symmetric Wheatstone bridge for the configurations described in Table 5-1 were measured using a UV lamp of wavelength 365 nm and intensity of 1 mW/cm^2. The response of the quasi symmetric Wheatstone bridge detector for the sample Q_1 is shown in Figure 5-4.

As expected, the trace of the transient response of the quasi-symmetric Wheatstone bridge Q_1 for different temperatures followed different paths because the temperature effect on the seed and rods for length 0.54-0.58 μm are different. The responsivity at room temperature was about 18.5 A/W and it drops to 18.3 A/W (1% change) and 12.5 A/W (33% change) at 60^0C and 90^0C,

respectively. The decrease in responsivity with increase in temperature was due to increase in recombination rate and prevention of readsorption of oxygen **(7, 65, 98, 99)**. The other interesting aspect of this response curve was the reversal of the bridge current for a brief time on UV exposure. This was explained by comparing the time constants of the transient response of the seed quadrant and rod quadrant. The time constants calculated from the transient response of the seed layer and rods of length 1.15-1.75 µm are shown in Table 5-2. The time constant for the
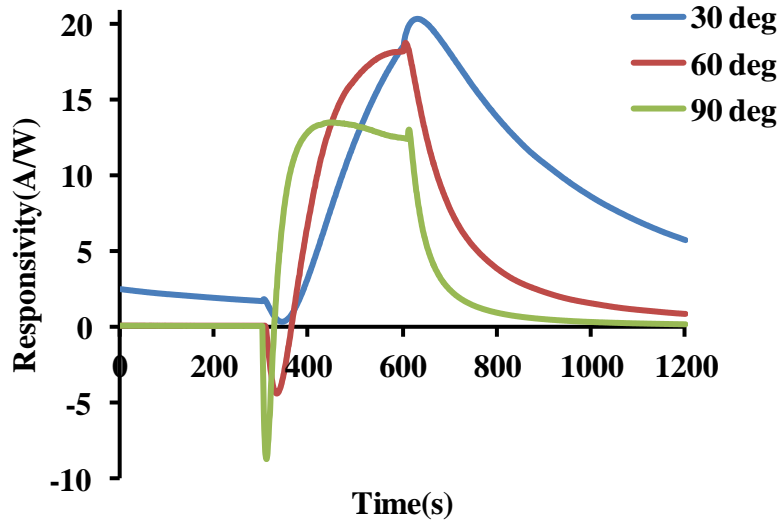
Figure 5-4   Transient response of quasi symmetric Wheatstone bridge (Q$_1$)

Table 5-2   Time constants of transient response of seed (40 nm) and rod (1.15-1.75 µm) for pattern L$_1$

	Temperature [^{0}C]	Raising portion [sec]	Decay portion	
			Faster decay [sec]	Slower decay [sec]
Seed	25	257	63	262
Rod	25	62	24	113

102

rise portion of the transient response of the seed was 62 sec for rod (0.54-0.58 μm) it was 257 sec. The time constant of the transient response depended on the amount of oxygen absorption on the surface of ZnO. In case of ZnO seed the surface area was less by 10^3 times compared to rod. Therefore, the time constant was small for seed than rod **(7, 65, 98)**. The reversal of the current was because the rate of decrease in resistance for the seed was greater than that of rod, as a result the resistance of the quadrants with the seed layer fell below the resistance of the quadrants with the rods. After a brief period, the resistance of the quadrants with rods fell below that of the seed, thereby reversing the bridge current. Before UV exposure the resistance of the seed layer quadrant was of the order of 10^9 ohm and for rod quadrant (0.54-0.58 μm) it was about 10^7 ohm. When exposed to UV light the resistance of the seed quadrant dropped to about 10^6 ohm and that of rod (0.54-0.58 μm) to about 10^5 ohm. Similarly, the rise in current when the UV light was switched off was explained. The seed layer returned to the dark condition pretty quick compared to the rods, thereby increasing the bridge current for a brief period. Once the resistance of the rod increases, the current starts to decay.

For sample Q_2 the response differed from the response of the sample Q_1. The room temperature responsivity for sample Q_2 was 17.3 A/W. When the temperature is raised, the responsivity dropped to 14.2 A/W (18% change) and 11.2 A/W (35% change) at 60^0C and 90^0C, respectively. The room temperature responsivity of the sample Q_2 was less by 1A/W than that of sample Q_1 due to the increase in diameter of the rods **(65, 98)**.

The response of the quasi symmetric Wheatstone bridge detector for sample Q_3 is shown in Figure 5-5. For sample Q_3 also the trace for transient response for different temperatures
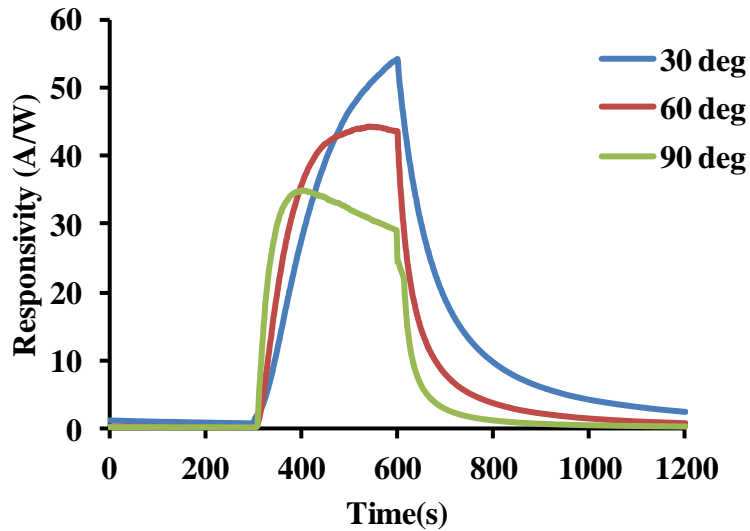
Figure 5-5   Transient response of quasi symmetric Wheatstone (Q₃)

followed different paths. The room responsivity for this combination was higher by 35.5 A/W compared to sample Q_1 because the bridge current increased with increase in the difference of resistance of the quadrants along the diagonals. The responsivity at room temperature was 54 A/W. When temperature was raised to 60^0C the responsivity dropped to 43.6 A/W (19% change). On increasing the temperature further to 90^0C the responsivity dropped to 26.2 A/W (51% change). The reversal of current on UV exposure as seen in Q_1 was not observed here. This was because the resistance of the seed layer and the rods with length 1.15-1.75 μm under dark conditions differed by about 10^3 ohm. The resistance of the seed under dark condition was of the order 10^9 ohm and for rod (1.15-1.75 μm) it was of the order 10^6 ohm. On UV exposure, the resistance dropped to 10^6 ohm for seed and for rod (1.15-1.75 μm) to 10^4 ohm. Hence, on exposure to UV light the resistance of the seed layer cannot drop below that of the rod though the drop in resistance rate is higher for seed than rod. Thus current reversal was not observed in sample Q_3 quasi-symmetric Wheatstone bridge.

The response of the quasi-symmetric Wheatstone bridge for sample Q_4 is shown in Figure 5-6. The trace of the transient response for different temperature for this case followed near retraceable paths. As mentioned previously, the temperature effects can be minimized if the temperature effects on all the four quadrants are almost the same. Since the rods along the diagonal differ from the other diagonal in terms of rod length and rod diameter by 100 nm and 10 nm, the temperature effects on the quadrants can be considered to be the same. The transient response curve shows that this seems to be the case. When compared to symmetric and asymmetric Wheatstone bridge the traces of the transient response for different temperature nearly retraces for quasi-symmetric detector Q_4. The responsivity was about 1.13 A/W at room temperature. The responsivity drops to about 1 A/W when temperature raised to 60^0C and at
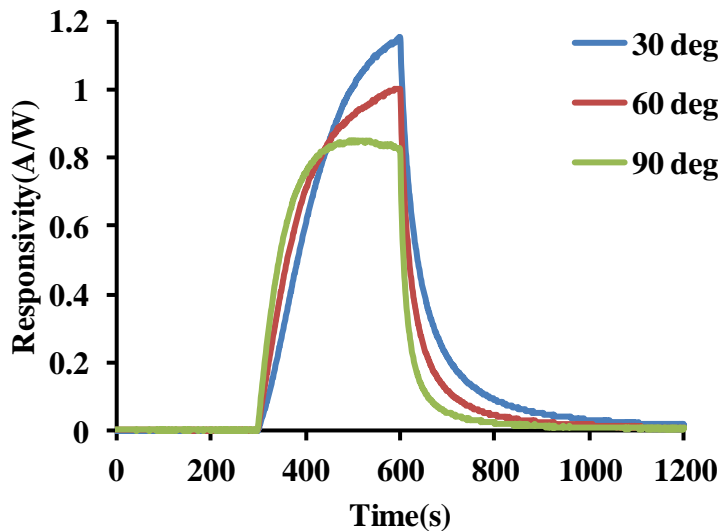
Figure 5-6   Transient response of quasi symmetric Wheatstone bridge (Q_4)

90^0C the responsivity further dips to 8.4×10^{-1} A/W. The change in responsivity at 60^0C with respect to room temperature was only 0.13 A/W (a 10% decline) and at 90^0C it was only about 0.34 A/W (a 25 % decline).   The responsivity of the quasi-symmetric detector Q_4 was less

compared to the symmetric Wheatstone bridge detectors by 2 A/W and for asymmetric Wheatstone bridge detectors with rods in three quadrants by 14 A/W. Also, for quasi-symmetric detector Q_4 the responsivity did not drop after saturation.

The responsivity of the quasi-symmetric for sample Q_5 is shown in Figure 5-7. In this case, the trace of the transient response at different temperatures followed different paths. The responsivity at room temperature is about 25.6 A/W. At 60^0C the responsivity is about 17 A/W and at 90^0C the responsivity is 13.6 A/W. Thus, the change in responsivity with respect to room temperature for 60^0C and 90^0C is 8.6 A/W (a change of 33 %) and 12 A/W (a change of 47 %),
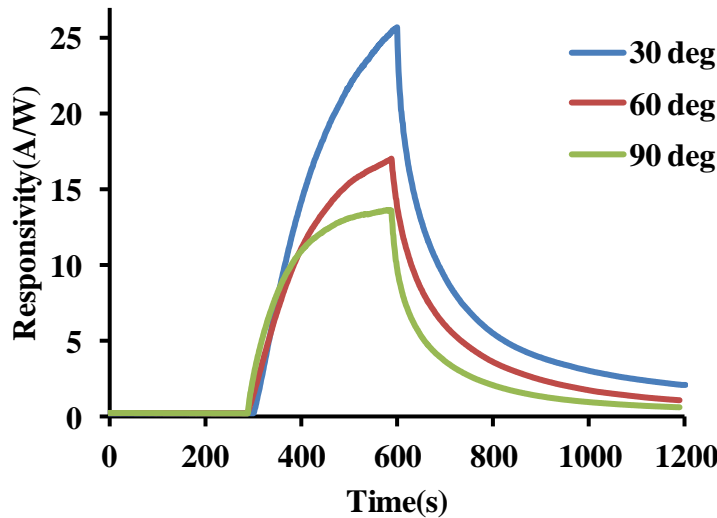
Figure 5-7   Transient response of quasi symmetric Wheatstone bridge (Q_6)

respectively. Thus in case of quasi symmetric Wheatstone bridge detector the best combination is that of sample Q_4. While for other samples the transient response trace was severely affected with temperature though the responsivity was higher. The time constant of the transient response of sample Q_4 at room temperature was 159 sec for rise trace, 101 sec for slow decay and 23 sec

for fast decay. At 60^0C and 90^0C, the time constant for the rise trace dropped to 88 sec and 49 sec, respectively. The corresponding time constant for slow and fast decay at 60^0C was 83 sec and 17 sec. and at 90^0C it was 64 sec and 11sec.

5.2.2 Response of Quasi-symmetric Wheatstone Bridge UV Detector for Different Wavelength

The wavelength dependence of the quasi-symmetric detector Q_4 was also examined using UV light of wavelength 270 nm, 310 nm, 355 nm and 365 nm. UV LED sources were used for obtaining wavelength corresponding to 270 nm, 310 nm and 355 nm. The responsivity versus wavelength curve is shown in Figure 5-8. The responsivity of the Q_4 detector increased with increasing wavelength.
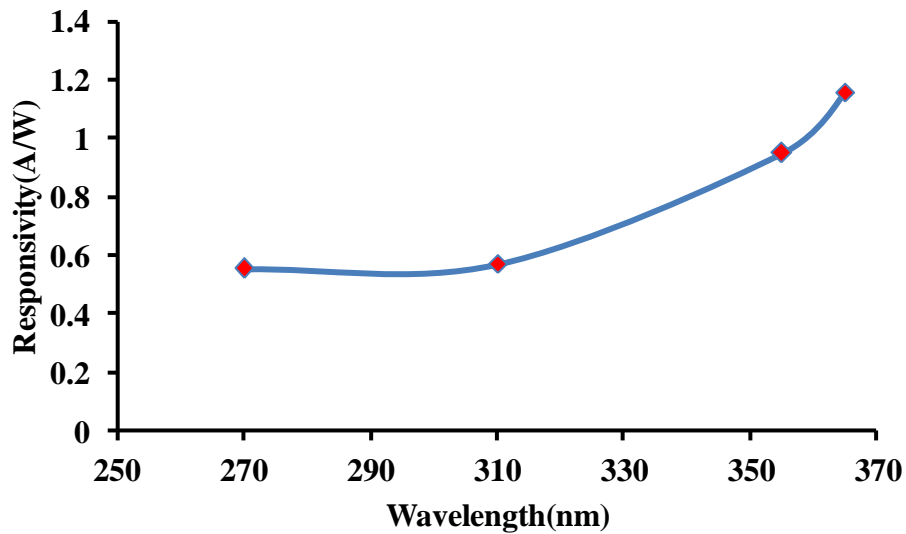
Figure 5-8   Response of quasi symmetric Wheatstone bridge (Q_4) for different wavelength

The responsivity of the detector for 365 nm was about 1.2 A/W. On decreasing the wavelength the responsivity dropped and it was about 0.6 A/W at 270 nm. The responsivity of the detector

dropped with decrease in wavelength because when wavelength decreased absorption of the light increased at the surface of the nanorods. The electron-hole pair generated near the surface is immediately annihilated due to large surface defects at the surface (**100-104**). Thus, the responsivity of the detector decreased with decreasing wavelength and the detector response was sensitive to wavelength.

5.2.3 Response of Quasi-symmetric Wheatstone Bridge UV Detector for Different Intensity

The response of the Q_4 detector for different light intensity corresponding to wavelength 365 nm was also determined. The current versus intensity graph is shown in Figure 5-9. The response of wavelength of UV light the detector increased with increasing intensity of UV light. The increase
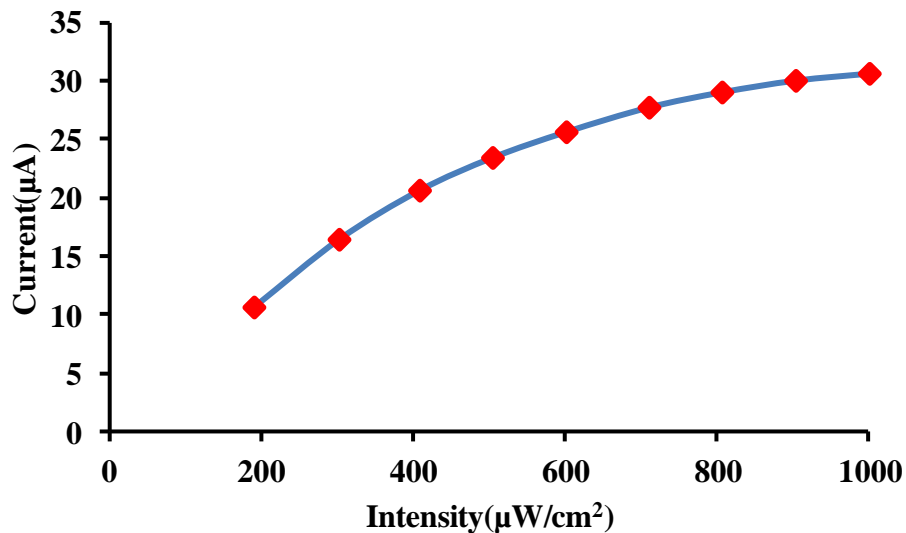
Figure 5-9   Response of quasi symmetric Wheatstone bridge(Q_4) for different intensity corresponding to wavelength 365 nm

in response was due to increase in the number of carriers generated with increase in intensity of the incident light. The current versus intensity graph showed exponential dependence. This can

be explained by considering the current through each quadrant of the detector. The Schottky current is governed by the Schottky diode equation for metal-semiconductor-metal structure (90, 105). Metal-Semiconductor-Metal structure (MSM) acts as two Schottky diodes connected back to back. When MSM is biased, one Schottky diode is forward biased and the other Schottky diode is reverse biased. The current through the MSM is given by

$$I = AA^*T^2 \exp\left(-\frac{q\text{Ø}_n}{KT}\right) \exp\left(\frac{q\Delta\text{Ø}_n}{KT}\right)\left(1 - \exp\left(-\frac{qV - IR}{nKT}\right)\right) \qquad \text{Eq } (5-21)$$

where A is the area of the interdigitated fingers, A^* is the Richardson constant, T is the absolute temperature, K Boltzmann constant, Ø_n is the barrier height, $\Delta\text{Ø}_n$ is the Schottky barrier lowering, V is the potential drop across the reverse bias Schottky junction, R is the series resistance, and n is the ideality factor.

The change in barrier height $\Delta\text{Ø}_n$ is given by,

$$\Delta\text{Ø}_n = \left[\frac{2q^3NV}{16\pi^2\varepsilon_s{}^3}\right]^{1/4} \qquad \text{Eq } (5-22)$$

where N is the electron carrier concentration, ε_s is the permittivity of ZnO seed layer, V is the potential drop across the reverse bias Schottky junction.

Comparing the different bridge configuration investigated here, qusai-symmetric whetstone bridge having Q_4 combination have near identical response for different temperature variations upto 90^0C. But the drawback of ZnO based detectors was that the response time is of several seconds. The response time of commercially available silicon based UV detectors have is in time

of the order of microseconds. But the responsivity of these silicon based diodes was only 0.01 to 0.2 A/W, while it's higher for quasi-symmetric (Q_4) ZnO based Wheatstone bridge about 0.8 A/W to 1 A/W. The response time of ZnO nanorod based detectors can be improved by using lateral grown ZnO rods **(7, 18, 93)**. Thus using quasi-symmetric bridge based detector in conjunction with lateral grown rods, detectors with high responsivity, temperature stability and lower response time could be achieved.

6. CONCLUSION AND FUTURE WORK

6.1 CONCLUSION

The goal of this research work was to fabricate a ZnO based UV detector that is operational at room temperature and above. The detector was fabricated to operate in Wheatstone bridge mode, so that the effects of changes in ambient conditions can be negated. Prior to the fabrication of the Wheatstone bridge based detector, the ZnO rod growth conditions were optimized, the dependence of detector response on the dimension of the electrodes, dimension of the rods, thickness of the seed layer and crystallinity of the rods and seed layer was studied. Based on these studies, the optimized conditions for the fabrication of the Wheatstone bridge were determined. The Wheatstone bridge was fabricated in three different configurations such as symmetric, asymmetric and quasi-symmetric. The transient response of these different types of Wheatstone bridge configurations at different temperatures above the room temperature was measured and compared with a conventional MSM UV detector.

In summary the following are the contributions of this dissertation research for the first time

- ➢ The rod growth conditions were optimized to grow rods of smaller diameters ranging from 20-60 nm.
- ➢ Studies on the response dependence of UV detector on electrode dimension showed that responsivity increases with increasing area of the interdigitated fingers and decreasing spacing between interdigitated fingers.
- ➢ Studies on the response dependence of UV detector on rod dimension showed that responsivity increases with increasing length of the rod and decreasing rod diameter.

➢ The relation of responsivity of the UV detector to number of times the ZnO seed layer was spin coated and spin speed at which the ZnO seed layer is coated was studied. The study showed that responsivity increases with increasing number of times the seed layer is coated and decreasing spin speed of seed layer coating.

➢ The dependence of responsivity of UV detector on crystallinity of seed layer and rod showed that the though the responsivity increases initially with annealing, but at higher annealing temperatures it decreases.

➢ The stability of detector at different temperatures was examined for conventional UV detector and UV detector in Wheatstone bridge configuration. The Wheatstone bridge configurations that were fabricated are symmetric, asymmetric, and quasi-symmetric. It was found the transient response of the quasi-symmetric Wheatstone bridge at different temperatures was better compared to those of the other Wheatstone bridge configurations and the conventional MSM UV detector.

➢ The responsivity of quasi-symmetric Wheatstone bridge is approximately 1 A/W. The responsivity of quasi-symmetric Wheatstone bridge is small compared to those of the symmetric, asymmetric, and conventional MSM UV detectors. However, the response of the quasi-symmetric Wheatstone bridge is still better than the commercially available detector having responsivity of only about 0.1A/W.

➢ The responsivity quasi-symmetric Wheatstone bridge is higher than commercial detectors. However, the drawback is that the response time of quasi-symmetric Wheatstone bridge is of the order of seconds, while that of commercially available detectors are of the order of microseconds. If the quasi-symmetric Wheatstone bridge has

to compete with current commercially available detectors, then the response time should

be brought down from seconds to microseconds.

➢ The studies on the quasi-symmetric Wheatstone bridge UV detector lead to a proposed

improved design with the ZnO rods oriented parallel to the substrate instead of oriented

vertical to the substrate.

6.2   FUTURE WORK

The slow response of the quasi-symmetric Wheatstone bridge detector is due to the vertical

orientation of the rods and the separation of the electrons from optically generated electron-hole

pair by recombination of the holes with the adsorbed oxygen on the surface of the nanorods.
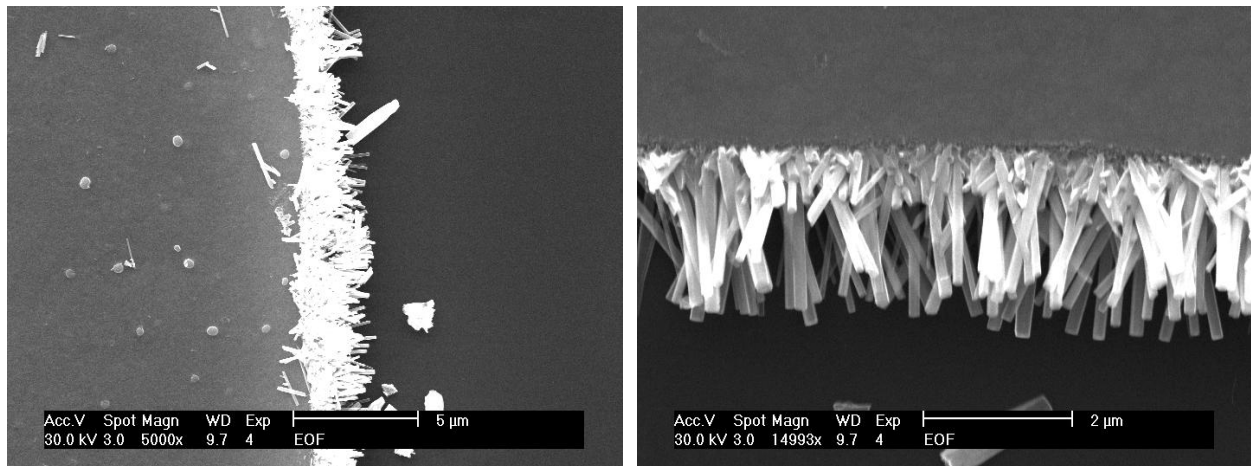
Figure 6-1   Growth of zinc oxide nanorods growth parallel to the substrate

When the rods are oriented vertically, the flow of the generated carriers in the rods to the seed

layer is due to diffusion drift associated with difference in carrier concentration. The response

time of the detector can be improved if the flow of the electron from the rods to the seed layer is

by voltage drift rather than diffusion drift and the electron separation from the optically

generated electron-hole pair is voltage assisted rater than the hole-oxygen recombination. The drift of the electrons from the rods to the seed layer and the separation of the electron-hole pairs can be voltage assisted if the rods are aligned parallel to the substrate. Various researchers have grown ZnO rods oriented horizontally for various applications. Figure 6-1 shows the growth of ZnO rods parallel to the substrate. A UV detector with less response time and a stable response (<25 % change) at different temperatures can be achieved by a combination of horizontally grown ZnO nanorods   and quasi symmetric Wheatstone bridge configuration. The conceptualized design of the quasi-symmetric Wheatstone bridge with horizontally grown nanorods is shown in Figure 6-2. Here for growing rods of different length along the opposite diagonals, the interdigitated spacing of the electrodes along the opposite diagonals should be accordingly spaced. This design might give faster and stable UV response even at higher temeperatue.
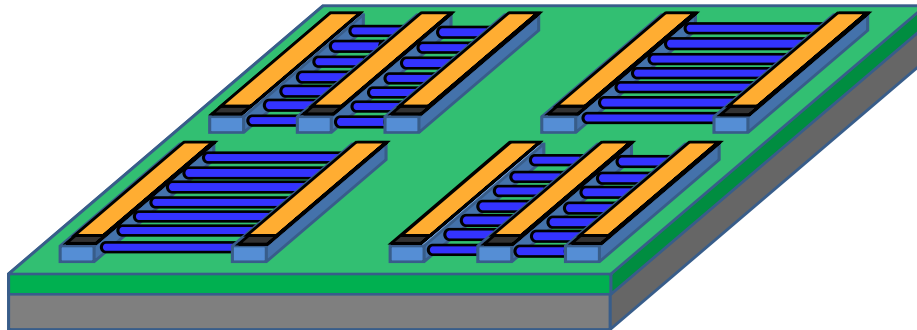
Figure 6-2   Structure of quasi-symmetric Wheatstone bridge with lateral grown zinc oxide nanorods

REFERENCES

1. Luo, L., Zhang, Y., Mao, S.S. & Lin, L. 2006, "Fabrication and characterization of ZnO nanowires based UV photodiodes", *Sensors and Actuators A: Physical,* vol. 127, no. 2, pp. 201-206.

2. Monroy, E., Omnes, F. & Calle, F. 2003, "Wide-bandgap semiconductor ultraviolet photodetectors", *Semiconductor Science and Technology,* vol. 18, no. 4, pp. R33.

3. Cheng, J., Zhang, Y. & Guo, R. 2008, "ZnO microtube ultraviolet detectors", *Journal of Crystal Growth,* vol. 310, no. 1, pp. 57-61.

4. Masuoka, F., Ooba, K., Sasaki, H., Endo, H., Chiba, S., Maeda, K., Yoneyama, H., Niikura, I. & Kashiwaba, Y. 2006, "Applicability of ZnO single crystals for ultraviolet sensors", *physica status solidi (c),* vol. 3, no. 4, pp. 1238-1241.

5. Cui, H., Zayat, M., Parejo, P.G. & Levy, D. 2007, "Highly Efficient Inorganic Transparent UV- Protective Thin-Film Coating by Low Temperature Sol-Gel Procedure for Application on Heat-Sensitive Substrates", *Advanced Materials,* vol. 20, no. 1, pp. 65-68.

6. Wiza, J.L. 1979, "Microchannel plate detectors", *Nucl.Instrum.Methods,* vol. 162, no. 1-3, pp. 587-601.

7. Jin, Y., Wang, J., Sun, B., Blakesley, J.C. & Greenham, N.C. 2008, "Solution-processed ultraviolet photodetectors based on colloidal ZnO nanoparticles", *Nano letters,* vol. 8, no. 6, pp. 1649-1653.

8. Jandow, N., Hassan, H.A., Yam, F. & Ibrahim, K. "ZnO Metal-Semiconductor-Metal UV Photodetectors on PPC Plastic with Various Metal Contacts", .

9. Razeghi, M. & Rogalski, A. 1996, "Semiconductor ultraviolet detectors", *Journal of Applied Physics,* vol. 79, no. 10, pp. 7433-7473.

10. Goldberg, Y.A. 1999, "Semiconductor near-ultraviolet photoelectronics", *Semiconductor science and technology,* vol. 14, no. 7, pp. R41.

11. Morkoc, H., Strite, S., Gao, G., Lin, M., Sverdlov, B. & Burns, M. 1994, "Large- band- gap SiC, III- V nitride, and II- VI ZnSe- based semiconductor device technologies", *Journal of Applied Physics,* vol. 76, no. 3, pp. 1363-1398.

12. Asif Khan, M., Shatalov, M., Maruska, H., Wang, H. & Kuokstis, E. 2005, "III-nitride UV devices", *Japanese journal of applied physics,* vol. 44, pp. 7191.

13. Chen, C., Chang, S., Su, Y., Chi, G., Chi, J., Chang, C., Sheu, J. & Chen, J. 2001, "GaN metal-semiconductor-metal ultraviolet photodetectors with transparent indium-tin-oxide Schottky contacts", *Photonics Technology Letters, IEEE,* vol. 13, no. 8, pp. 848-850.

14. Liang, S., Sheng, H., Liu, Y., Huo, Z., Lu, Y. & Shen, H. 2001, "ZnO Schottky ultraviolet photodetectors", *Journal of Crystal Growth,* vol. 225, no. 2, pp. 110-113.

15. Chiou, Y. & Tang, J. 2004, "GaN photodetectors with transparent indium tin oxide electrodes", *Japanese journal of applied physics,* vol. 43, pp. 4146.

16. Look, D.C., Reynolds, D., Hemsky, J.W., Jones, R. & Sizelove, J. 1999, "Production and annealing of electron irradiation damage in ZnO", *Applied Physics Letters,* vol. 75, no. 6, pp. 811-813.

17. Hickernell, F.S. 1976, "Zinc-oxide thin-film surface-wave transducers", *Proceedings of the IEEE,* vol. 64, no. 5, pp. 631-635.

18. Jin, B., Woo, H., Im, S., Bae, S. & Lee, S. 2001, "Relationship between photoluminescence and electrical properties of ZnO thin films grown by pulsed laser deposition", *Applied Surface Science,* vol. 169, pp. 521-524.

19. Craciun, V., Elders, J., Gardeniers, J. & Boyd, I.W. 1994, "Characteristics of high quality ZnO thin films deposited by pulsed laser deposition", *Applied Physics Letters,* vol. 65, no. 23, pp. 2963-2965.

20. Ghosh, R., Basak, D. & Fujihara, S. 2004, "Effect of substrate-induced strain on the structural, electrical, and optical properties of polycrystalline ZnO thin films", *Journal of Applied Physics,* vol. 96, no. 5, pp. 2689-2692.

21. Sans, J., Segura, A., Mollar, M. & Marí, B. 2004, "Optical properties of thin films of ZnO prepared by pulsed laser deposition", *Thin Solid Films,* vol. 453, pp. 251-255.

22. Kiriakidis, G., Suchea, M., Christoulakis, S., Horvath, P., Kitsopoulos, T. & Stoemenos, J. 2007, "Structural characterization of ZnO thin films deposited by dc magnetron sputtering", *Thin Solid Films,* vol. 515, no. 24, pp. 8577-8581.

23. Tsai, H. 2007, "Characteristics of ZnO thin film deposited by ion beam sputter", *Journal of Materials Processing Technology,* vol. 192, pp. 55-59.

24. Wang, Q.J., Pflugl, C., Andress, W.F., Ham, D., Capasso, F. & Yamanishi, M. 2008, "Gigahertz surface acoustic wave generation on ZnO thin films deposited by radio frequency magnetron sputtering on III-V semiconductor substrates", *Journal of Vacuum Science & Technology B: Microelectronics and Nanometer Structures,* vol. 26, no. 6, pp. 1848-1851.

25. Ianno, N., McConville, L., Shaikh, N., Pittal, S. & Snyder, P. 1992, "Characterization of pulsed laser deposited zinc oxide", *Thin Solid Films,* vol. 220, no. 1, pp. 92-99.

26. Shan, F., Shin, B., Jang, S. & Yu, Y. 2004, "Substrate effects of ZnO thin films prepared by PLD technique", *Journal of the European Ceramic Society,* vol. 24, no. 6, pp. 1015-1018.

27. Lu, Y.M., Tsai, S.Y., Lu, J.J. & Hon, M.H. 2007, "The structural and optical properties of zinc oxide thin films deposited on PET substrate by rf magnetron sputtering", *Solid State Phenomena,* vol. 121, pp. 971-974.

28. Koch, U., Fojtik, A., Weller, H. & Henglein, A. 1985, "Photochemistry of semiconductor colloids. Preparation of extremely small ZnO particles, fluorescence phenomena and size quantization effects", *Chemical physics letters,* vol. 122, no. 5, pp. 507-510.

29. Paul, G., Bhaumik, A., Patra, A. & Bera, S. 2007, "Enhanced photo-electric response of ZnO/polyaniline layer-by-layer self-assembled films", *Materials Chemistry and Physics,* vol. 106, no. 2, pp. 360-363.

30. Liu, Y., Yuan, Y., Gao, X., Yan, S., Cao, X. & Wei, G. 2007, "Deposition of ZnO thin film on polytetrafluoroethylene substrate by the magnetron sputtering method", *Materials Letters,* vol. 61, no. 23, pp. 4463-4465.

31. Ma, C., Taya, M. & Xu, C. 2008, "Flexible electrochromic device based on poly (3, 4-(2, 2-dimethylpropylenedioxy) thiophene)", *Electrochimica Acta,* vol. 54, no. 2, pp. 598-605.

32. Brabec, C.J., Sariciftci, N.S. & Hummelen, J.C. 2001, "Plastic solar cells", *Advanced Functional Materials,* vol. 11, no. 1, pp. 15-26.

33. Auret, F., Goodman, S., Hayes, M., Legodi, M., Van Laarhoven, H. & Look, D. 2001, "Electrical characterization of 1.8 MeV proton-bombarded ZnO", *Applied Physics Letters,* vol. 79, no. 19, pp. 3074-3076.

34. Chen, Y., Bagnall, D., Koh, H., Park, K., Hiraga, K., Zhu, Z. & Yao, T. 1998, "Plasma assisted molecular beam epitaxy of ZnO on c-plane sapphire: Growth and characterization", *Journal of Applied Physics,* vol. 84, no. 7, pp. 3912-3918.

35. Ohtomo, A., Kawasaki, M., Sakurai, Y., Ohkubo, I., Shiroki, R., Yoshida, Y., Yasuda, T., Segawa, Y. & Koinuma, H. 1998, "Fabrication of alloys and superlattices based on ZnO towards ultraviolet laser", *Materials Science and Engineering: B,* vol. 56, no. 2, pp. 263-266.

36. Hullavarad, S., Hullavarad, N., Karulkar, P., Luykx, A. & Valdivia, P. 2007, "Ultra violet sensors based on nanostructured ZnO spheres in network of nanowires: a novel approach", *Nanoscale Research Letters,* vol. 2, no. 3, pp. 161-167.

37. Ma, T., Guo, M., Zhang, M., Zhang, Y. & Wang, X. 2007, "Density-controlled hydrothermal growth of well-aligned ZnO nanorod arrays", *Nanotechnology,* vol. 18, no. 3, pp. 035605.

38. Ozgur, U., Alivov, Y.I., Liu, C., Teke, A., Reshchikov, M., Dogan, S., Avrutin, V., Cho, S. & Morkoc, H. 2005, "A comprehensive review of ZnO materials and devices", *Journal of Applied Physics,* vol. 98, no. 4, pp. 041301-041301-103.

39. Liu, Y., Gorla, C., Liang, S., Emanetoglu, N., Lu, Y., Shen, H. & Wraback, M. 2000, "Ultraviolet detectors based on epitaxial ZnO films grown by MOCVD", *Journal of Electronic Materials,* vol. 29, no. 1, pp. 69-74.

40. Bi, Z., Yang, X., Zhang, J., Bian, X., Wang, D., Zhang, X. & Hou, X. 2009, "A Back-Illuminated Vertical-Structure Ultraviolet Photodetector Based on an RF-Sputtered ZnO Film", *Journal of Electronic Materials,* vol. 38, no. 4, pp. 609-612.

41. Mandalapu, L., Xiu, F., Yang, Z. & Liu, J. 2007, "Ultraviolet photoconductive detectors based on Ga-doped ZnO films grown by molecular-beam epitaxy", *Solid-state electronics,* vol. 51, no. 7, pp. 1014-1017.

42. Basak, D., Amin, G., Mallik, B., Paul, G. & Sen, S. 2003, "Photoconductive UV detectors on sol–gel-synthesized ZnO films", *Journal of Crystal Growth,* vol. 256, no. 1, pp. 73-77.

43. Fabricius, H., Skettrup, T. & Bisgaard, P. 1986, "Ultraviolet detectors in thin sputtered ZnO films", *Applied Optics,* vol. 25, no. 16, pp. 2764-2767.

44. Oh, D., Suzuki, T., Hanada, T., Yao, T., Makino, H. & Ko, H. 2006, "Photoresponsivity of ZnO Schottky barrier diodes", *Journal of Vacuum Science & Technology B: Microelectronics and Nanometer Structures,* vol. 24, no. 3, pp. 1595-1598.

45. Endo, H., Sugibuchi, M., Takahashi, K., Goto, S., Sugimura, S., Hane, K. & Kashiwaba, Y. 2007, "Schottky ultraviolet photodiode using a ZnO hydrothermally grown single crystal substrate", *Applied Physics Letters,* vol. 90, no. 12, pp. 121906-121906-3.

46. Nakano, M., Makino, T., Tsukazaki, A., Ueno, K., Ohtomo, A., Fukumura, T., Yuji, H., Akasaka, S., Tamura, K. & Nakahara, K. 2008, "Transparent polymer Schottky contact for a high performance visible-blind ultraviolet photodiode based on ZnO", *Applied Physics Letters,* vol. 93, pp. 123309.

47. Moon, T., Jeong, M., Lee, W. & Myoung, J. 2005, "The fabrication and characterization of ZnO UV detector", *Applied Surface Science,* vol. 240, no. 1, pp. 280-285.

48. Ryu, Y., Lee, T., Lubguban, J., White, H., Park, Y. & Youn, C. 2005, "ZnO devices: Photodiodes and p-type field-effect transistors", *Applied Physics Letters,* vol. 87, no. 15, pp. 153504-153504-3.

49. Lopatiuk-Tirpak, O., Chernyak, L., Mandalapu, L., Yang, Z., Liu, J., Gartsman, K., Feldman, Y. & Dashevsky, Z. 2006, "Influence of electron injection on the photoresponse of ZnO homojunction diodes", *Applied Physics Letters,* vol. 89, no. 14, pp. 142114-142114-3.

50. Lin, T., Chang, S., Su, Y., Huang, B., Fujita, M. & Horikoshi, Y. 2005, "ZnO MSM photodetectors with Ru contact electrodes", *Journal of Crystal Growth,* vol. 281, no. 2, pp. 513-517.

51. Ji, L., Wu, C., Lin, C., Meen, T., Lam, K., Peng, S., Young, S. & Liu, C. 2010, "Characteristic Improvements of ZnO-Based Metal-Semiconductor-Metal Photodetector on Flexible Substrate with ZnO Cap Layer", *Japanese Journal of Applied Physics,* vol. 49, no. 5, pp. 2201.

52. Shan, C., Zhang, J., Yao, B., Shen, D., Fan, X. & Choy, K. 2009, "Ultraviolet photodetector fabricated from atomic-layer-deposited ZnO films", *Journal of Vacuum Science & Technology B: Microelectronics and Nanometer Structures,* vol. 27, no. 3, pp. 1765-1768.

53. Li, M., Chokshi, N., DeLeon, R.L., Tompa, G. & Anderson, W.A. 2007, "Radio frequency sputtered zinc oxide thin films with application to metal–semiconductor–metal photodetectors", *Thin Solid Films,* vol. 515, no. 18, pp. 7357-7363.

54. Li, M., Anderson, W., Chokshi, N., DeLeon, R.L. & Tompa, G. 2006, "Laser annealing of laser assisted molecular beam deposited ZnO thin films with application to metal-semiconductor-metal photodetectors", *Journal of Applied Physics,* vol. 100, no. 5, pp. 053106-053106-4.

55. Jiang, D., Zhang, J., Lu, Y., Liu, K., Zhao, D., Zhang, Z., Shen, D. & Fan, X. 2008, "Ultraviolet Schottky detector based on epitaxial ZnO thin film", *Solid-State Electronics,* vol. 52, no. 5, pp. 679-682.

56. Liu, C., Zhang, B., Lu, Z., Binh, N., Wakatsuki, K., Segawa, Y. & Mu, R. 2009, "Fabrication and characterization of ZnO film based UV photodetector", *Journal of Materials Science: Materials in Electronics,* vol. 20, no. 3, pp. 197-201.

57. Ji, L., Peng, S., Su, Y., Young, S., Wu, C. & Cheng, W. 2009, "Ultraviolet photodetectors based on selectively grown ZnO nanorod arrays", *Applied Physics Letters,* vol. 94, no. 20, pp. 203106-203106-3.

58. Bube, R.H. 1992, *Photoelectronic properties of semiconductors,* Cambridge University Press.

59. Rose, A. 1978, *Concepts in photoconductivity and allied problems,* Krieger New York.

60. Jie, J., Zhang, W., Jiang, Y., Meng, X., Li, Y. & Lee, S. 2006, "Photoconductive characteristics of single-crystal CdS nanoribbons", *Nano letters,* vol. 6, no. 9, pp. 1887-1892.

61. Jeong, I., Kim, J.H. & Im, S. 2003, "Ultraviolet-enhanced photodiode employing n-ZnO/p-Si structure", *Applied Physics Letters,* vol. 83, no. 14, pp. 2946-2948.

62. Mridha, S. & Basak, D. 2007, "Ultraviolet and visible photoresponse properties of n-Zn/p-Si heterojunction", *Journal of Applied Physics,* vol. 101, no. 8, pp. 083102-083102-5.

63. Chen, T., Young, S., Chang, S., Hsiao, C. & Wu, S. 2013, "Photoelectrical and Low-Frequency Noise Characteristics of ZnO Nanorod Photodetectors Prepared on Flexible Substrate", .

64. Chai, G., Lupan, O., Chow, L. & Heinrich, H. 2009, "Crossed zinc oxide nanorods for ultraviolet radiation detection", *Sensors and Actuators A: Physical,* vol. 150, no. 2, pp. 184-187.

65. Soci, C., Zhang, A., Xiang, B., Dayeh, S.A., Aplin, D., Park, J., Bao, X., Lo, Y. & Wang, D. 2007, "ZnO nanowire UV photodetectors with high internal gain", *Nano Letters,* vol. 7, no. 4, pp. 1003-1009.

66. Vasudevan, A., Jung, S. & Ji, T. 2012, "On the Responsivity of UV Detectors Based on Selectively Grown ZnO Nanorods", *Sensors Journal, IEEE,* vol. 12, no. 5, pp. 1317-1325.

67. Thomas, D. 1960, "The exciton spectrum of zinc oxide", *Journal of Physics and Chemistry of Solids,* vol. 15, no. 1, pp. 86-96.

68. Huang, M.H., Wu, Y., Feick, H., Tran, N., Weber, E. & Yang, P. 2001, "Catalytic growth of zinc oxide nanowires by vapor transport", *Advanced Materials,* vol. 13, no. 2, pp. 113-116.

69. Wang, Z.L. 2000, "Characterizing the structure and properties of individual wire-like nanoentities", *Advanced Materials,* vol. 12, no. 17, pp. 1295-1298.

70. Wang, Z.L. 2004, "Nanostructures of zinc oxide", *Materials today,* vol. 7, no. 6, pp. 26-33.

71. Park, J., Choi, H., Choi, Y., Sohn, S. & Park, J. 2004, "Ultrawide ZnO nanosheets", *Journal of Materials Chemistry,* vol. 14, no. 1, pp. 35-36.

72. Park, J., Choi, H. & Park, J. 2004, "Scaffolding and filling process: a new type of 2D crystal growth", *Journal of Crystal Growth,* vol. 263, no. 1, pp. 237-242.

73. Keem, K., Kim, H., Kim, G., Lee, J.S., Min, B., Cho, K., Sung, M. & Kim, S. 2004, "Photocurrent in ZnO nanowires grown from Au electrodes", *Applied Physics Letters,* vol. 84, no. 22, pp. 4376-4378.

74. Arnold, M.S., Avouris, P., Pan, Z.W. & Wang, Z.L. 2003, "Field-effect transistors based on single semiconducting oxide nanobelts", *The Journal of Physical Chemistry B,* vol. 107, no. 3, pp. 659-663.

75. Lee, C., Lee, T., Lyu, S., Zhang, Y., Ruh, H. & Lee, H. 2002, "Field emission from well-aligned zinc oxide nanowires grown at low temperature", *Applied Physics Letters,* vol. 81, no. 19, pp. 3648-3650.

76. Park, W.I., Kim, D.H., Jung, S. & Yi, G. 2002, "Metalorganic vapor-phase epitaxial growth of vertically well-aligned ZnO nanorods", *Applied Physics Letters,* vol. 80, pp. 4232.

77. Xu, C., Xu, G., Liu, Y. & Wang, G. 2002, "A simple and novel route for the preparation of ZnO nanorods", *Solid State Communications,* vol. 122, no. 3, pp. 175-179.

78. Wang, Y., Zhang, L., Wang, G., Peng, X., Chu, Z. & Liang, C. 2002, "Catalytic growth of semiconducting zinc oxide nanowires and their photoluminescence properties", *Journal of Crystal Growth,* vol. 234, no. 1, pp. 171-175.

79. Yang, P., Yan, H., Mao, S., Russo, R., Johnson, J., Saykally, R., Morris, N., Pham, J., He, R. & Choi, H. 2002, "Controlled growth of ZnO nanowires and their optical properties", *Advanced Functional Materials,* vol. 12, no. 5, pp. 323.

80. Yao, B., Chan, Y. & Wang, N. 2002, "Formation of ZnO nanostructures by a simple way of thermal evaporation", *Applied Physics Letters,* vol. 81, no. 4, pp. 757-759.

81. Greene, L.E., Yuhas, B.D., Law, M., Zitoun, D. & Yang, P. 2006, "Solution-grown zinc oxide nanowires", *Inorganic chemistry,* vol. 45, no. 19, pp. 7535-7543.

82. Vasudevan, A., Jung, S. & Ji, T. 2011, "Synthesis and Characterization of Hydrolysis Grown Zinc Oxide Nanorods", *ISRN Nanotechnology,* vol. 2011.

83. Onodera, A. & Takesada, M. 2012, "Electronic Ferroelectricity in II-VI Semiconductor ZnO", .

84. http://www.globalspec.com/reference/82039/203279/5-1-oxides (accessed on 06-012-13)

85. Sood, A.K., Zeller, J.W., Puri, Y.R., Dhar, N.K., Polla, D.L., Manzur, T., Wang, Z.L. & Anwar, A.M. 2011, "A review of growth and characterization of ZnO nanostructures for optoelectronic sensor and energy harvesting applications", *SPIE Optical Engineering Applications*International Society for Optics and Photonics, , pp. 815514.

86. Von Wenckstern, H., Müller, S., Biehne, G., Hochmuth, H., Lorenz, M. & Grundmann, M. 2010, "Dielectric passivation of ZnO-based Schottky diodes", *Journal of Electronic Materials,* vol. 39, no. 5, pp. 559-562.

87. Qiu, X., Tang, R., Zhu, J., Oiler, J., Yu, C., Wang, Z. & Yu, H. 2011, "The effects of temperature, relative humidity and reducing gases on the ultraviolet response of ZnO based film bulk acoustic-wave resonator", *Sensors and Actuators B: Chemical,* vol. 151, no. 2, pp. 360-364.

88. Rashid, T., Phan, D. & Chung, G. 2012, "Characteristics of UV sensors using ZnO nanostructures synthesized by galvanostatic electrochemical deposition", *Sensors, 2012 IEEE*IEEE, , pp. 1.

89. Panda, S. & Jacob, C. 2012, "Preparation of transparent ZnO thin films and their application in UV sensor devices", *Solid-State Electronics,* vol. 73, pp. 44-50.

90. Sze, S., Coleman, D. & Loya, A. 1971, "Current transport in metal-semiconductor-metal (MSM) structures", *Solid-State Electronics,* vol. 14, no. 12, pp. 1209-1218.

91. Ghasempour Ardakani, A., Pazoki, M., Mahdavi, S.M., Bahrampour, A.R. & Taghavinia, N. 2012, "Ultraviolet photodetectors based on ZnO sheets: the effect of sheet size on photoresponse properties", *Applied Surface Science,* vol. 258, no. 14, pp. 5405-5411.

92. Su, Y., Peng, S., Ji, L., Wu, C., Cheng, W. & Liu, C. 2009, "Ultraviolet ZnO nanorod photosensors", *Langmuir,* vol. 26, no. 1, pp. 603-606.

93. Liu, N., Fang, G., Zeng, W., Zhou, H., Cheng, F., Zheng, Q., Yuan, L., Zou, X. & Zhao, X. 2010, "Direct growth of lateral ZnO nanorod UV photodetectors with Schottky contact by a single-step hydrothermal reaction", *ACS Applied Materials & Interfaces,* vol. 2, no. 7, pp. 1973-1979.

94. Li, Q., Gao, T., Wang, Y. & Wang, T. 2005, "Adsorption and desorption of oxygen probed from ZnO nanowire films by photocurrent measurements", *Applied Physics Letters,* vol. 86, no. 12, pp. 123117-123117-3.

95. Reemts, J. & Kittel, A. 2007, "Persistent photoconductivity in highly porous ZnO films", *Journal of Applied Physics,* vol. 101, no. 1, pp. 013709-013709-5.

96. Darling, R.B. 1991, "Defect-state occupation, Fermi-level pinning, and illumination effects on free semiconductor surfaces", *Physical Review B,* vol. 43, no. 5, pp. 4071.

97. Ul Hasan, K., Alvi, N., Lu, J., Nur, O. & Willander, M. 2011, "Single nanowire-based UV photodetectors for fast switching", *Nanoscale research letters,* vol. 6, no. 1, pp. 1-6.

98. Prades, J.D., Hernández-Ramírez, F., Jimenez-Diaz, R., Manzanares, M., Andreu, T., Cirera, A., Romano-Rodriguez, A. & Morante, J. 2008, "The effects of electron–hole separation on the photoconductivity of individual metal oxide nanowires", *Nanotechnology,* vol. 19, no. 46, pp. 465501.

99. Mamat, M.H., Khusaimi, Z., Zahidi, M.M. & Mahmood, M.R. "ZnO Nanorod Arrays Synthesised Using Ultrasonic-Assisted Sol-Gel and Immersion Methods for Ultraviolet Photoconductive Sensor Applications", .

100. Young, S., Ji, L., Chang, S., Chen, Y., Lam, K., Liang, S., Du, X., Xue, Q. & Sun, Y. 2007, "ZnO metal–semiconductor–metal ultraviolet photodetectors with Iridium contact electrodes", *IET optoelectronics,* vol. 1, no. 3, pp. 135-139.

101. Young, S., Ji, L., Chang, S. & Su, Y. 2006, "ZnO metal–semiconductor–metal ultraviolet sensors with various contact electrodes", *Journal of Crystal Growth,* vol. 293, no. 1, pp. 43-47.

102. Jandow, N., Yam, F., Thahab, S., Abu Hassan, H. & Ibrahim, K. 2010, "Characteristics of ZnO MSM UV photodetector with Ni contact electrodes on poly propylene carbonate (PPC) plastic substrate", *Current Applied Physics,* vol. 10, no. 6, pp. 1452-1455.

103. Yan, F., Xin, X., Aslam, S., Zhao, Y., Franz, D., Zhao, J.H. & Weiner, M. 2004, "4H-SiC UV photo detectors with large area and very high specific detectivity", *Quantum Electronics, IEEE Journal of,* vol. 40, no. 9, pp. 1315-1320.

104. Hassan, N., Hashim, M. & Allam, N.K. 2013, "Low power UV photodetection characteristics of cross-linked ZnO nanorods/nanotetrapods grown on silicon chip", *Sensors and Actuators A: Physical,* vol. 192, pp. 124-129.

105. Mehrabian, M., Azimirad, R., Mirabbaszadeh, K., Afarideh, H. & Davoudian, M. 2011, "UV detecting properties of hydrothermal synthesized ZnO nanorods", *Physica E: Low-dimensional Systems and Nanostructures,* vol. 43, no. 6, pp. 1141-1145.

106. Chao, Y., Chen, C., Lin, C. & He, J. 2011, "Light scattering by nanostructured anti-reflection coatings", *Energy & Environmental Science,* vol. 4, no. 9, pp. 3436-3441.

107. Bekeny, C., Voss, T., Hilker, B., Gutowski, J., Hauschild, R., Kalt, H., Postels, B., Bakin, A. & Waag, A. 2007, "Influence of ZnO seed crystals and annealing on the optical quality of low-temperature grown ZnO nanorods", *Journal of Applied Physics,* vol. 102, no. 4, pp. 044908-044908-5.

108. Yang, L., Zhao, Q., Willander, M., Yang, J. & Ivanov, I. 2009, "Annealing effects on optical properties of low temperature grown ZnO nanorod arrays", *Journal of Applied Physics,* vol. 105, no. 5, pp. 053503-053503-7.

109. Liu, S., Chen, T., Wan, J., Ru, G., Li, B. & Qu, X. 2009, "The effect of pre-annealing of sputtered ZnO seed layers on growth of ZnO nanorods through a hydrothermal method", *Applied Physics A,* vol. 94, no. 4, pp. 775-780.

110. Ma, T., Guo, M., Zhang, M., Zhang, Y. & Wang, X. 2007, "Density-controlled hydrothermal growth of well-aligned ZnO nanorod arrays", *Nanotechnology,* vol. 18, no. 3, pp. 035605.

111. Endo, H., Sugibuchi, M., Takahashi, K., Goto, S., Sugimura, S., Hane, K. & Kashiwaba, Y. 2007, "Schottky ultraviolet photodiode using a ZnO hydrothermally grown single crystal substrate", *Applied Physics Letters,* vol. 90, no. 12, pp. 121906-121906-3.

112. Kester, W. & Devices, A. 1999, *Practical design techniques for sensor signal conditioning,* Analog Devices.

113. Wang, S., Song, C., Cheng, K., Dai, S., Zhang, Y. & Du, Z. 2012, "Controllable growth of ZnO nanorod arrays with different densities and their photoelectric properties", *Nanoscale research letters,* vol. 7, no. 1, pp. 1-7.

114. Liu, J., She, J., Deng, S., Chen, J. & Xu, N. 2008, "Ultrathin seed-layer for tuning density of ZnO nanowire arrays and their field emission characteristics", *The Journal of Physical Chemistry C,* vol. 112, no. 31, pp. 11685-11690.

APPENDICES

A: KNOW WHETHER THE SUN IS HOT OR COOL TODAY

The need to consult doctor for knowing your insulin level in blood has become a thing of the past. Insulin kits which are very cheap and available in a majority of stores allow us to determine the insulin level at home. With advancement in technology, the power vested upon oneself to know your body as well as your environment has improved. So, how do you feel about having a new gadget that can be incorporated into your watch or mobile phone which lets you keep track of the amount of UV rays from sun you are exposed. Who knows that someday this device might help in bringing down the number of skin cancer illness related to UV over exposure?

Researchers at the University of Arkansas have been working to build microsized UV detector to incorporate in portable devices like watch or mobile phone. Arun Vasudevan, Ph.D. student in Microelectronics-Photonics, is spearheading this work under the guidance of a former university of Arkansas Professor Dr. Taeksoo Ji and the current Director of High Density Electronic Center, Dr. Simon Ang.

"The lack of detectors that can measure the UV intensity in outerspace as well as survive the harsh environments of the outer space is the main trigger to embark on this work. The two main objectives attempted by this research work are to build a UV detector that can be resilient to the onslaught of high energy particles as well as high temperature in outer space and the UV detector should be portable and easy to manufacture," says Arun.

Though the first objective of the researchers might not have direct benefit for the common man, the second objective might have a great value for the mankind. This objective will help in the realization of UV detectors that can be easily incorporated in portable devices like watch and cellphones as well as the manufacturing techniques employed here makes it affordable.

Every material is made of three basic constituents namely electron, proton and neutron. The proton and neutron occupy the central portion of the atom and is collectively called the nucleus. The nucleus has a positive charge. Whereas the electron the third constituent of the atom, has negative charge and revolves around the nucleus due to attractive force with the positively charged nucleus. The electron being held by the positively charged nucleus can be pulled from the clutches of the nucleus by using heat energy or light energy. By counting the number of electrons pulled apart from the nucleus is an indirect measurement of the strength of the heat energy or light energy.

A material which is suitable to measure the strength of the incident UV light should have the ability to absorb the incident UV light and use this absorbed light energy to free the electrons from the nucleus. Electrons can also be freed by various sources of energy emanating from the ambient and these stray electrons are called noise. The electrons freed by the incident light can be distinguishable from the noise only if the number of electrons freed by the incident light is larger than the noise.

The number of electrons freed by the incident light can be enhanced by increasing the strength of the incident light. But the drawback is that if the strength of the incident light is very low then it is difficult to measure. The number of electrons freed by the incident light can be made higher than the noise even if the strength of the incident light is low if the area of available for interaction with the incident light can be enhanced.

This can be achieved by breaking down UV absorbing material into very small structures. The effectiveness of using smaller structures can be better visualized by comparing the lethality of a fully grown shark and pack of piranha fishes. Though a piranha fish is very small compared to
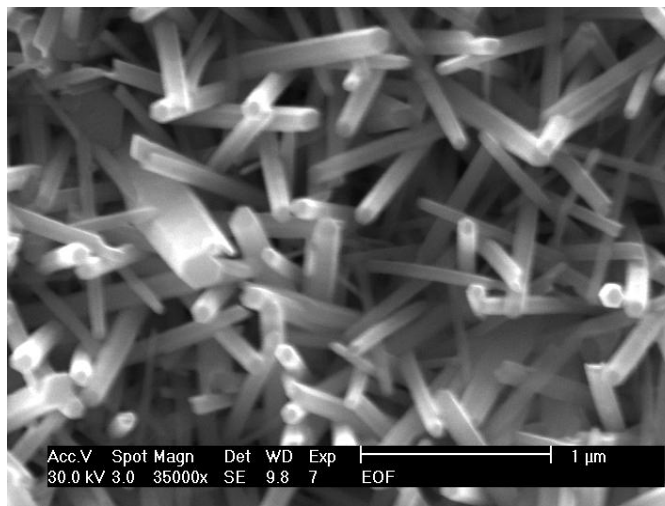
The near cylindrical small structures of zinc oxide material

fully grown shark, a pack of piranha fish can be more lethal than a shark. A similar technique is being employed here to build the detector. The detector being developed here uses UV absorbing cylindrical structures made of zinc oxide material whose size is about 1000 times smaller than the thickness of the human hair. These extremely small structures are grown by mixing special chemicals and then boiling at a temperature close to the boiling temperature of water. These extremely small structures are invisible to the naked eye and special equipments are required to see them. A pack of these structures assembled over a very small area can perform 10 times better than the current detectors. The current detectors available in market are bulky and not portable because they use additional equipment to enhance the strength of the incident low intense light and to decrease the noise.

In addition to employing smaller structures to improve the performance of the detector, the detector is designed such that the output signal of the detector is the difference of four near identical detectors. The reason for employing such a structure is that change in ambient conditions like temperature and pressure can affect the performance of the detector. By designing the detector output as the difference of four near identical detectors, the output will remain the

same irrespective of the changes in ambient conditions since all the four detectors performance are affected equally.
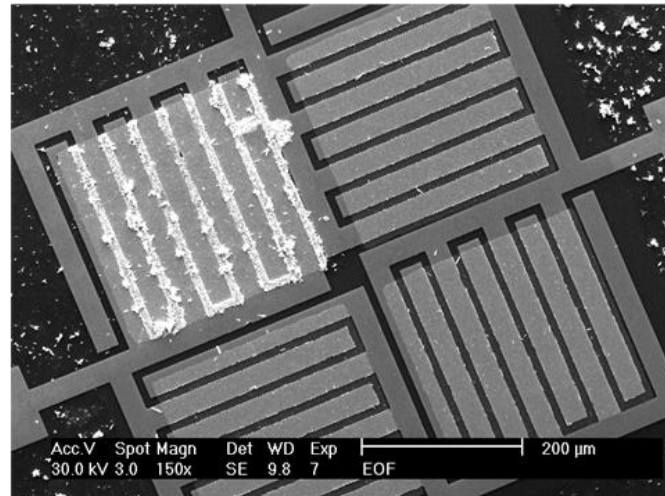
Microsized UV detector showing zinc oxide material in cylindrical structure grown only at one detector out of the four identical detectors. The zinc oxide structures can also be grown in the remaining three detectors.

The researchers working on this detector said "the detection ability of the new detector being developed here is better than the current detectors available in market but further research is needed to improve the time it takes to respond to the incident light". The researchers exuded confidence that they can soon overcome this minor glitch with the detector. Let's hope that it's just a matter of time before they overcome this glitch. We hope in near future before we step out into sun, our portable devices can speak whether the sun is hot or cool today!

B: EXCECUTIVE SUMMARY OF INTELLECTUAL PROPERTY

The major IP contributions of this work can be summarized as follows:

1. Effects on rod properties by varying the concentration of the chemicals used for the rod growth.

2. Effects of electrode dimensions, rod dimensions, seed layer thickness, crystallinity of the seed layer and rods on the UV response of ZnO based MSM detector.

3. Response stability of the Wheatstone bridge based detectors having symmetric, asymmetric and quasi-symmetric configuration at different temperatures.

4. Proposed quasi-symmetric Wheatstone bridge design with rod growth parallel to the substrate

C: POTENTIAL PATENT AND COMMERCIALIZATION

C.1   Potential Patent

Several authors have explored ZnO seed based MSM UV detectors prepared using different preparation techniques. Incorporation of ZnO rods in MSM UV detector for improving the performance was first reported by Ji et al **(57)**. The effects of ambient temperature on the response of the ZnO nanorod incorporated UV detector were not studied. This study reports the effects of change in ambient temperature on the response of the detector and how the variations in detector response due to changes in the ambient conditions (temperature) are reduced by operating the detector in Wheatstone bridge mode. ZnO based UV detectors reported here are configured in quasi-symmetric Wheatstone bridge. Though Wheatstone bridge principle based sensors have been reported in literature, this is for the first time the Wheatstone bridge principle

has been applied for a UV detector application. The detector fabricated here uses the Wheatstone bridge design in conjunction with selective growth of ZnO nanorods to form a quasi-symmetric Wheatstone bridge UV detector. The use of quasi-symmetric Wheatstone bridge design for sensors application have not been reported anywhere in literature nor any patents exist. The proposed quasi-symmetric Wheatstone bridge design with the rods grown parallel to the substrate for improving the response time of the UV detector is a newly developed design. Several authors have used rods grown parallel to the substrate for UV detector applications. The difference here is that the proposed structure for improving the response time of the detector is a combination of quasi-symmetric Wheatstone bridge and growth of rods parallel to the substrate.

Item 1: Cannot be patented because the data were already published in ISRN Nanotechnology Journal.

Item 2: Cannot be patented because the data were published in IEEE sensor Journal.

Item 3: Can be patented since the use of Wheatstone bridge for ZnO based UV detector has not been reported elsewhere.

Item 4: Can be patented because the combination of Wheatstone bridge and lateral growth of rods is a newly proposed design for UV detector.

C.2   Commercialization

Item 1: Cannot be commercialized because these are optimization studies for the growth of ZnO rods.

Item 2: Cannot be commercialized because these are optimization studies for the fabrication of UV detector.

Item 3: Cannot be commercialized because further studies are needed to decrease the response
time of the detector

Item 4: Can be commercialized if this design improves the response time of the detector. Since
this fabricated detector is of micro-sized and fabrication techniques employed are
feasible for large scale production.

D: BROADER IMPACT

The use of ZnO nanorods for the fabrication of the UV detector allows it to be used for other applications as well. The high isoelectric point and large surface area of ZnO nanorods improves enzyme loading and gas adsorption on the rod surface. Hence this detector can be used for biological as well as gas sensor applications.

One of the highlights of this detector is its portability. The self calibration ability of the detector eliminates the need for additional gadgets to maintain a constant operating temperature and the detector response is high even at room temperature. Also, there is no need for optical filters for blocking visible light. Hence, the detector developed here is compact. The fabrication techniques uses silicon integration technology, thereby, the incorporation into a wrist watch or other portable device is easier. The benefit of incorporation of this detector in portable devices is that it can be used to track the amount of UV light from the sun the human body is exposed. This can be a major step towards the prevention of cancer related illness from UV over exposure.

Rapid industrialization and lack of proper management of industrial waste has severely affected the earth atmosphere especially the thermosphere which contains the ozone layer. The ozone layer prevents harmful UV radiation from the sun reaching the earth surface. Damage to this layer will allow the harmful UV radiation to reach the earth surface, thereby, increasing the chances of cancer related illness and gene mutation. Since the detector fabricated here is portable and fabrication techniques adopted here makes it cheaper than the current detectors, large deployment of theses detectors over a wider area is easier and cheaper. This will allow the environmental monitoring agencies to keep better track of the ozone layer and as well recommend the necessary actions to prevent ozone layer damage.

E: RESEARCH PROJECT PLAN

#	Task Name	08 Qtr 3	2009 Qtr 1	Qtr 3	2010 Qtr 1	Qtr 3	2011 Qtr 1	Qtr 3	2012 Qtr 1	Qtr 3	2013 Qtr 1	Qtr 3
1	Project plan for ZnO nanorod based ultraviolet detectors with Wheatstone bridge design											
2	Literature review											
3	Growth of ZnO rods											
4	Optimization of the ZnO seed layer											
5	Variation in zinc acetate concentration (0.01 M to 0.1 M)											
6	Variation in ethanolamine concentration (0.05 M to 0.3 M)											
7	Charecterization (SEM and XRD)											
8	Optimization of the ZnO growth											
9	Variation in hexamethylenetetramine conc. (0.015 M, 0.02 M, 0.025 M, 0.03 M, and 0.035 M (horizontal orientation)											
10	Variation in hexamethylenetetramine conc. (0.015 M, 0.02 M, 0.025 M, 0.03 M, and 0.035 M (vertical orientation)											
11	Charecterization (SEM and XRD)											
12	Optimization of response of simple ZnO based MSM UV detector											
13	Fabrication											
14	Samples with different electrode dimension(L1, L2, L3, L4)											
15	Samples with different rod dimension (Growth time in hours- 4, 8, and 16)											
16	IV charecterizattion											
17	Transient response charecterization											

	Task Name	08	2009	2010	2011	2012	2013
		Qtr 3	Qtr 1 Qtr 3	Qtr 1 Qtr 3	Qtr 1 Qtr 3	Qtr 1 Qtr 3	Qtr 1 Qtr 3
18	⊟ **Symmetric Wheatstone bridge**						
19	Fabrication (rod growth time- 16 hours)						
20	Transient response charecterization						
21	⊟ **Assymetric Wheatstone bridge**						
22	Fabrication (rod growth time- 16 hours)						
23	Transient response charecterization						
24	⊟ **Quasi-symmetric Wheatstone bridge**						
25	Mask layout for quadrant masking						
26	Fabrication(growth time in hours, 0 - 4, 0 - 8, 0 - 16, 4 - 8, and 4 - 16)						
27	Transient response charecterization						
28	Response of the detector for different wavelength						
29	Response of the detector for different light intensity						
30	⊟ **Optimization of response of simple ZnO based MSM based UV detector**						
31	⊟ **Response dependence on the crystallinity of the seed layer**						
32	Fabrication(no. of seed layers, 1 - 5 and spin seed, 1000 - 5000 rpm)						
33	Response measurement						
34	⊟ **Response dependence on the crystallinity of the rods**						
35	Fabrication(seed annealing, 350 - 550 deg. Cel. and rod annealing, 100 - 250 deg. cel.)						
36	Response measurement						
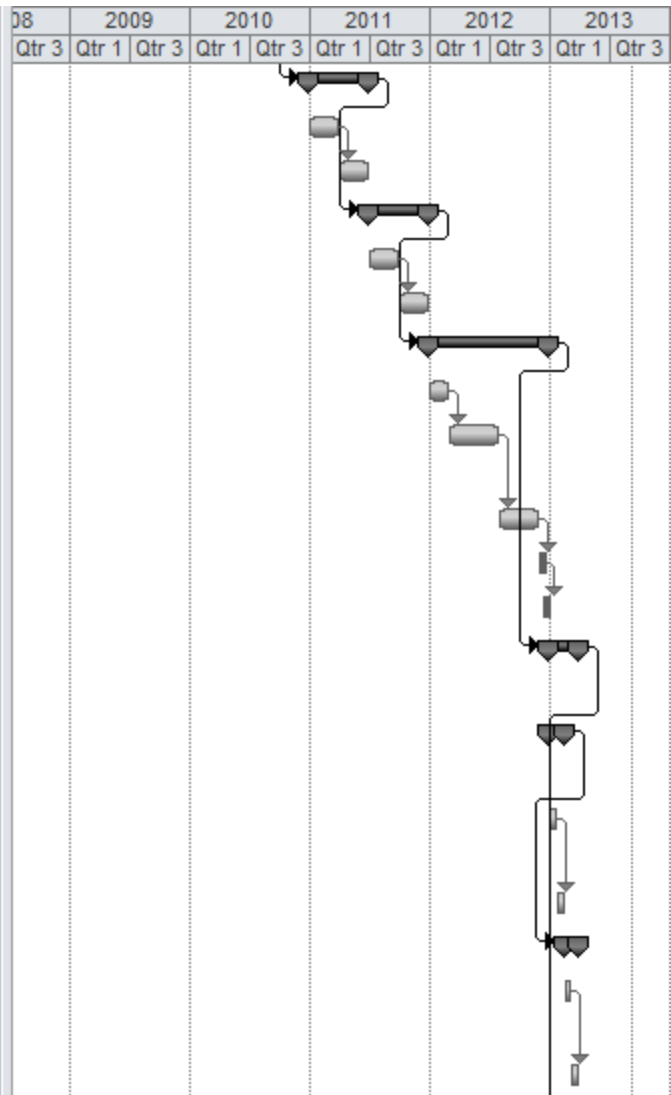
	Task Name	08	2009	2010	2011	2012	2013
		Qtr 3	Qtr 1	Qtr 3	Qtr 1	Qtr 3	Qtr 1	Qtr 3	Qtr 1	Qtr 3	Qtr 1	Qtr 3
37	**Dissertation**						
38	**Introduction (chapter- 1)**						
39	**Optimization of ZnO nanorod growth (chapter- 2)**						
40	Optimization of ZnO seed layer						
41	Optimization of ZnO nanorod growth						
42	**Optimization of the resposne of simple MSM UV detector (chapter- 3)**						
43	Response dependence on electrode dimension and rod dimension						
44	Response dependence on thickness of ZnO seed layer						
45	Response dependence on crystallinity of ZnO seeds and rods						
46	**Symmetric and assymmetric Wheatstone bridge UV detector (chapter- 4)**						
47	**Quasi-symmeteric Wheatstone bridge UV detector (chapter- 5)**						
48	**Conclusion and future work (chapter- 6)**						
49	**Bibliography**						
50	**Appendix**						
51	**Ph. D defence**						
52	Send abstract , title and schedule to microEP						
53	Public presentation						
54	Defend before committee						
55	Submit thesis to graduate school						

F: SOFTWARE USED FOR RESEARCH

F.1 Computer 1

Model Number and Serial Number: Dell Inspiron 1545, JG18YJ1

Location: Personal laptop

Owner: Arun Vasudevan

Software 1: Windows XP, Downloaded from MSDN Center, University of Arkansas

Software 2: MS Office, Purchased by Arun Vasudevan

Software 3: MS Project, Downloaded from MSDN Center, University of Arkansas

Software 4: Adobe Reader, Free download

Software 5: PDFill, Free download

Software 6: AutoCAD, Free download (student version)

Software 7: MS Visio, Downloaded from MSDN Center, University of Arkansas

F.2 Computer 2

Model Number and Serial Number: Dell OptiPlex 7010, 85VMLJ1

Location: Engineering Research Center (ENRC), University of Arkansas

Owner: Electrical Engineering Department, University of Arkansas

Software 1: Windows XP, Purchased by University of Arkansas

Software 2: MS Office, Purchased by University of Arkansas

Software 4: Adobe Reader, Free download

Software 5: AutoCAD, Free download (student version)

G: PUBLICATIONS

G.1 Published

1. Vasudevan, A., Jung, S., Ji, T. 2011, "Synthesis and Characterization of Hydrolysis Grown Zinc Oxide Nanorods", *ISRN Nanotechnology,* vol. 2011.

2. Jung, S., Vasudevan, A., Roddy, M. & Ji, T. 2011, "Low temperature zinc oxide nanorod synthesis for gas detection applications", *SPIE NanoScience Engineering* International Society for Optics and Photonics, pp. 81020F.

3. Vasudevan, A., Bourland, C., Jung, S. & Ji, T. 2010 "Preparation of ZnO nanorods for Wheatstone bridge principle based UV detector", pp. 528.

4. Vasudevan, A., Jung, S. & Ji, T. 2009, "Hybrid solar cells using ZnO nanorods", *SPIE Photonic Devices Applications* International Society for Optics and Photonics, , pp. 741607.

5. Vasudevan, A., Jung, S. & Ji, T. 2011, "Optimization of the spray parameters for ZnO based hybrid solar cells", *SPIE NanoScience Engineering* International Society for Optics and Photonics, , pp. 81020D.

6. Vasudevan, A., Jung, S. & Ji, T. 2011, "UV detector from ZnO nanorods with electrodes resembling a wheatstone bridge pattern", *SPIE NanoScience Engineering* International Society for Optics and Photonics, pp. 81020G.

7. Vasudevan, A., Jung, S. & Ji, T. 2012, "On the Responsivity of UV Detectors Based on Selectively Grown ZnO Nanorods", *Sensors Journal, IEEE,* vol. 12, no. 5, pp. 1317-1325.

8. Vasudevan, A., Jung, S. & Ji, T. 2010, "Fabrication of hybrid solar cells by spray coating technique", IASTED International Conference on Nanotechnology and Applications, pp. 552

9. Barnes, B., Rios, J., Vasudevan, A., Manoharan, A., and Ji, T. 2010 "Organic sensors using carbon nanotubes for detecting gases with the Wheatstone bridge design," Proc. the 2nd Annual FEP Honors Research Symp.

G.2 Submitted

1. Vasudevan, A., Jung, S. & Ji, T. 2013, "Wheatstone Bridge Principle Based Ultraviolet Detector" *Journal Name*

G.3 Planned

1. Vasudevan, A., Jung, S., Ji, T. & Ang, S. 2013, "Quasi-symmetric Wheatstone Bridge With Zinc Oxide Nanorod Incorporated UV Detector" *Journal Name*

H: EQUIPMENT USED FOR RESEARCH

Weighing Scale: Ohaus, Adventure Pro AV64C

Ultrasonic Cleaner: VWR, 97043-960 and Branson, 5510

Magnetic Stirrer/Hotplate: Torrey Pines Scientific, HS30

Spin Coater: Specialty Coating Systems, 6800 and G3P-8

Photolithography Mask Aligner: Karl Suss, MA150

Thin Film Thermal Evaporation System: Edwards, Auto306

Oven: Thermo Scientific, BF51848A-1

High Resolution Optical Microscope: Nikon, 57782

Environmental Scanning Electron Microscope: Philips, XL 30

Atomic Force Microscope: Veeco, 3100

X-Ray Diffraction: Philips, PW1830

UV Lamp: Spectroline, EN280L

UV LED: Sensor Electronic Technology Inc, UVTOP355, UVTOP310, UVTOP270

Source Meter: Keithley, 236 and 238

High Resolution Multimeter: Radioshack, 22-812

Micromanipulator probe: Quarter Research & Development, XYZ 300TL

DC Power Supply: BK Precision, 1610

I: FABRICATION PROCEDURE FOR UV DETECTOR

I.1 Simple MSM UV Detector

Step- 1	**Preparation of seed layer**	Set the stirrer temp at 70^0C
		Weigh ethanolamine
		Weigh zinc acetate
		Ethanol solvent
		Mix ethanolamine, zinc acetate, and ethanol: RPM- 400, Stir-1hr, temp-70^0C, cover the beaker
Step- 2	**Wafer Cleaning**	Sonicate in soap solution- 10 min
		Rinse with DI water
		Sonicate in acetone- 5 min
		Rinse with DI water
		Sonicate in IPA- 2 min
		Rinse with DI water
		Rinse and blow with nitrogen
Step- 3	**Spin coating of the seed layer**	Set hot plate temp- 170^0C
		Anneal wafer using hot plate (to get rid of moisture)– 170^0C, 3 min(hot), 3 min(cool)
		Spin coat seed layer solution: RPM– 1000, ramp– 25.5 sec, and dwell time – 20 sec
		Anneal wafer using hot plate (to get rid of solvent)– 170^0C, 3 min(hot), 3 min(cool)
		Repeat the spin coating and annealing process for 5 times
		Anneal the coated wafer (for formation of ZnO seeds)– 350^0C for 1 hr, ramp up and down- ½ hr
Step-4	**Patterning for Gold electrode fabrication**	Blow with N_2
		Heat the wafer for 3 min at 110^0C (to get rid of moisture), cool for 5 min
		Spin coat HMDS: RPM- 5000
		Spin coat photo resist (4110) using recipe for 1.8 µm thick
		Pre-bake at 110^0C for 2 min, cool for 3 min
		Align the electrode patterning mask
		Expose to UV– 8.6 sec (Alignment gap- 65 µm, [expose time = $\underline{(35 \times thickness)}$ +2 sec extra]) Intensity
		Develop in developer solution (Developer:H_2O to 1:3)- 20 sec (After each 5sec, dip in DI water)
		Inspect with microscope
Step- 5	**Evaporation of gold and lift-off**	Set the ultrasonic bath temp. at 40^0C
		Pour liquid nitrogen into Dewar flask of the thermal evaporation system

		Coat chromium- 10 nm (thick), 0.4 nm (deposition rate),
		Coat gold- 125 nm (thick), 0.4 nm (deposition rate), coat in five steps (25 nm thick for each coat and 5 min cool b/w each coating)
		Cool for 5 min, before breaking the vacuum.
		Lift off using acetone with ultrasonic water bath- bath temp at 40^0C
		Rinse with IPA and DI
		Dry with N_2
Step- 6	**Growth of ZnO rods**	Set the stirrer temp at 30^0C
		Weigh zinc nitrate
		Weigh HMT
		DI water
		Mix zinc nitrate and HMT: RPM- 400, Stir- 2hr, temp- 30^0C, cover the beaker
		Immerse the wafer coated with seed layer in the zinc nitrate and HMT mixture aqueous solution (80ml) and heat in oven at 90^0C for 4 hours
		Replace the zinc nitrate and HMT mixture aqueous solution with fresh solution and heat it again in oven at 90^0C for 4 hours.
		Repeat the above ZnO rod growth process for a total growth time of 16 hours, replacing the ZnO growth solution at each 4 hours interval
		Remove the ZnO particles settled on the surface of the wafer by ultrasonification- Acetone(1min), IPA(1 min), DI(1 min)
		Dry with N_2

I.2 Symmetric Wheatstone Bridge MSM UV Detector

Step- 1	**Preparation of seed layer**	Set the stirrer temp at 70^0C
		Weigh ethanolamine
		Weigh zinc acetate
		Ethanol solvent
		Mix ethanolamine, zinc acetate, and ethanol: RPM- 400, Stir-1hr, temp-70^0C, cover the beaker
Step- 2	**Wafer Cleaning**	Sonicate in soap solution- 10 min
		Rinse with DI water
		Sonicate in acetone- 5 min
		Rinse with DI water
		Sonicate in IPA- 2 min
		Rinse with DI water
		Rinse and blow with nitrogen
Step- 3	**Spin coating of the seed layer**	Set hot plate temp- 170^0C
		Anneal wafer using hot plate (to get rid of moisture)– 170^0C, 3 min(hot), 3 min(cool)
		Spin coat seed layer solution- RPM– 1000, ramp– 25.5 sec, and dwell time – 20 sec
		Anneal wafer using hot plate (to get rid of solvent)– 170^0C, 3 min(hot), 3 min(cool)
		Repeat the spin coating and annealing process for 5 times
		Anneal the coated wafer (for formation of ZnO seeds)– 350^0C for 1 hr, ramp up and down- ½ hr
Step- 4	**Etching into four quadrants**	Blow with N_2
		Anneal wafer for 3 min using hot plate at 110^0C (to get rid of moisture), cool for 5 min
		Spin coat photo resist (4110) using recipe for 1.8 µm thick
		Pre-bake the resist at 110^0C for 2 min, cool for 3 min
		Align the patterning mask
		Expose to UV– 8.6 sec (Alignment gap- 65 µm, [expose time = $\frac{35 \times thickness}{Intensity}$ +2 sec extra])
		Develop in developer solution (Developer:H_2O to 1:3)- 20 sec (after each 5sec dip in DI water and then dip in the developer solution)
		Rinse and dry with N_2
		Inspect with microscope
		Etching solution- HCl:H_2O to 0.5 ml:500 ml
		Etching time- 2:30 min
		Strip resist by ultrasonification- Acetone(5min), IPA(2 min), DI(2 min)
Step-5	**Patterning for Gold electrode**	Heat the wafer for 3 min at 110^0C (to get rid of moisture), cool for 5 min

	fabrication	Spin coat HMDS: RPM- 5000
		Spin coat photo resist (4110) using recipe for 1.8 μm thick
		Pre-bake at 110^0C for 2 min, cool for 3 min
		Align the electrode patterning mask and expose for 8.6 sec
		Develop in developer solution (Developer:H_2O to 1:3)- 20 sec (After each 5sec, dip in DI water)
		Inspect with microscope
Step- 6	**Evaporation of gold and lift-off**	Set the ultrasonic bath temp. at 40^0C
		Pour liquid nitrogen into Dewar flask of the thermal evaporation system
		Coat chromium- 10 nm (thick), 0.4 nm (deposition rate),
		Coat gold- 125 nm (thick), 0.4 nm (deposition rate), coat in five steps (25 nm thick for each coat and 5 min cool b/w each coating)
		Cool for 5 min, before breaking the vacuum.
		Lift off using acetone with ultrasonic water bath- bath temp at 40^0C
		Rinse with IPA and DI
Step- 7	**Growth of ZnO rods (On all the four quadrants)**	Set the stirrer temp at 30^0C
		Weigh zinc nitrate
		Weigh HMT
		DI water
		Mix zinc nitrate and HMT: RPM- 400, Stir- 2hr, temp- 30^0C, cover the beaker
		Immerse the wafer coated with seed layer in the aqueous solution and heat in oven at 90^0C for 4 hours
		Replace the zinc nitrate and HMT mixture aqueous solution with fresh solution (80ml) and heat it again in oven at 90^0C for 4 hours.
		Repeat the above ZnO rod growth process for a total growth time of 16 hours, replacing the ZnO growth solution at each 4 hours interval
		Remove the ZnO particles settled on the surface of the wafer by ultrasonification- Acetone(1min), IPA(1 min), DI(1 min)
		Dry with N_2

I.3 Asymmetric Wheatstone Bridge UV Detector

Step- 1	Preparation of seed layer	Set the stirrer temp at 70^0C
		Weigh ethanolamine
		Weigh zinc acetate
		Ethanol solvent
		Mix ethanolamine, zinc acetate, and ethanol: RPM- 400, Stir-1hr, temp-70^0C, cover the beaker
Step- 2	Wafer Cleaning	Sonicate in soap solution- 10 min
		Rinse with DI water
		Sonicate in acetone- 5 min
		Rinse with DI water
		Sonicate in IPA- 2 min
		Rinse with DI water
		Rinse and blow with nitrogen
Step- 3	Spin coating of the seed layer	Set hot plate temp- 170^0C
		Anneal wafer using hot plate (to get rid of moisture)– 170^0C, 3 min(hot), 3 min(cool)
		Spin coat seed layer solution- RPM– 1000, ramp– 25.5 sec, and dwell time – 20 sec
		Anneal wafer using hot plate (to get rid of solvent)– 170^0C, 3 min(hot), 3 min(cool)
		Repeat the spin coating and annealing process for 5 times
		Anneal the coated wafer (for formation of ZnO seeds)– 350^0C for 1 hr, ramp up and down- ½ hr
Step- 4	Etching into four quadrants	Blow with N_2
		Anneal wafer for 3 min using hot plate at 110^0C (to get rid of moisture), cool for 5 min
		Spin coat photo resist (4110) using recipe for 1.8 µm thick
		Pre-bake the resist at 110^0C for 2 min, cool for 3 min
		Align the patterning mask
		Expose to UV– 8.6 sec (Alignment gap- 65 µm, [expose time = $\frac{35 \times \text{thickness}}{\text{Intensity}}$ +2 sec extra])
		Develop in developer solution (Developer:H_2O to 1:3)- 20 sec (after each 5sec dip in DI water and then dip in the developer solution)
		Rinse and dry with N_2
		Inspect with microscope
		Etching solution- HCl:H_2O to 0.5 ml:500 ml
		Etching time- 2:30 min
		Strip resist by ultrasonification- Acetone(5min), IPA(2 min), DI(2 min)
Step-5	Patterning for Gold electrode	Heat the wafer for 3 min at 110^0C (to get rid of moisture), cool for 5 min

	fabrication	Spin coat HMDS: RPM- 5000
		Spin coat photo resist (4110) using recipe for 1.8 μm thick
		Pre-bake at 110^0C for 2 min, cool for 3 min
		Align the electrode patterning mask and expose for 8.6 sec
		Develop in developer solution (Developer:H_2O to 1:3)- 20 sec (After each 5sec, dip in DI water)
		Inspect with microscope
Step- 6	**Evaporation of gold**	Set the ultrasonic bath temp. at 40^0C
		Pour liquid nitrogen into Dewar flask of the thermal evaporation system
		Coat chromium- 10 nm (thick), 0.4 nm (deposition rate),
		Coat gold- 125 nm (thick), 0.4 nm (deposition rate), coat in five steps (25 nm thick for each coat and 5 min cool b/w each coating)
		Cool for 5 min, before breaking the vacuum.
		Lift off using acetone with ultrasonic water bath- bath temp at 40^0C
		Rinse with IPA and DI
Step- 7	**Masking three quadrants or one quadrant**	Anneal wafer using hot plate for 3 min at 110^0C (to get rid of moisture) and cool for 5 min
		Spin coat HMDS- RPM 5000
		Spin coat photo resist (4110) using recipe for 1.8 μm thick
		Pre-bake at 110^0C for 2 min, cool for 3 min
		Align pattern mask and expose- 8.5 sec
		Develop in developer solution (Developer:H_2O to 1:3)- 20 sec (after each 5sec dip in DI water and then dip in the developer solution)
		Rinse with DI and dry with N_2
Step- 8	**Growth of ZnO rods (On unmasked quadrants)**	Set the stirrer temp at 30^0C
		Weigh zinc nitrate
		Weigh HMT
		DI water
		Mix zinc nitrate and HMT: RPM- 400, Stir- 2hr, temp- 30^0C, cover the beaker
		Immerse the wafer coated with seed layer in the aqueous solution and heat in oven at 90^0C for 4 hours
		Replace the zinc nitrate and HMT mixture aqueous solution with fresh solution (80ml) and heat it again in oven at 90^0C for 4 hours.
		Repeat the above ZnO rod growth process for a total growth time of 16 hours, replacing the ZnO growth solution at each 4 hours interval
		Remove photoresist and remove ZnO particles by ultrasonification- Acetone(1min), IPA(1 min), DI(1 min) and then dry with N_2

I.4 Quasi-Symmetric Wheatstone Bridge

Step- 1	**Preparation of seed layer**	Set the stirrer temp at 70^0C
		Weigh ethanolamine
		Weigh zinc acetate
		Ethanol solvent
		Mix ethanolamine, zinc acetate, and ethanol: RPM- 400, Stir-1hr, temp-70^0C, cover the beaker
Step- 2	**Wafer Cleaning**	Sonicate in soap solution- 10 min
		Rinse with DI water
		Sonicate in acetone- 5 min
		Rinse with DI water
		Sonicate in IPA- 2 min
		Rinse with DI water and dry with N_2
Step- 3	**Spin coating of the seed layer**	Set hot plate temp- 170^0C
		Anneal wafer using hot plate (to get rid of moisture)– 170^0C, 3 min(hot), 3 min(cool)
		Spin coat seed layer solution- RPM– 1000, ramp– 25.5 sec, and dwell time – 20 sec
		Anneal wafer using hot plate (to get rid of solvent)– 170^0C, 3 min(hot), 3 min(cool)
		Repeat the spin coating and annealing process for 5 times
		Anneal the coated wafer (for formation of ZnO seeds)– 350^0C for 1 hr, ramp up and down- ½ hr
Step- 4	**Etching into four quadrants**	Blow with N_2
		Anneal wafer for 3 min using hot plate at 110^0C (to get rid of moisture), cool for 5 min
		Spin coat photo resist (4110) using recipe for 1.8 µm thick
		Pre-bake the resist at 110^0C for 2 min, cool for 3 min
		Align the patterning mask
		Expose to UV– 8.6 sec (Alignment gap- 65 µm, [expose time = $\frac{35 \times thickness}{Intensity}$ +2 sec extra])
		Develop in developer solution (Developer:H_2O to 1:3)- 20 sec (after each 5sec dip in DI water and then dip in the developer solution)
		Rinse and dry with N_2
		Inspect with microscope
		Etching solution- HCl:H_2O to 0.5 ml:500 ml
		Etching time- 2:30 min
		Strip resist by ultrasonification- Acetone(5min), IPA(2 min), DI(2 min)
Step-5	**Patterning for Gold electrode fabrication**	Heat the wafer for 3 min at 110^0C (to get rid of moisture), cool for 5 min
		Spin coat HMDS: RPM- 5000

		Spin coat photo resist (4110) using recipe for 1.8 µm thick
		Pre-bake at 110^0C for 2 min, cool for 3 min
		Align the electrode patterning mask and expose for 8.6 sec
		Develop in developer solution (Developer:H_2O to 1:3)- 20 sec (After each 5sec, dip in DI water)
		Inspect with microscope
Step- 6	**Evaporation of gold and lift-off**	Set the ultrasonic bath temp. at 40^0C
		Pour liquid nitrogen into Dewar flask of the thermal evaporation system
		Coat chromium- 10 nm (thick), 0.4 nm (deposition rate),
		Coat gold- 125 nm (thick), 0.4 nm (deposition rate), coat in five steps (25 nm thick for each coat and 5 min cool b/w each coating)
		Cool for 5 min, before breaking the vacuum.
		Lift off using acetone with ultrasonic water bath- bath temp at 40^0C
		Rinse with IPA and DI
Step- 7	**Masking one of the diagonal quadrants**	Anneal wafer using hot plate for 3 min at 110^0C (to get rid of moisture) and cool for 5 min
		Spin coat HMDS- RPM 5000
		Spin coat photo resist (4110) using recipe for 1.8 µm thick
		Pre-bake at 110^0C for 2 min, cool for 3 min
		Align pattern mask for diagonal masking and expose- 8.5 sec
		Develop in developer solution (Developer:H_2O to 1:3)- 20 sec (after each 5sec dip in DI water and then dip in the developer solution)
		Rinse with DI and dry with N_2
Step- 8	**Growth of ZnO rods (Along the unmasked diagonal)**	Set the stirrer temp at 30^0C
		Weigh zinc nitrate
		Weigh HMT
		DI water
		Mix zinc nitrate and HMT: RPM- 400, Stir- 2hr, temp- 30^0C, cover the beaker
		Immerse the wafer coated with seed layer in the aqueous solution (80ml) and heat in oven at 90^0C for 4 hours
		Strip the photoresist by ultrasonification- Acetone(1min), IPA(1 min), DI(1 min) and dry with N_2
Step- 9	**Growth of ZnO rods (On all the four quadrants)**	Immerse the wafer coated with seed layer in fresh aqueous solution and heat in oven at 90^0C for 4 hours
		Remove ZnO particles settled on the surface of the wafer by ultrasonification- Acetone(1min), IPA(1 min), DI(1 min) and then dry with N_2

J: MODELLING OF CONVENTIONAL MSM ZINC OXIDE BASED UV DETECTOR FOR DIFFERENT ROD AND ELECTRODE DIMENSION

The current through the MSM is given by

$$I = AA^*T^2 \exp\left(-\frac{q\emptyset_n}{KT}\right) \exp\left(\frac{q\Delta\emptyset_n}{KT}\right)\left(1 - \exp\left(-\frac{q(V - IR)}{nKT}\right)\right) \qquad \text{Eq (J − 1)}$$

where A is the area of the interdigitated fingers, A^* is the Richardson constant, T is the absolute temperature, K Boltzmann constant, $\emptyset_n$ is the barrier height, $\Delta\emptyset_n$ is the Schottky barrier lowering, V is the potential drop across the reverse bias Schottky junction, n is the ideality factor, and R is the series resistance.

The decrease in barrier height $\Delta\emptyset_n$ is given by,

$$\Delta\emptyset_n = \left[\frac{2q^3NV}{16\pi^2\varepsilon_s{}^3}\right]^{1/4} \qquad \text{Eq (J − 2)}$$

where N is the electron carrier concentration, ε_s is the permittivity of ZnO seed layer, and V is the potential drop across the reverse bias Schottky junction.

If it is assumed that n=1 , then Eq (J-1) can be rewritten as

$$I = AA^*T^2 \exp\left(-\frac{q\emptyset_n}{KT}\right) \exp\left(\frac{q\Delta\emptyset_n}{KT}\right)\left(1 - \exp\left(-\frac{q(V - IR)}{KT}\right)\right) \qquad \text{Eq (J − 3)}$$

$$\text{Area of interdigitated finger}, A = \text{finger width (w)} * \text{finger spacing (s)} \qquad \text{Eq (J − 4)}$$

$$\text{Increase in carrier concentration due to UV illumination}, N = \frac{\eta F\tau}{V_r + V_s} \qquad \text{Eq (J − 5)}$$

Where η is the charge conversion efficiency, F is the photon absorption rate, τ is the life time of

the carriers, V_r is the total volume of the rods, and V_s is the total volume of the seed layer

Total volume of the rods, V_r

$$= \pi * \text{radius of rod}(r)^2 * \text{length of rod (l)}$$

$$* \text{density of rod growth}(\rho) \qquad\qquad \text{Eq (J − 6)}$$

Total volume of the seed layer, V_s

$$= \text{finger spacing}(s) * \text{length of finger}(b)$$

$$* \text{thickness of seed layer}(t) \qquad\qquad \text{Eq (J − 7)}$$

The current given by Eq (J-1) is for the back to back Schottky diode formed between two interdigitated fingers. If there are D(n) number of finger spacing for a pattern, then the total current for the pattern is given by,

$$I = D(n)AA^*T^2 \exp\left(-\frac{q\varnothing_n}{KT}\right) \exp\left(\frac{q\Delta\varnothing_n}{KT}\right)\left(1 - \exp\left(-\frac{q(V - IR)}{KT}\right)\right) \qquad \text{Eq (J − 8)}$$

Using the above equation the current values measured for different rod dimension and electrode dimension (shown in Figure 3-14) was fitted theoretically by varying the different parameters associated with Eq (J-8). The values of the various parameters used for the fitting is shown in Table J-1.

The value of the constants used for the fitting are Richardson constant (A^*)= 32 A/(cm^2 K^2), Temperature (T)= 300 K, Boltzmann constant (K)= 1.38 x 10^{-23} J/K, Permittivity of ZnO seed layer (ε_s)= 9ε_0= 9 x 8.85 x 10^{-14} F/cm = 7.97 x 10^{-13} F/cm, Thickness of seed layer (t)= 40 x 10^{-4} cm.

Table J-1   Values of the pattern dimension and rod dimension used for fitting the corresponding measured current values

Pattern dimension					Rod dimension		
Pattern label	Length (b) (cm)	Spacing (s) (cm)	Width (w) (cm)	No. of diodes D(n)	Growth time (hr)	Radius (r) (cm)	Length (l) (cm)	Density (ρ) (cm^2)
L1	4.90E-01	2.80E-02	2.00E-02	40	4	1.25E-06	6.00E-05	9.50E+09
L2	3.80E-02	4.50E-03	4.00E-03	16	4	1.50E-06	7.20E-05	7.60E+09
L3	9.75E-02	4.50E-03	5.00E-03	40	4	1.30E-06	6.24E-05	8.60E+09
L4	1.95E-01	9.00E-03	1.00E-02	40	4	1.28E-06	6.34E-05	8.73E+09
L1	4.90E-01	2.80E-02	2.00E-02	40	8	1.75E-06	6.50E-05	9.50E+09
L2	3.80E-02	4.50E-03	4.00E-03	16	8	2.10E-06	7.80E-05	7.60E+09
L3	9.75E-02	4.50E-03	5.00E-03	40	8	1.82E-06	6.76E-05	8.60E+09
L4	1.95E-01	9.00E-03	1.00E-02	40	8	1.79E-06	6.86E-05	8.73E+09
L1	4.90E-01	2.80E-02	2.00E-02	40	16	2.63E-06	1.45E-04	9.50E+09
L2	3.80E-02	4.50E-03	4.00E-03	16	16	3.16E-06	1.74E-04	7.60E+09
L3	9.75E-02	4.50E-03	5.00E-03	40	16	2.74E-06	1.51E-04	8.60E+09
L4	1.95E-01	9.00E-03	1.00E-02	40	16	2.70E-06	1.53E-04	8.73E+09

Table J-2   Values of the various parameters used for fitting the measured current values for different rod dimension and electrode dimension

Pattern label	Life time (τ) (s)	Voltage (V) (V)	Barrier Height ($\emptyset_n$) (V)	Photon abs. and electron Conv. (F and η) (%)	Calculated Current (A)	Measured Current (A)	Respon-sivity (A/W)
L1	1.00E-01	4	7.90E-01	60	1.04E-03	1.04E-03	1.81E+00
L2	3.10E-01	4.6	7.95E-01	55	1.26E-04	1.25E-04	4.02E+01
L3	2.99E-01	4.6	7.93E-01	57	1.02E-03	1.02E-03	5.46E+01
L4	2.25E-01	4.4	7.91E-01	58	1.87E-03	1.89E-03	2.54E+01
L1	9.70E-02	4.1	7.91E-01	65	5.84E-04	5.80E-04	1.01E+00
L2	5.80E-01	4.7	7.96E-01	60	2.39E-04	2.43E-04	1.31E+01
L3	1.58E-01	4.7	7.94E-01	62	9.25E-05	9.25E-05	2.98E+01
L4	2.40E-01	4.5	7.92E-01	64	1.35E-03	1.26E-03	1.69E+01
L1	6.97E-01	4.3	7.92E-01	75	9.66E-03	9.65E-03	1.69E+01
L2	2.14E+00	4.9	7.97E-01	70	7.68E-04	7.65E-04	2.47E+02
L3	1.59E+00	4.9	7.95E-01	72	7.49E-03	7.54E-03	4.06E+02
L4	1.54E+00	4.7	7.93E-01	74	3.03E-02	3.01E-02	4.05E+02